

Phase Field Modelling of Bainitic Transformation

by

Fawzi Elhigazi

A thesis submitted to the Faculty of Graduate and Postdoctoral
Affairs in partial fulfillment of the requirements for the degree of

Doctor of Philosophy in Mechanical Engineering

Ottawa-Carleton Institute for Mechanical and Aerospace
Mechanical and Aerospace Engineering

Department of Mechanical and Aerospace Engineering

Carleton University
Ottawa, Ontario, Canada

© Copyright by Fawzi Elhigazi

March 2020

Abstract

A phase field model was developed to study the interaction between the displacive transformation, diffusion process and carbide formation during the bainitic type transformation. The thermodynamic data for the chemical free energy were obtained using the Thermo-Calc software. Also, the transformation strains reproducing the $\gamma \rightarrow \alpha$ transformation with three transformation variants of ferrite were used. In the case of carbide free bainite, the bainitic transformation develops in two stages: the first, fast stage, wherein the displacive transformation is dominant at the onset of the transformation, and the second stage, which begins when the diffusion-controlled decomposition takes control over the transformation kinetics and ferrite morphology, and results in the formation of a carbon enriched layer around ferrite grains. Both plate-like and rod-like shapes of the ferrite grains can be obtained depending on the thermodynamic conditions and diffusion mobility.

The carbide nucleation was modeled as the formation of carbon sinks either in retained austenite or in supersaturated ferrite with different nucleation sequences. The results indicated that in the case of carbide formation in retained austenite, the carbide nucleation might play a secondary role controlling the transformation kinetics and microstructure evolution after the completion of the fast transformation stage; however, elastic interactions could control the ferrite morphology even at a later stage, thus leading to the change of the ferrite grain shape from a rod-like to plate-like. In the case of carbide formation in supersaturated ferrite, the results demonstrated that initially, due to a slow

nucleation of carbides and fast carbon partitioning, carbon diffusion to austenite was the dominant process leading to the decrease in the transformation rate. However, after some period of time, the effect of carbon depletion by carbides in the solid solution became more significant, which led to the reduction of the average concentration of carbon in the whole system and to the acceleration of the structural transformation. In both cases, the rate of carbide nucleation and the number of nucleated carbides controlled both the transformation rate and the period of time before the transformation acceleration.

Acknowledgements

First and foremost, I am most grateful to Allah (God), the Creator and Sustainer of the universe, for His uncountable bounties on me including the ability to perform this research and to write this thesis.

I gratefully acknowledge the intellect, wisdom and efforts of Dr. Andrei Artemev whose labor and profound understanding formed the foundation for this work.

I am deeply grateful to my parents who raised me and instilled in me the love and appreciate of knowledge. To my children: Mueen, Malak, Munib, and Mubin, your smiles and laughter gave me hope and motivation; thanks for being patient and for your limitless unconditional love. Finally, I am extremely thankful to my wife, Hana, for her constant support endless patience, understanding and encouragement throughout this period.

Preface

As defined by section 12.4 of 2020-2021 Carleton University Graduate Calendar, the current thesis is an integrated Ph. D thesis. It includes the following articles which are either published (paper 1) or are under review (papers 2,3):

1. F. Elhigazi, A. Artemev, The interaction between the displacive transformation and the diffusion process in the bainitic type transformation, Computational Materials Science. 169 (2019) 109079.
2. F. Elhigazi, A. Artemev, The interaction between the carbon partitioning and carbide nucleation inside austenite during the bainitic type transformation, Computational Materials Science.
3. F. Elhigazi, A. Artemev, The influence of carbide formation in ferrite on the bainitic type transformation, Computational Materials Science.

Contents

Abstract.....	i
Acknowledgements	iii
Preface.....	iv
List of Figures.....	viii
List of Appendices.....	xiv
List of Symbols	xvi
Chapter 1: Introduction.....	1
1.1 Motivation	1
1.2 Objective.....	4
1.3 Outline	5
Chapter 2: Background and Literature Review.....	7
2.1 Overview of bainitic transformation and bainitic structures.....	7
2.2 Phenomenon of incomplete bainitic transformation and T_0 concept.....	10
2.3 Bainite crystallography.....	13
Chapter 3: The interaction between the displacive transformation and the diffusion process in the bainitic type transformation.	16
Abstract.....	16
3.1 Introduction	16
3.2 Phase field Model.....	20

3.2.1	Order parameters and transformation strains	20
3.2.2	Energy functional.....	22
3.2.3	Elastic energy.....	23
3.2.4	Governing equation.....	25
3.2.4	Model parameters	26
3.3	Results	30
3.3.1	Transformation development.....	30
3.3.2	Strain energy effect.....	35
3.3.3	Mobility effect	37
3.4	Discussion.....	39
3.5	Conclusions	43
Chapter 4: The interaction between the carbon partitioning and carbide nucleation inside austenite during the bainitic type transformation.....		
		45
4.1	Introduction	46
4.2	Phase field modelling	49
4.2.1	Transformation variants and order parameters	50
4.2.2	Energy functional and strain energy	51
4.2.3	Governing equations	53
4.2.4	Modelling of carbide nucleation	54
4.2.5	Model parameters	56
4.3	Results	58
4.4	Discussion.....	70
4.5	Conclusions	74
Chapter 5: The influence of carbide formation in ferrite on the bainitic type transformation.		
		76
5.1	Introduction	77

5.2	Phase field modelling	80
5.2.1	Order parameters and transformation strains	81
5.2.2	Chemical free energy functional	82
5.2.3	Elastic strain energy	83
5.2.4	Governing equations for microstructure evolution	84
5.2.5	Modelling of carbide nucleation	85
5.2.6	Computational parameters	86
5.3	Results	88
5.3.1	Transformation development without carbide nucleation.	88
5.3.2	Transformation development with two different carbide nucleation sequences..	93
5.4	Discussion.....	104
5.5	Conclusions	107
	Chapter 6: Conclusions	109
	Appendix A.....	112
	References.....	116

List of Figures

Figure 2-1 Schematic representation of a plate and a lath [20].	7
Figure 2-2 Transmission electron micrograph of carbide-free bainitic structure formed at 200°C with each bainitic plate is separated by retained austenite [19].	8
Figure 2-3 The schematic of the nucleation and growth of subunits during the bainite formation [20].	8
Figure 2-4 The schematics of TTT diagram illustrating the flat tops on the bainite C-curves [20].	10
Figure 2-5 The schematic illustration of the origin of the T_0 curve on the phase diagram. The T_0' curve incorporates the strain energy term for ferrite, illustrated on the diagram by rising the free energy curve for ferrite by an appropriate quantity [20].	11
Figure 2-6 The fraction volume of ferrite vs time obtained at different temperatures for Fe-0.1C-3Mn alloy [28].	13
Figure 2-7 Orientation relationships between austenite (fcc) and ferrite (bcc) lattices: (a) K-S orientation relationships, (b) N-W orientation relationships [30].	14
Figure 3-1. Free energy curves vs. carbon wt% plot for both the austenite and ferrite phase using Eq. (3-7) and the corresponding parameters obtained at 260 °C. Δf_0 is the free energy difference between the α and γ phases at the corresponding initial carbon content (\bar{c}), c_γ is the equilibrium carbon concentration in the γ phase, c_α is the equilibrium	

carbon concentration in the α phase and $\eta_{\min}(c)$ is the minima order parameter corresponding to the value of c at that point..... 27

Figure 3-2. Free energy curves vs. carbon wt% plot for both the austenite and ferrite phase using Eq. (3-7) and the corresponding parameters obtained at 500 °C. Δf_0 is the free energy difference between the α and γ phases at the corresponding initial carbon content (\bar{c}), c_γ is the equilibrium carbon concentration in the γ phase, c_α is the equilibrium carbon concentration in the α phase and $\eta_{\min}(c)$ is the minima order parameter corresponding to the value of c at that point..... 28

Figure 3-3. Structure sequences (upper) and respective distributions of the carbon concentrations (lower) at different reduced times; (a)-(d) corresponding to $t = 5, 10, 50, 10300$ in the system with the thermodynamic parameters corresponding to 260°C, $\zeta = 1157$ and $M = 0.1$. C' is the periodic repetition of the morphology to show the whole plate size..... 31

Figure 3-4. Structure sequences (upper) and respective distributions of the carbon concentrations (lower) at different reduced times; (a)-(e) correspond to $t = 20, 21, 25, 100, 671$ in the system with the thermodynamic parameters corresponding to 500°C, $\zeta = 1157$ and $M = 0.1$ 31

Figure 3-5. One dimensional distributions of the carbon concentration along the white lines shown in the inserts with two-dimensional concentration maps. The inserts demonstrate the final concentration distributions and the graphs show distributions at different moments of time. (a) distributions obtained in the system with the thermodynamic parameters corresponding to 260°C, $\zeta=1157$ and $M=0.1$. Spatial

coordinate is counted along the white line on the insert from left to right. (b) distributions obtained in the system with the thermodynamic parameters corresponding to 500°C, $\zeta=1157$ and $M = 0.1$. Spatial coordinate is counted along the white line on the insert from bottom to top. 33

Figure 3-6. Dependencies of the austenite volume fraction on time obtained in the systems with (a) the thermodynamic parameters corresponding to 260°C, $\zeta=1157$ and $M = 0.1$. (b) the thermodynamic parameters corresponding to 500°C, $\zeta=1157$ and $M = 0.1$. The inserts show the initial high transformation rate stages with a higher temporal resolution..... 35

Figure 3-7. Different morphologies of final structures obtained with (a) the thermodynamic parameters corresponding to 260°C, $\zeta = 1157$ and $M = 0.1$. (b) the thermodynamic parameters corresponding to 260°C, $\zeta = 500$ and $M = 0.1$ 36

Figure 3-8 Morphologies of final structures (upper) and respective distributions of the carbon concentrations (lower) at 260°C with (a) the thermodynamic parameters corresponding to $\zeta = 1157$ and $M = 0.01$. (b) the thermodynamic parameters corresponding to $\zeta = 500$ and $M = 0.1$. (c) the thermodynamic parameters corresponding to $\zeta = 1157$ and $M = 1$ 38

Figure 4-1 The effects of different distributions of the nucleation events with time on the ferrite volume fraction rate and the overall average carbon concentration rate. The solid lines represent the number of carbide sinks introduced at different times; the dotted lines show the evolution of the ferrite volume fraction rate and the dashed lines show the average carbon concentration rate. The initial average carbon concentration in the system

is 0.92 wt.% and the final average carbon concentration in the system is 0.6 wt.%, which is the carbon content of carbide in equilibrium with austenite. 59

Figure 4-2 Distributions of the carbon concentrations sequences (upper) and respective structures (lower) at different moments of time outlined in Fig. 4-1 a. All transformation variants of ferrite are shown with the same colour. 61

Figure 4-3. One dimensional distributions of the carbon concentration along the dotted white line (from bottom to top) shown in the insert with a two-dimensional concentration map at $t=t_a$ where the encircled point is the location of the first carbide sink. The graph shows carbon concentrations at different moments of time with the coloured solid lines, whereas the coloured dashed lines represent the different positions of the structural boundaries at different moments of time, and the encircled point indicates the location of the first carbide sink. All time markings indicated on these curves are consistent with time moments indicated by the same letters in Fig. 4-1 a. 63

Figure 4-4 (a) Dependence of the ferrite volume fraction on time obtained in the systems without the formation of carbide. (b) Two-dimensional gradient of carbon concentrations through the coloured solid lines and the coloured dashed lines represents different positions of the boundary interface at three different moments of time along the same line as in Fig. 4-3. 65

Figure 4-5 Morphologies of the final distributions of the carbon concentrations (upper) and respective structure (lower) at different moments of time outlined in (a) scenario 2, (b) scenario 3, and (c) scenario 4. The marked points that are pointed out by arrows show the first carbide sink formed at time t_a 67

Figure 4-6. One dimensional distributions of the carbon concentration along the dotted white line (from bottom to top) shown in the insert with a two-dimensional concentration map at $t=t_a$, where the encircled point is the location of the first carbide sink. The graph shows the carbon concentrations and different positions of the structural boundaries with coloured solid lines at moments of time t_a , t_b and t_c outlined in Fig. 4-1a (scenario 1), while the coloured dotted lines represent the carbon concentrations and different positions of the structural boundaries at moments of time t_a , t_b and t_c outlined in Fig. 4-1b (scenario 2). All time markings indicated on these curves are consistent with time moments indicated by the same letters in Fig. 4-1 a and b, respectively..... 68

Figure 5-1 The dependence of the ferrite fraction on the time obtained in the system with the initial carbon concentration 0.92 wt.% and no carbide nucleation allowed. 89

Figure 5-2. Coloured solid lines represent the distribution of carbon concentration; coloured dashed lines represent positions of the interfaces at different moments of time along the dotted arrow shown in the top left thumbnail. representing the carbon distribution map and respective structure at t_a 90

Figure 5-3 Distributions of the carbon concentrations (a) and the sequences of the corresponding structures (b) at different moments of time marked in Fig. 5-1 and Fig. 5-2. (c) shows a vertical cross section of the corresponding structure (b) along the line (A-A). All transformation variants of ferrite are shown in the same colour. 92

Figure 5-4. The solid line represents the number of carbide sinks introduced at different times; the dashed line shows the evolution of the ferrite volume fraction rat; the dotted line shows the average carbon concentration rate. The initial average carbon

concentration in the system is 0.92 wt%; the final average carbon concentration in the system is 0.025 wt% (the carbon content of carbide in equilibrium with ferrite). 94

Figure 5-5. One dimensional distributions of the carbon concentration along the dotted white arrow shown in the insert with a two-dimensional concentration map and microstructure at $t=t_a$. The encircled point is the location of the first carbide sink. The coloured solid lines present carbon concentrations at different moments of time; the coloured dashed lines represent different positions of the structural boundaries at different moments of time. All time moments indicated on the curves correspond to time moments indicated by the same letters in Fig. 5-4..... 97

Figure 5-6 (a) Distributions of the carbon concentrations sequences (upper) and respective structure (lower) at different moments of time marked in Fig. 5-4. (b) Periodic repetition of the structure shown in Fig. 5-6 a at the moment of time $t= t_e$. Solid red lines outline the boundaries of composite austenite-ferrite plates; dotted red lines outline the austenite-ferrite interfaces in the plates. All transformation variants of ferrite are shown in the same colour. 100

Figure 5-7 Solid line represents the number of carbide sinks introduced at different time; dashed line shows the evolution of the ferrite volume fraction rate; dotted line shows the average carbon concentration rate. The initial average carbon concentration in the system is 0.92 wt%; the final average carbon concentration in the system is 0.025 wt%. 102

Figure 5-8. Periodic repetition of the structure at time $t= t_d$ marked in Fig. 5-7. All transformation variants of ferrite are shown in the same colour. 103

List of Appendices

Appendix A.....	110
-----------------	-----

List of Symbols

FCC	Face centered cubic
BCC	Body centered cubic
BCT	Body centered tetragonal
TTT	Time-temperature-transformation
α	Ferrite phase
γ	Austenite phase
K-S	Kurdjumov–Sachs orientation relationships
N-W	Nishiyama–Wassermann orientation relationships
TRIP	Transformation Induced Plasticity
FEM	Finite element method
c	Carbon concentration
\bar{c}	Initial composition
c_α	Equilibrium carbon concentration in the α phase
c_γ	Equilibrium carbon concentration in the γ phase
ε_{ij}^{00}	Transformation strain
ζ	Characteristic energy ratio
M	Kinetic coefficient of diffusional mobility
L	Kinetic coefficient of long-range order relaxation rate
E	Gibbs free energy
η	Order parameter

Chapter 1: Introduction

1.1 Motivation

Over the years, there has been a lack of agreement on the nature of the bainitic transformation. The main disagreement has been on whether or not the formation of bainitic ferrite is controlled by diffusional processes or by the displacive structural transformation. Many studies have proposed various interpretations of the morphology and kinetics of this transformation. However, the debate on the nature of the bainitic transformation still continues. There are many different models of bainitic transformation that can be found in the literature. In [1-4] the micro-macro models of the bainitic transformation, based on the general Johnson-Mehl-Avrami-Kolmogorov phase transformation model, were introduced. In these models, the microstructure state is described by the volume fraction of ferrite units (bainite subunits), which, in turn, is determined by the number of units and their size. It is assumed that the growth of units from the nucleation to a definite size occurs instantaneously, and the overall transformation rate is then determined by the nucleation rate alone. All the ferrite units in the material volume have the same size; according to the model assumptions, however, this size can be different at different temperatures [2]. The nucleation kinetics according to the models presented in [1-9] can be described by the kinetics function accounting for the effect of the autocatalysis and carbon partitioning, assuming that partitioning occurs

after the ferrite units reach their limiting size and a uniform distribution of carbon in austenite is maintained. The later assumption means that partitioning is slow as compared to the subunit growth but fast as compared to the nucleation process. The analytical [1, 2, 4] and numerical [3] solutions, based on these models and utilizing a number of empirical coefficients, were obtained for the kinetics of the bainitic transformation in high silicon steels [10]. The models based on the displacive transformation mechanism are strongly supported by the established relationship between the temperature, below which the bainitic transformation becomes possible, and the carbon concentration in austenite [10]. Recent experimental studies provide a strong evidence in favour of the displacive mechanism control of the bainite formation [10, 11]; however, the diffusion process also is undeniably present during the transformation.

The bainitic transformation often demonstrates a nontrivial kinetics with the phenomenon of an incomplete transformation or transformation stasis under isothermal transformation conditions. In that case, the transformation occurs at a greatly reduced rate or stops completely while a significant amount of austenite is still untransformed. However, after some time in stasis, the transformation can reaccelerate (without changes in temperature or any other external conditions), eventually producing a complete transformation. Such a behavior is very different from the usual transformation kinetics characterized by the transformation-time curve with a sigmoidal shape. The multistage nature of the bainitic transformation suggests that changes in the internal factors controlling the transformation rate lead to transitions between different stages.

Several different techniques for the simulation of the phase pattern evolution during phase transformations have emerged: the molecular dynamics [12], Monte Carlo methods [13], cellular automata [14] and phase field method [15-17]. Molecular dynamics with the evolution described at the level of individual atoms places severe restrictions on the maximum size of the model and, therefore, cannot be used for the simulation of the bainitic transformation. The Monte Carlo, cellular automata and phase field methods describe microstructure patterns at the mesoscopic level and, thus, are equally applicable for the length scales typical for bainitic structures. The Monte Carlo and cellular automata methods may have a simpler implementation for the processes without deformation effects associated with the transformation; however, if the transformation produces a stress-free strain and the strain energy plays a significant role in the transformation process, then the phase field method based on the micromechanics theory and utilizing the Fast Fourier transform method for the solution of the elasticity problem [18] has a significant computational advantage. With this method the strain energy and driving forces for the microstructure evolution can be calculated faster than with alternative numerical methods (such as FEM), and models with a larger size can be studied. As a result, the phase field method has become the main tool for the simulation of the microstructure evolution in solids.

1.2 Objective

The objective of this thesis is to use the phase field model to simulate three different cases of the bainitic transformation in order to obtain a better understanding of the main factors controlling the development of this transformation and resolve some questions about the factors controlling the transformation which are still under discussion.

1. In the case of the model of carbide-free bainite formation, the main objective is to investigate which of the displacive or diffusion modes may better describe the transformation of the bainitic type and which of the displacive transformation or diffusion decomposition processes plays a more important role controlling the transformation and the final microstructure.
2. In the case of the model of bainite formation with carbides inside austenite, the main objective is to investigate a) the effect of carbide formation on carbon partition and b) to which extent the strain energy may play a substantial role determining the final microstructure.
3. In the case of the model of bainite formation with carbides produced inside supersaturated bainitic ferrite, the main objective is to investigate how the

interaction between carbide formation and the strain energy can produce a significant effect on the transformation kinetics and morphology of microstructure.

1.3 Outline

The current thesis is an integrated work that incorporates three papers which are either published or under review. This section provides an outline of the remaining chapters and papers included in this thesis.

Chapter 2: This chapter contains a literature review on several important topics related to this thesis, including the basics of: the bainitic transformation and bainitic structure, incomplete phenomenon of the bainitic transformation and T_0 concept, and the bainite crystallography.

Chapter 3: The first paper (published in Computational Materials Science in July 2019) covers the interaction between the displacive transformation and the diffusion process during a bainitic type transformation. The transformation models with different mobility coefficients of the structural transformation and diffusion, and with a different strength of elastic interactions are studied in the paper with the goal to find how such parameters may control the transformation kinetics and morphology.

Chapter 4: The second paper (submitted to Computational Materials Science in February 2020) covers the interaction between carbon partitioning and carbide nucleation inside austenite during a bainitic type transformation using four different transformations - carbide formation scenarios producing a different number of carbides at different formation rates. This study has the goal to determine how the carbide formation may play a role controlling the transformation kinetics and microstructure evolution.

Chapter 5: The third paper (submitted to Computational Materials Science in March 2020) covers the interaction between the displacive transformation, carbon partitioning from ferrite to austenite, and carbide formation in bainitic ferrite. The main goal of this study was to determine how carbide formation may play a critical role controlling the transformation, carbon partitioning kinetics and microstructure evolution through simulations with two different transformation - carbide formation sequences.

Chapter 6: This chapter contains the conclusions of the thesis.

Chapter 2: Background and Literature Review

2.1 Overview of bainitic transformation and bainitic structures.

Bainite microstructure has been described as aggregates of either plates or laths of ferrite (Fig. 2-1), separated by untransformed austenite (Fig. 2-2) or cementite [19]. The aggregates of the bainitic plates are called sheaves, and the individual plates are called

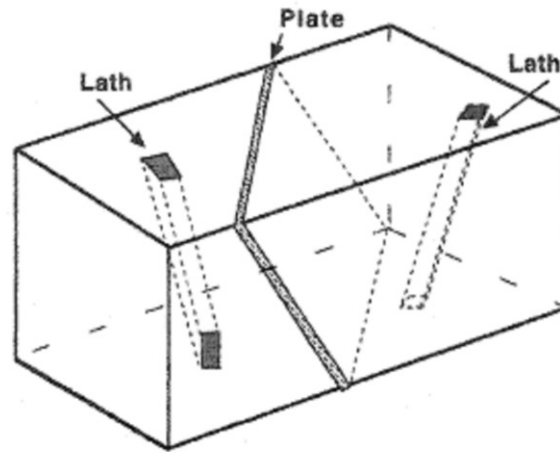


Figure 2-1 Schematic representation of a plate and a lath [20].

sub-units [20]. The shape of a sheaf on a macroscopic scale is similar to a wedge shaped plate and growth of this sheaf occurs by repeated nucleation of sub-units each of which grows rapidly to a limited size (autocatalysis nucleation) [20]. There are two opposite theories regarding the development of the bainitic transformation: the displacive transformation theory and diffusion limited growth model [20-22]. In the displacive mechanism theory no composition change accompanies the nucleation and growth of

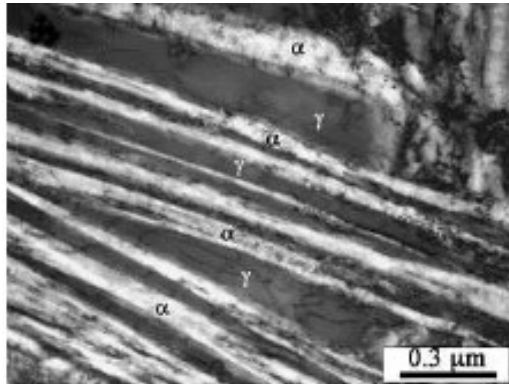


Figure 2-2 Transmission electron micrograph of carbide-free bainitic structure formed at 200°C with each bainitic plate is separated by retained austenite [19].

bainite (or individual subunits) while in the diffusion limited growth model there is a change in the chemical composition of austenite when it begins to decompose into ferrite. These opposite theories regarding the development of the bainitic transformation will be discussed in detail in chapter 3.



Figure 2-3 The schematic of the nucleation and growth of subunits during the bainite formation [20].

Bainite is classified as upper and lower bainite based on the presence of carbides and their location. During a bainitic formation, carbides can form either in carbon-enriched residual austenite (upper bainite) or within bainitic ferrite (lower bainite) [20, 23, 24]. In upper bainite, carbide formation inside austenite can be caused by carbon partitioning between ferrite and austenite, and, once produced will lead to the development of bainitic ferrite as a diffusion-controlled ledge-wise growth [25]. In this case, carbide might play a subsequent role controlling the transformation kinetics of upper bainite [20, 24, 26]. However, the effect of carbide formation in bainitic ferrite on the transformation kinetics is more complicated and is not completely understood [20, 24, 26].

There is a variety of factors (such as temperature and alloying elements), that can produce a significant impact on the bainitic transformation kinetics. For example, at high temperature the carbon partitioning from bainitic ferrite to austenite is rapid, so that any carbide formation occurs in a carbon-enriched layer in austenite and the final microstructure morphology produced in this process is that of upper bainite. Thus, the upper bainitic ferrite in this case is free from precipitates [20, 24]. However, due to a low diffusivity at a lower temperature, less carbon decomposes from bainitic ferrite to austenite, so that carbide formation within bainitic ferrite is more effective. Thus, the lower bainite microstructure is produced based on this condition. Also, the presence of a dislocation in bainitic ferrite can result in supersaturated bainitic ferrite and allow carbides to form only within bainitic ferrite [23, 27].

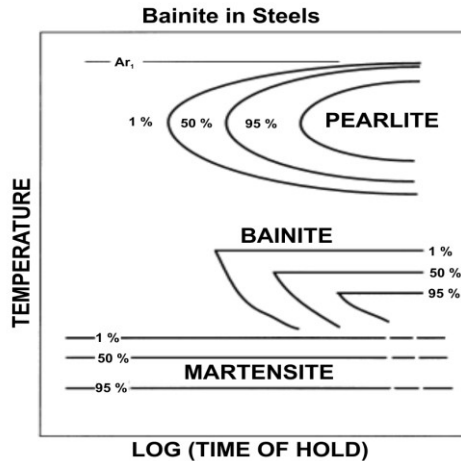


Figure 2-4 The schematics of TTT diagram illustrating the flat tops on the bainite C-curves [20].

It is generally accepted that carbide formation can be greatly affected by carbon partitioning from bainitic ferrite to austenite, however, the additional information is required to define the role of carbide formation in bainitic transformation kinetics and more details will be discussed in chapters 4 and 5.

2.2 Phenomenon of incomplete bainitic transformation and T_0 concept

In terms of the overall reaction kinetics, bainite has its own C-curve on the TTT diagram, between the pearlite curve and martensite curve and its C-curve of position depending on the alloying element content (Fig. 2-3). During the isothermal transformation, bainite and Widmanstätten ferrite are not distinguished at the nucleation stage. However, if a sufficient driving force is obtained for the displacive transformation, then the bainitic growth has two scenarios : *i*) the carbon partitioning may occur soon

after the growth by the displacive transformation or *ii*) the growth may occur by the displacive transformation with some carbon partitions to austenite, and the remaining carbon leaves the bainitic ferrite partially supersaturated [22]. These two processes (displacive transformation and carbon partitioning from ferrite to austenite) produce a carbide-free bainitic structure composed of bainitic ferrite and carbon-enriched retained austenite. The bainite formation then stops completely and austenite is no longer transformed to bainite even though a significant amount of untransformed austenite remains. This phenomenon has been defined as a transformation stasis or an incomplete

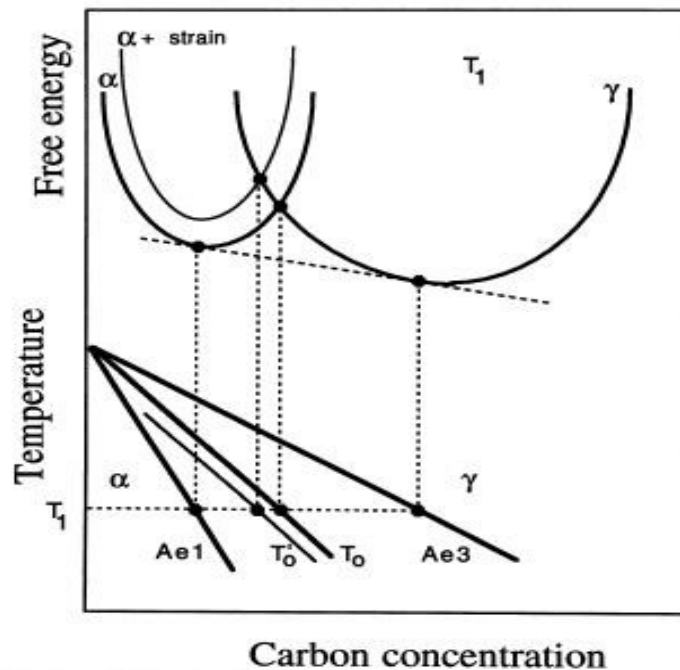


Figure 2-5 The schematic illustration of the origin of the T_0 curve on the phase diagram. The T_0' curve incorporates the strain energy term for ferrite, illustrated on the diagram by rising the free energy curve for ferrite by an appropriate quantity [20].

transformation since the direct transformation ceases before the system reaches the equilibrium composition [20, 22].

The transformation stasis is defined as a displacive transformation followed by an uphill diffusion from bainite to austenite [20, 22]. The displacive transformation becomes only possible when the free energy of ferrite and that of austenite have the same composition below T_0 . If the elastic strain energy of bainitic ferrite is considered, then T_0 curve is modified to be T_0' curve with the estimated strain energy of $400 \text{ J}\cdot\text{mol}^{-1}$ as shown in Fig. 2-4. The bainite in this case grows below T_0 and the direct transformation then becomes possible at the location of T_0' , and, possibly, the bainitic growth will be determined by T_0' . If the composition of the austenite shifts to the right due to an uphill diffusion, then the direct transformation becomes impossible and the full growth stasis occurs. However, in the presence of carbide formation, the growth stasis vanishes because carbide formation produces a decrease in the carbon concentration and shifts the location of T_0' to the left (Fig. 2-4) as the result of reducing the strain energy [26].

The experimental data at temperature $550 \text{ }^\circ\text{C}$ in Fig. 2-6 shows that in case of carbide formation, the transformation rate has three stages: the first stage up to time equal to 10^3 s , the transformation rate is fast and continues until the ferrite fraction reaches 0.35. At the second stage from 10^3 s to 10^4 s the transformation rate slows down and reaches the stasis at ferrite fraction equal to 0.4. The third stage begins after 10^4 s when the carbide formation is produced [28]. The formation of carbide reduces the carbon concentration, which increases the driving force that is responsible for continues the direct transformation. There is a strong indication that carbides are formed with coherent interfaces and with definite orientation relationships with ferrite [23, 26]. The strain

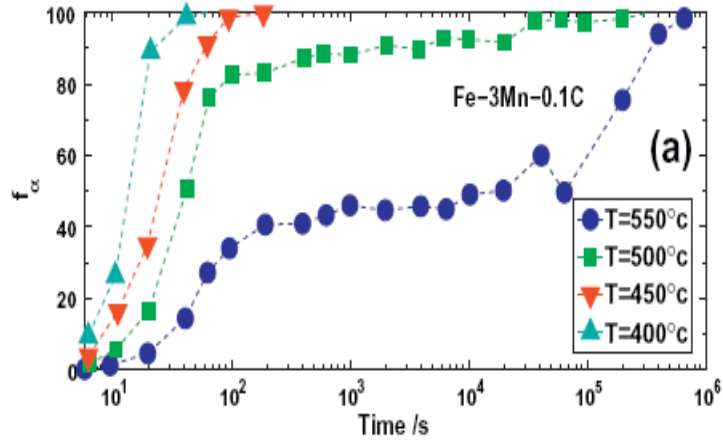


Figure 2-6 The fraction volume of ferrite vs time obtained at different temperatures for Fe-0.1C-3Mn alloy [28].

energy is proportional to $(\alpha) \cdot (1 - \alpha)$, which means that more transformation from austenite to ferrite occurs when the location of T_0' shifts to the left. However, when all retained austenite transforms to ferrite, the transformation is terminated and the effect of the strain energy vanishes (see chapters 4, 5 for more detail).

2.3 Bainite crystallography

If we consider the bainitic transformation as a displacive transformation similar to the martensitic transformation, then we can assume that 1) the orientation relationships between austenite and bainitic ferrite are close to either the Kurdjumov-Sachs (K-S) orientation relationships $(111)_\gamma // (110)_\alpha$ and $[01\bar{1}]_\gamma // [\bar{1}\bar{1}1]_\alpha$ [29, 30] or the Nishiyama-Wassermann (N-W) orientation relationships $(111)_\gamma // (110)_\alpha$ and $[\bar{1}\bar{1}2]_\gamma //$

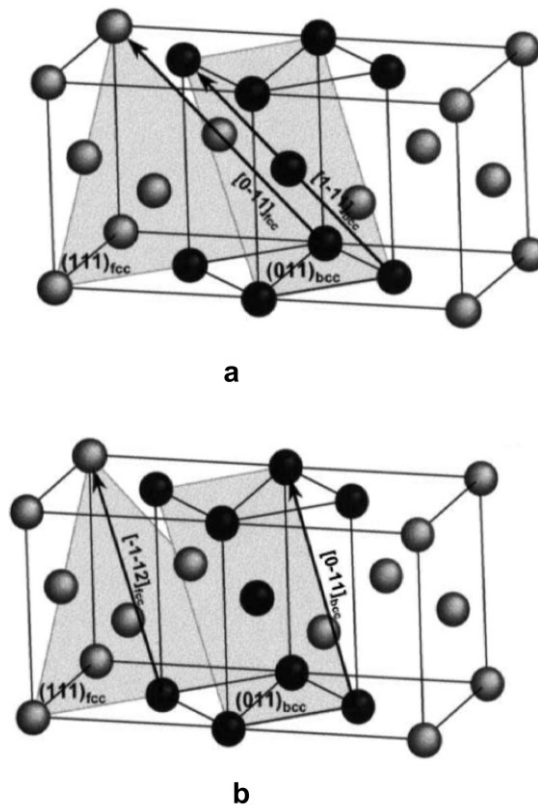


Figure 2-7 Orientation relationships between austenite (fcc) and ferrite (bcc) lattices: (a) K-S orientation relationships, (b) N-W orientation relationships [30].

$[0\bar{1}1]_{\alpha}$ $[30, 31]$ relationship, and 2) the transformation strain corresponds to the Bain strain [30, 32]. The coherent transformation from austenite to ferrite is produced with the Bain strain deformation in which the fcc structure of austenite is squeezed along one of $\{100\}$ direction and extended in the perpendicular plane to form the bcc structure of ferrite as shown in Fig. 2-5. The number of Bain strain variants and relationships between them are determined by the symmetry of parent phase (austenite). However, the Bain strain alone cannot create a coherent interface with the K-S or N-W orientation

relationships between phases and produce a continuous lattice. To accomplish this coherency between the $\{111\}$ closed packed plane of the fcc and the $\{110\}$ closed packed plane of the bcc, it is necessary to modify the Bain distortion by rotating the bcc crystal and adding shear. This results of the analysis of the orientation relationships and more details on the calculations of the Bain strain are presented in chapter 3 and Appendix A.

Chapter 3: The interaction between the displacive transformation and the diffusion process in the bainitic type transformation.

Abstract

The interaction between the displacive transformation and the diffusion process during the bainitic type transformation was studied using a phase field model incorporating both processes. A chemical free energy density function was derived to represent thermodynamic properties of low-alloy steels at high supercooling conditions at which the direct transformation from austenite to ferrite at a constant carbon concentration is possible. The results demonstrate that in such conditions both the displacive transformation and diffusional decomposition process may play important roles controlling the transformation kinetics and microstructure. A fast displacive transformation is dominant at the onset of the transformation; however, the diffusion-controlled decomposition can take control over the transformation kinetics and even the ferrite morphology at later stages as a result of the formation of a carbon enriched layer around ferrite grains. Both plate-like and rod-like shapes of ferrite grains can be obtained depending on the thermodynamic conditions and diffusion mobility.

3.1 Introduction

The nature of the bainitic transformation has remained a significant challenge for the theoretical materials science for a long time. The main problem for the development

of the theoretical or computational models of this transformation originates from the presence of two different factors controlling its development. On one hand, it has obvious features typical for the displacive transformations (such as the martensitic transformation), i.e., definite orientation relationships between austenite and ferrite, and the shape of ferrite dictated by the minimization of elastic energy [20, 33-35]. On the other hand, it has features typical for diffusion-controlled transformations, i.e., thermally activated kinetics, non-uniform distribution of carbon between austenite and ferrite after the transformation, and the formation of carbides during the transformation [19, 20, 36-38].

The bainitic transformation kinetics can demonstrate a stasis effect [39, 40] during which the transformation slows down or stops; however, after a time period it reaccelerates and reaches completion. Such a two-stage development of the transformation may result from the changes in the factors controlling the transformation rate.

Several models of bainitic transformation were proposed in [1-9, 41]; however, a number of important questions first formulated in still remain unanswered [42]. In particular, the question about the nature of the factors controlling the kinetics of the transformation and morphology of the microstructure produced by it still cause debates. Two opposing points of view have been presented: it was suggested that the transformation kinetics is completely controlled by the carbon diffusion process [5-9] with the morphology of the bainite structure controlled by the anisotropy of the ferrite austenite interface [9]. However, it was also proposed that the displacive mechanism of transformation plays the main role [1-4] with the transformation kinetics controlled by

the bainite nucleation kinetics (which can be described by a model presented in [9]) and with any carbon partitioning playing a secondary role in the transformation process [10, 36, 41, 43].

The models based on the displacive transformation are strongly supported by the established relationship between the temperature below which the bainitic transformation becomes possible and the carbon concentration in austenite [11]. Recent experimental studies provide a strong evidence in favour of the displacive mechanism control of the bainite formation [11, 44]; however, the diffusion process also is undeniably present during the transformation.

In [45, 46] the model describing the steady state growth of a ferrite grain with the shape of a parabolic cylinder was developed. In this model the energy dissipation by both diffusion and structural transformation processes was taken into account and the possibility of the ferrite growth with an incomplete partitioning of carbon between ferrite and austenite was demonstrated. In this case the overall transformation kinetics was completely controlled by the growth rate instead of the nucleation. Thus, both the deformation process and the diffusion process can be playing important roles simultaneously. The computational methods are necessary to introduce models with the displacive structural transformation and the diffusion decomposition process taken into account together in the model where the microstructure evolution is considered directly at the microscopic level. Such computational models can be used to study a process with a complicated morphology of the microstructure and without any imposed assumptions about the shape of phases.

The phase field method [15-17, 47] provides a powerful tool for the simulation of microstructural processes. It is especially suitable for the transformations involving significant strain effects with coherence strains producing a large strain energy. In this case the micromechanics model [18] utilizing the Fast Fourier transform method for the calculation of the elastic energy [16, 17, 47, 48] provides for the highest computational efficiency in comparison with other computational methods.

The phase field model was used in [9] for the simulation of the bainitic transformation in TRIP steels. However, in this study only the diffusion control of the microstructure evolution was simulated and the morphology of the bainitic pattern was controlled through the anisotropy of the interface energy and mobility of the austenite-ferrite interface. Thus, the presence of the transformation strain and its effect on the transformation kinetics and morphology of the bainitic pattern was not taken into account. Also, a number of phase field models were developed for martensitic transformations in which the transformation strain similar to that in the bainitic transformation was taken into account, but without any decomposition effects [16, 47-49]. The phase field method can be used to develop a transformation model in which both the transformation strain and decomposition effect are taken into account [50-53]. In [53] the analysis of possible scenarios for the development of decomposition accompanied by the displacive transformation was performed. It was shown that in the same system of alloys with different compositions three transformation paths are possible: 1-The path in which a fast displacive transformation plays the leading role (in case when the energy of the product phase is below the energy of the parent phase with the same composition); 2-The path where decomposition should occur first to allow the displacive transformation

to be produced, however, with decomposition developing by a fast spinodal mechanism.

3- The path where decomposition occurs first by a slow discontinuous mechanism, and, after that a displacive transformation is produced. It is clear that the bainitic transformation follows the first path because it becomes possible only when the temperature is below T_0 at which the free energy of ferrite is the same as the sum of the free energy of austenite with the same composition and the stored energy produced by the transformation strain. In this study we have used a phase field model of combined decomposition and displacive transformations following such a transformation path.

3.2 Phase field Model

3.2.1 Order parameters and transformation strains

The microstructure state is described in the phase field model by the distribution of three order parameters, η_1, η_2, η_3 , and by the distribution of carbon concentration c . The phase state at any point in the system is determined by the order parameter values. If all the three order parameters at some point have values close to zero then that point is in the state of the parent phase (austenite). If one of the order parameters has a value close to one and the values of the other two are close to zero, then the phase state corresponds to the transformation variant of the product phase (ferrite) associated with the non-zero order parameter. While the states with two or three order parameters with significantly non-zero values are in principle possible, such states will have a prohibitively high energy according to the energy density function described below and, as a result, they are

not realized in the model. The values of the order parameters also determine the transformation strain (stress free strain), according to:

$$\varepsilon_{ij}^0 = \sum_{n=1}^3 \eta_n \cdot \varepsilon_{ij}^{00}(n) \quad (3-1)$$

where $\varepsilon_{ij}^{00}(n)$ is the transformation strain corresponding to the transformation variant number n . For the austenite to ferrite transformations, as can be found in appendix, there are three different transformation strains (Bain Strains) corresponding to three different transformation variants:

$$\varepsilon_{ij}^{00}(1) = \begin{bmatrix} 0.137 & 0 & 0 \\ 0 & 0.137 & 0 \\ 0 & 0 & -0.196 \end{bmatrix} \quad (3-2)$$

$$\varepsilon_{ij}^{00}(2) = \begin{bmatrix} 0.137 & 0 & 0 \\ 0 & -0.196 & 0 \\ 0 & 0 & 0.137 \end{bmatrix} \quad (3-3)$$

$$\varepsilon_{ij}^{00}(3) = \begin{bmatrix} -0.196 & 0 & 0 \\ 0 & 0.137 & 0 \\ 0 & 0 & 0.137 \end{bmatrix} \quad (3-4)$$

There are significantly more (up to 24) γ - α orientation relations produced by the combination of transformation strains and rotations. However, in the phase field model, only transformation strains are required as input parameters. The rotations are added by

the model automatically in the process of the simulation to maintain a continuity of the lattice [16, 18, 48].

3.2.2 Energy functional

The free energy of the system is described by the energy functional:

$$E = E^{Chem} + E^{Elast} \quad (3-5)$$

where E^{Chem} is the chemical free energy and E^{Elast} is the elastic energy. The E^{Chem} is presented as a functional:

$$E^{Chem} = \int_V f[c(\mathbf{r}), \eta_p(\mathbf{r})] + \frac{1}{2} \beta_\eta \cdot [\nabla \eta_p(\mathbf{r})]^2 + \frac{1}{2} \beta_c \cdot [\nabla c(\mathbf{r})]^2 d^3r \quad (3-6)$$

The $f[c(\mathbf{r}), \eta_p(\mathbf{r})]$ is the local chemical free energy density which is a function of the composition, c , and the order parameters, η_p with $p=1,2,3$. The second and third terms represent a part of the interfacial energy determined by the order parameter and concentration gradients with the corresponding gradient coefficients of β_η and β_c . We use the fourth-order Landau-type polynomial introduced in [53] for a generic decomposition-ordering or decomposition-displacive transformations to describe the local chemical free energy density as:

$$\begin{aligned}
f(c, \eta) = & \frac{1}{4} A_4 (c - c_d)^2 (c - c_i)^2 + \frac{1}{2} A_2 (c - c_d)^2 - \frac{1}{2} B_2 (c_{\tilde{\alpha}} - c) \cdot (\eta_1^2 + \eta_2^2 + \eta_3^2) \\
& - \frac{1}{3} B_3 (\eta_1^3 + \eta_2^3 + \eta_3^3) + \frac{1}{4} B_4 (\eta_1^2 + \eta_2^2 + \eta_3^2)^2
\end{aligned} \tag{3-7}$$

where c_i is close to the equilibrium composition of the austenite phase; $c_{\tilde{\alpha}}$ is close to the equilibrium composition of the product phase and c_d is close to the critical composition c_0 , where the matrix and product phases have the same free energy, and the transformation ceases at this concentration. We have fitted the coefficients in the free energy density polynomial to reproduce the thermodynamic properties of low alloy steels at two different temperature values.

3.2.3 Elastic energy

The elastic energy of the system with an arbitrary distribution of misfitting inclusions producing a field of the stress-free strain described by Eq. (3-1) under the stress-controlled boundary conditions is determined by:

$$E^{Elast} = \int_V \frac{1}{2} \cdot C_{ijkl} \cdot [\varepsilon_{ij}(\mathbf{r}) - \varepsilon_{ij}^0(\mathbf{r})] \cdot [\varepsilon_{kl}(\mathbf{r}) - \varepsilon_{kl}^0(\mathbf{r})] d^3r - \int_V \sigma_{ij}^{appl} \varepsilon_{ij}(\mathbf{r}) d^3r \tag{3-8}$$

where C_{ijkl} is the elasticity tensor; $\varepsilon_{ij}(\mathbf{r})$ is the total strain tensor, including the elastic part and stress free strain; and σ_{ij}^{appl} is the applied stress tensor. The elastic strain field has to be found in order to use Eq. (3-8). It can be found by using the FEM computational tools; however, a more computationally efficient method, based on the microelasticity

theory, was developed in [18, 54]. The microelasticity theory provides a solution satisfying the continuity condition and the stress equilibrium condition for the elastic strain distribution in the systems with $\varepsilon_{ij}^0(\mathbf{r})$ having an arbitrary heterogeneity on the microscopic scale while being homogenous on the macroscale. The latter requirement means that the details of the microstructure should be much smaller than the size of the system in which the transformation develops. The elastic energy can be presented, by using the microelasticity theory, as a functional of $\varepsilon_{ij}^0(\mathbf{r})$ which also depends on macroscopic strain $\bar{\varepsilon}_{ij}$, determining the overall change of the shape of the system [18, 47, 53, 55]:

$$E^{Elast} = \frac{1}{2} \int_V C_{ijkl} \cdot \varepsilon_{ij}^0(\mathbf{r}) \cdot \varepsilon_{kl}^0(\mathbf{r}) d^3r - \bar{\varepsilon}_{ij} \cdot \int_V C_{ijkl} \cdot \varepsilon_{kl}^0(\mathbf{r}) d^3r + \frac{V}{2} \cdot C_{ijkl} \cdot \bar{\varepsilon}_{ij} \cdot \bar{\varepsilon}_{kl} - \frac{1}{2} \cdot \int_{|\mathbf{k}| \neq 0} \frac{d^3k}{(2\pi)^3} e_i \cdot \tilde{\sigma}_{ij}^0(\mathbf{k}) \cdot \Omega_{jk}(\mathbf{e}) \cdot \tilde{\sigma}_{kl}^0(\mathbf{k})^* \cdot e_l \quad (3-9)$$

where $\Omega_{jk}(\mathbf{e})$ is the Green function tensor defined as $\Omega_{jk}(\mathbf{e}) = (C_{ijkl} \cdot e_i \cdot e_l)^{-1}$; \mathbf{e} is the unit vector in the reciprocal space ($\mathbf{e} = \mathbf{k}/|\mathbf{k}|$); $\tilde{\sigma}_{ij}^0(\mathbf{k}) = \int_V [C_{ijkl} \cdot \varepsilon_{kl}^0(\mathbf{r})] \cdot e^{-i\mathbf{k} \cdot \mathbf{r}} d^3r$; the superscript asterisk represents the complex conjugate; V is the system volume; and the integration in the reciprocal space in Eq. (3-9) is performed excluding volume $(2\pi)^3/V$ around the $\mathbf{k} = 0$ point. In the case the system is clamped, $\bar{\varepsilon}_{ij}$ can be different from the average transformation strain, $\bar{\varepsilon}_{ij}^0 = \frac{1}{V} \cdot \int_V \varepsilon_{ij}^0(\mathbf{r}) d^3r$, produced in the system at any particular moment. If the system has stress controlled boundary conditions, then the work

of external forces equal to $-V\sigma_{ij}^{appl} \cdot \bar{\varepsilon}_{ij}$ (where σ_{ij}^{appl} presents stresses produced by external loads) should be added to the energy functional and the elastic energy should be minimized with respect to $\bar{\varepsilon}_{ij}$. The minimization produces an expression for the energy in the form [56]:

$$\begin{aligned}
E^{Elast} = & \frac{1}{2} \int_V C_{ijkl} \cdot \varepsilon_{ij}^0(\mathbf{r}) \cdot \varepsilon_{kl}^0(\mathbf{r}) d^3r - \frac{C_{ijkl}}{2 \cdot V} \cdot \int_V \varepsilon_{ij}^0(\mathbf{r}) d^3r \cdot \int_V \varepsilon_{kl}^0(\mathbf{r}') d^3r' - \\
& \frac{1}{2} \cdot \int_{|\mathbf{k}| \neq 0} \frac{d^3k}{(2\pi)^3} e_i \cdot \tilde{\sigma}_{ij}^0(\mathbf{k}) \cdot \Omega_{jk}(\mathbf{e}) \cdot \tilde{\sigma}_{kl}^0(\mathbf{k})^* \cdot e_l - \sigma_{ij}^{appl} \cdot \int_V \varepsilon_{ij}^0(\mathbf{r}) d^3r - \\
& \frac{V}{2} \cdot C_{ijkl}^{-1} \cdot \sigma_{ij}^{appl} \cdot \sigma_{kl}^{appl}
\end{aligned} \tag{3-10}$$

corresponding to: $\bar{\varepsilon}_{ij} = \bar{\varepsilon}_{ij}^0 + C_{ijkl}^{-1} \cdot \sigma_{kl}^{appl}$. If the system is under the zero applied stress conditions, then Eq. (3-10) becomes equivalent to Eq. (3-9) under the $\bar{\varepsilon}_{ij} = \bar{\varepsilon}_{ij}^0$ condition.

3.2.4 Governing equation

The temporal evolution is governed by the time-dependent Ginzburg-Landau equation for $\eta_p(\mathbf{r},t)$ and the Cahn-Hilliard diffusion equation for $c(\mathbf{r},t)$ as follows:

$$\frac{\partial \eta_p(\mathbf{r},t)}{\partial t} = -L \frac{\delta E}{\delta \eta_p(\mathbf{r},t)} + \xi_{\eta_p}(\mathbf{r},t) \tag{3-10}$$

$$\frac{\partial c(\mathbf{r},t)}{\partial t} = M \nabla^2 \frac{\delta E}{\delta c(\mathbf{r},t)} + \xi_c(\mathbf{r},t) \tag{3-11}$$

where ∇ is the gradient operator; L and M are kinetic coefficients characterizing the long-range order relaxation rate and diffusional mobility, respectively; E is the total free

energy; $\frac{\delta E}{\delta \eta_p(\mathbf{r}, t)}$ and $\frac{\delta E}{\delta c(\mathbf{r}, t)}$ are the variational derivatives representing driving forces; and $\xi_{\eta_p}(\mathbf{r}, t)$ and $\xi_c(\mathbf{r}, t)$ are the random uncorrelated noise terms for order parameters and composition, respectively. The presence of this noise permits to model the thermal nucleation without any a priori assumptions about the geometry and spatial distribution of the concentration and order parameters in the nuclei.

3.2.4 Model parameters

The polynomial coefficients in Eq. (3-7) were fitted to reproduce the thermodynamic data on free energy based on Thermo-Calc software for low alloy steels at two different temperatures Fig. 3-1, Fig. 3-2, [55, 57]. It is convenient to describe the model parameters using the dimensionless values. The energy scale is defined by the difference between energy of γ phase and α phase with the same composition: $\Delta f_0 = f(c, 0) - f(c, (\eta_1=1, \eta_2=0, \eta_3=0))$ (Fig.3-1 and Fig 3-2). With this definition of Δf_0 the characteristic energy ratio, that determines the relative strength of elastic interactions, can be introduced as:

$$\zeta = \frac{\varepsilon_0^2 G}{2\Delta f_0} \quad (3-13)$$

where G is shear modulus and ε_0 is defined by:

$$\varepsilon_0 = \frac{a_t - c_t}{a_c} \quad (3-14)$$

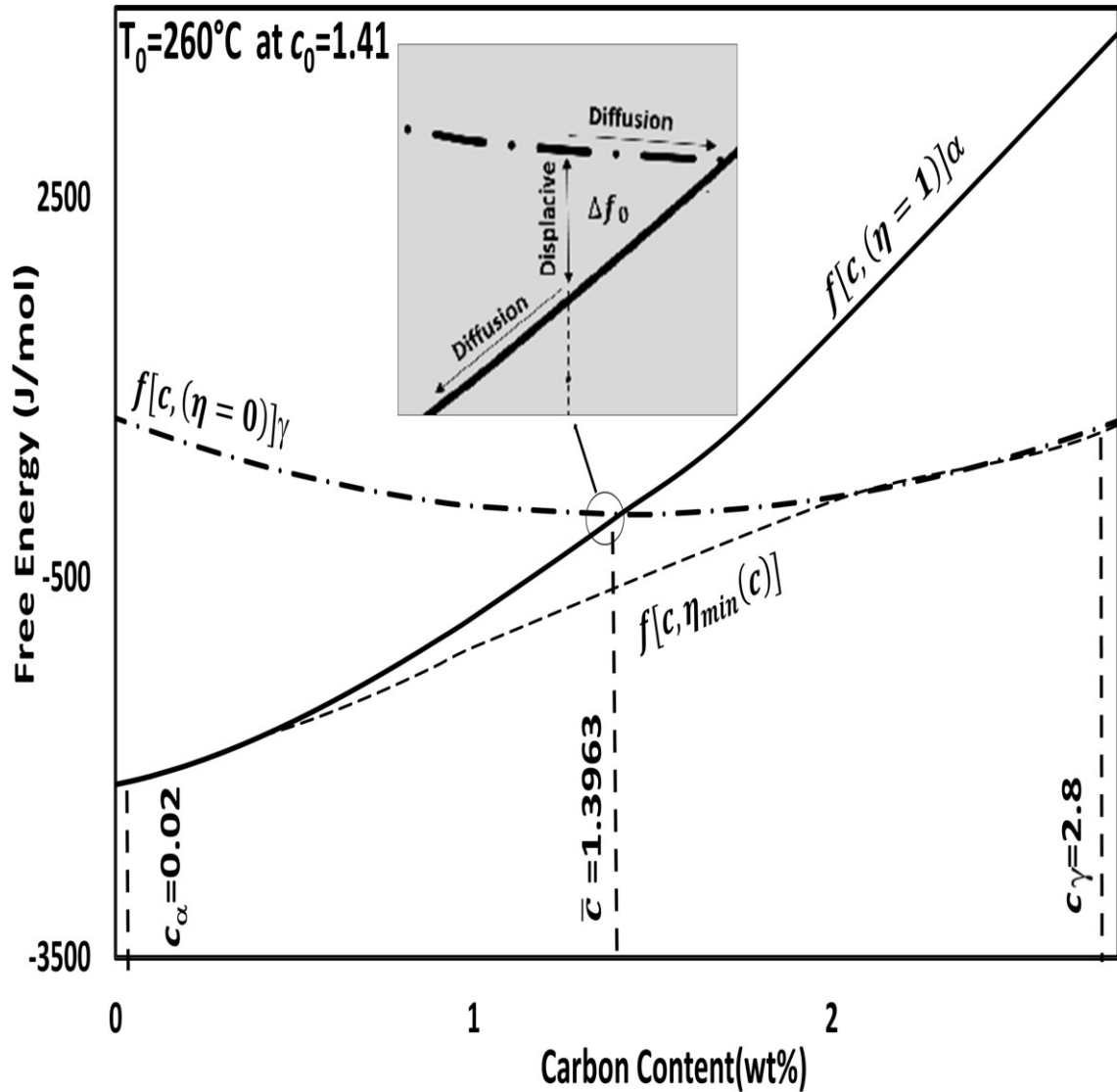


Figure 3-1. Free energy curves vs. carbon wt% plot for both the austenite and ferrite phase using Eq. (3-7) and the corresponding parameters obtained at 260 °C. Δf_0 is the free energy difference between the α and γ phases at the corresponding initial carbon content (\bar{c}), c_γ is the equilibrium carbon concentration in the γ phase, c_α is the equilibrium carbon concentration in the α phase and $\eta_{\min}(c)$ is the minima order parameter corresponding to the value of c at that point.

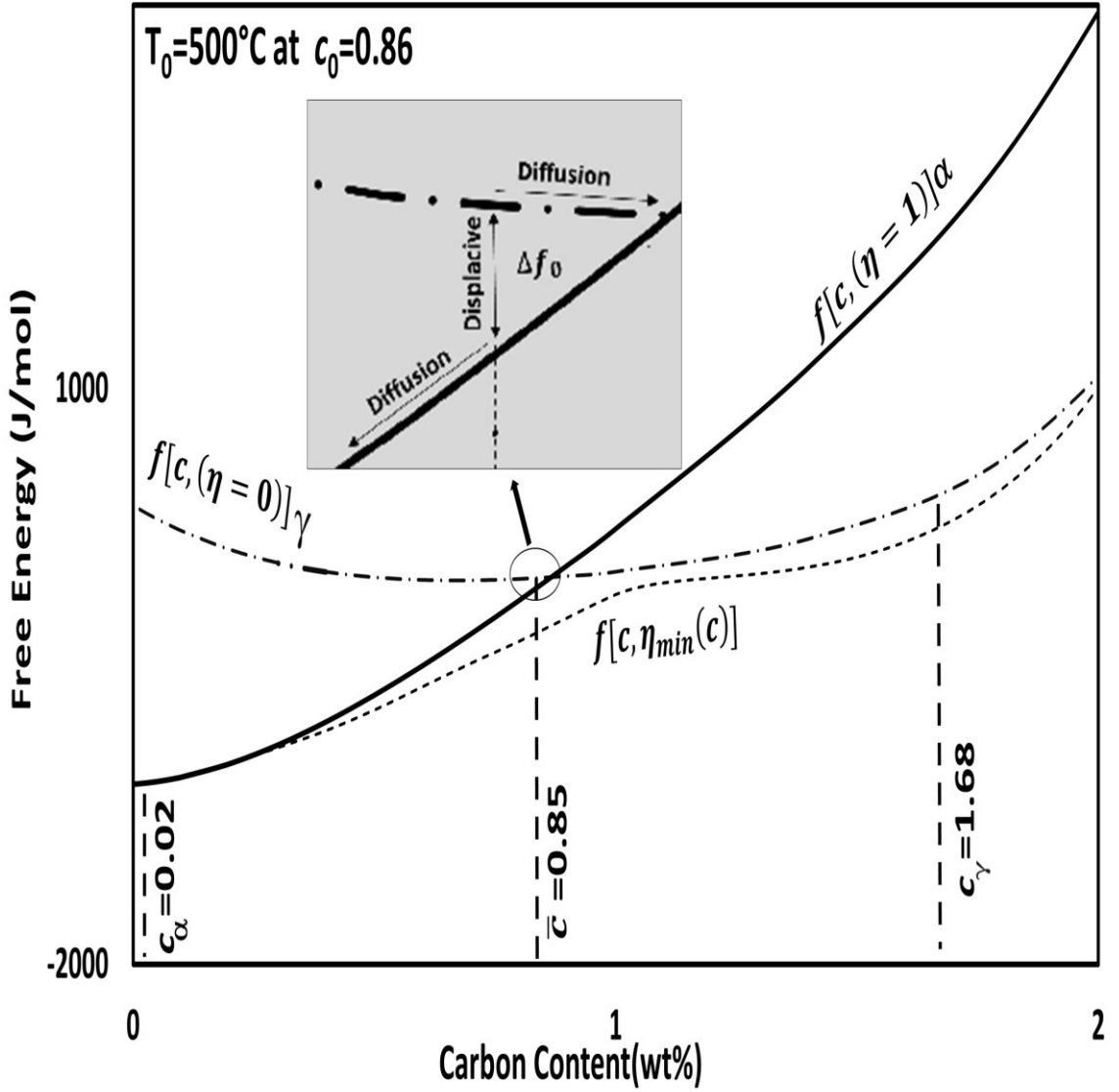


Figure 3-2. Free energy curves vs. carbon wt% plot for both the austenite and ferrite phase using Eq. (3-7) and the corresponding parameters obtained at 500 °C. Δf_0 is the free energy difference between the α and γ phases at the corresponding initial carbon content (\bar{c}), c_γ is the equilibrium carbon concentration in the γ phase, c_α is the equilibrium carbon concentration in the α phase and $\eta_{\min}(c)$ is the minima order parameter corresponding to the value of c at that point.

where a_c is the lattice parameter of austenite, c_t and a_t are lattice parameters produced by the cubic to tetragonal transformation Bain strain. The chemical free energy can be presented in the dimensionless form using reduced coefficients in Eq. (3-7) defined as dimensional coefficients divided by Δf_0 . Δf_0 depends on the alloy initial composition \bar{c} and as a result, coefficients in polynomial expansion for chemical free energy as well as ζ values depend on \bar{c} . We produced simulations using thermodynamic parameters corresponding to two different temperatures. For 260°C, simulations were performed for two \bar{c} values, i.e. $\bar{c} = 1.3963$ and $\bar{c} = 1.38$. These \bar{c} values corresponded to $\zeta = 1157$ and $\zeta = 500$, respectively, and to polynomial coefficient sets $A_4 = 9.457$; $A_2 = 20.804$; $B_2 = 158.87$; $B_3 = 1323.9$; $B_4 = 1323.9$; $c_d = 1.40$; $c_i = 1.5$; $c_{\tilde{\alpha}} = 0.02$ for $\bar{c} = 1.3963$; and $A_4 = 4.121$; $A_2 = 9.066$; $B_2 = 69.231$; $B_3 = 576.923$; $B_4 = 576.923$; $c_d = 1.40$; $c_i = 1.5$; $c_{\tilde{\alpha}} = 0.02$ for $\bar{c} = 1.38$. High values of the average carbon concentration were chosen so that the relative contributions of the elastic energy (ζ values) are high and the elastic interaction plays an important role in the transformation process. The dimensionless gradient coefficient can be defined as $\beta^* = \beta / (l_0^2 \Delta f_0)$, where l_0 is the mesh cell size. By choosing different β^* values the length scale of the model is controlled. We used $\beta_{\eta}^* = 1$ and $\beta_c^* = 80$. The time scale of the model and relative speed of deformation and diffusion processes are controlled by the dimensionless mobility coefficients. It should be mentioned here that the absolute values of mobility coefficients M and kinetic coefficients L are not important because they can be adjusted by changing the time scale, and only the ratio of these coefficients is important if we are interested in the final

structure and are not attempting to capture the true temporal evolution. The simulations were performed using the $64 \times 64 \times 64$ computational mesh and the $\bar{\varepsilon}_{ij} = 0$ conditions.

3.3 Results

3.3.1 Transformation development

The simulations in which only one transformation variant was allowed did not produce any nucleation of ferrite. The nucleation barrier can be overcome if the heterogeneous nucleation is allowed on the dislocations or near other defects, which produce a favorable strain field, to result in a stable embryo. However, even in that case at least two transformation variants are required for the growing ferrite embryo to accommodate the transformation strain [58], or, alternatively, the transformation strain accommodation can be achieved through plastic deformation. In our model with three transformation variants with the transformation strains presented in Eq. (3-2) - (3-4), the transformation strain accommodation was produced through the formation of the polytwinned structure in growing ferrite grains. Fig. 3-3 and Fig. 3-4 demonstrate the sequence of structures and composition distributions obtained in the systems with the thermodynamic parameters corresponding to 260°C (Fig. 3-1) and 500°C (Fig. 3-2). In both cases the diffusion mobility was equal to 0.1 and the characteristic energy ratio was equal to 1157, corresponding to different initial compositions in these two models. Different colours represent different transformation variants of ferrite and residual

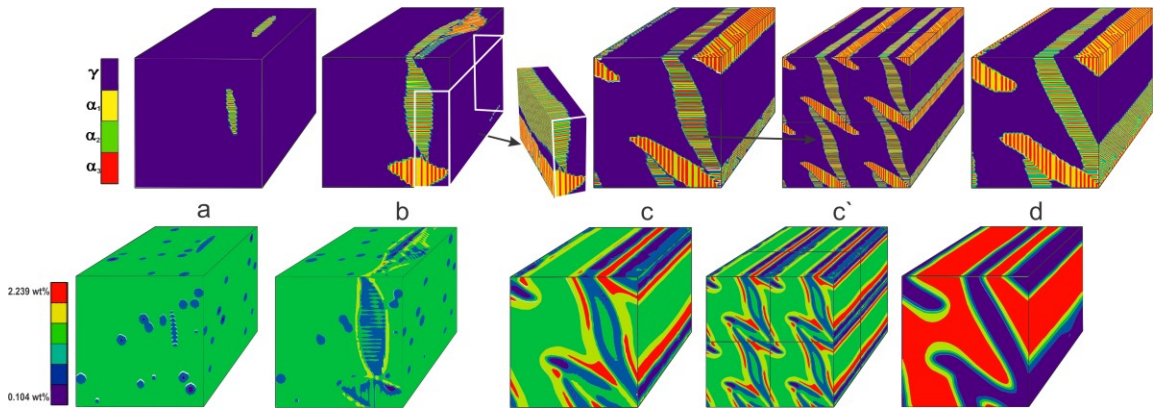


Figure 3-3. Structure sequences (upper) and respective distributions of the carbon concentrations (lower) at different reduced times; (a)-(d) corresponding to $t = 5, 10, 50, 10300$ in the system with the thermodynamic parameters corresponding to 260°C , $\zeta = 1157$ and $M = 0.1$. C' is the periodic repetition of the morphology to show the whole plate size.

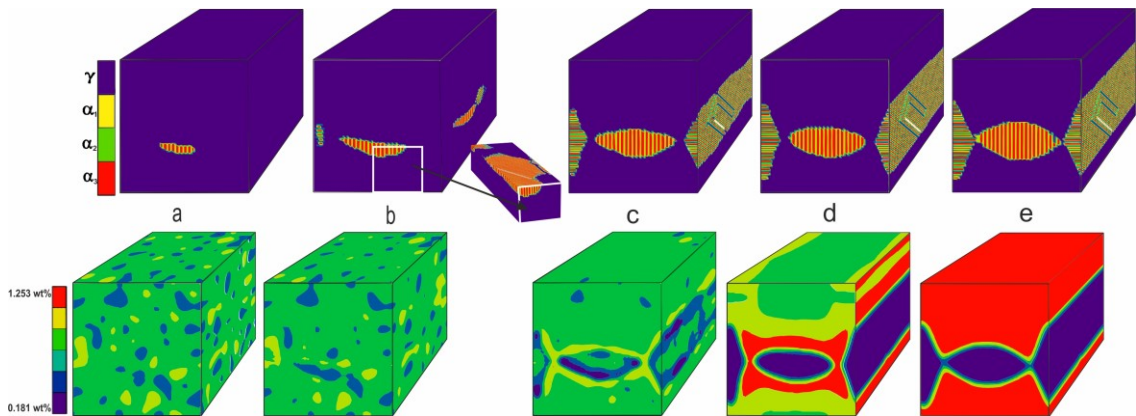


Figure 3-4. Structure sequences (upper) and respective distributions of the carbon concentrations (lower) at different reduced times; (a)-(e) correspond to $t = 20, 21, 25, 100, 671$ in the system with the thermodynamic parameters corresponding to 500°C , $\zeta = 1157$ and $M = 0.1$.

austenite in the microstructure pictures and different concentrations in composition distributions. In both cases the transformation starts with the formation of small nuclei of ferrite by the displacive mechanism. The carbon distribution remains unaffected by the transformation at this stage with concentration fluctuations resulting only from the noise applied to the system during the nucleation period. These concentration fluctuations are distributed randomly in the system and are not aligned in any way with the ferritic grains. The nucleated grains have polytwinned structure and plate-like shapes minimizing the elastic energy. The growth of these grains occurs fast in the in-plane directions, or, at least, in one in-plane direction if the plate-like shape is transformed into a rod-like shape during the growth. In the directions normal to the fast growth directions the increase in the thickness of plates and rods occurs slowly, and in this direction the decomposition starts to affect the growth. The carbon enriched layer is formed in austenite at the boundary between ferrite and austenite and when the concentration in this layer exceeds c_0 , further direct displacive transformation of austenite into ferrite becomes impossible.

Fig. 3-5 illustrates the evolution of the carbon concentration along the lines shown on the inserts representing the final carbon distribution maps. Initially, the decomposition produces only thin layers with the carbon concentration slightly increased in austenite relatively to the initial concentration and decreased in ferrite. The concentration in the enriched layer in austenite is higher than c_0 , and any further growth in the direction aligned with the line along which the concentration profiles are presented in Fig. 3-5 is diffusion controlled. In ferrite the carbon concentration at the interfaces with austenite is lower initially than at the center of the grain. As the transformation continues the difference between the concentration in austenite and ferrite increases and the

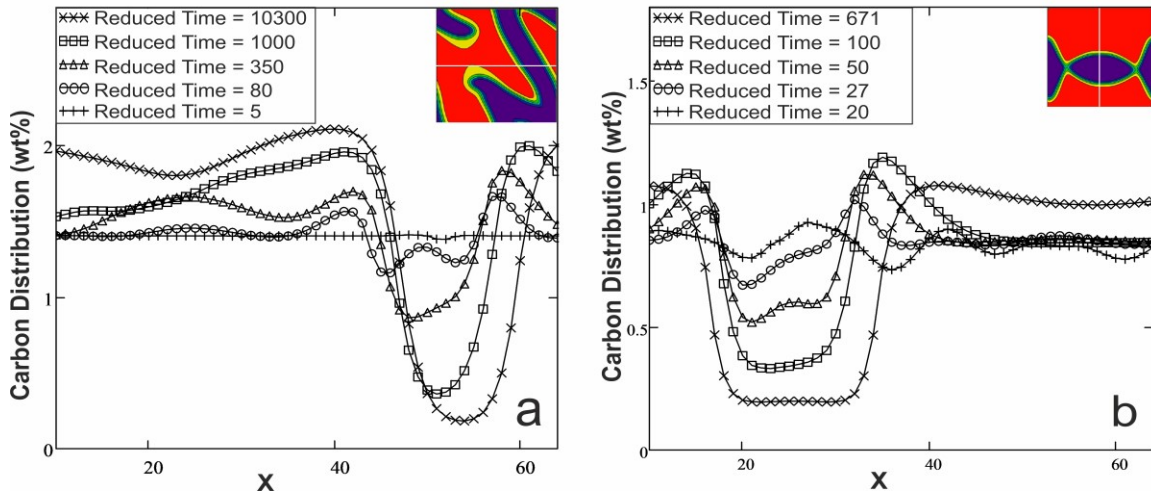


Figure 3-5. One dimensional distributions of the carbon concentration along the white lines shown in the inserts with two-dimensional concentration maps. The inserts demonstrate the final concentration distributions and the graphs show distributions at different moments of time. (a) distributions obtained in the system with the thermodynamic parameters corresponding to 260°C, $\zeta=1157$ and $M=0.1$. Spatial coordinate is counted along the white line on the insert from left to right. (b) distributions obtained in the system with the thermodynamic parameters corresponding to 500°C, $\zeta=1157$ and $M = 0.1$. Spatial coordinate is counted along the white line on the insert from bottom to top.

concentration minimum in ferrite shifts to the center of the grain. The maximum concentration in the carbon enriched layer in austenite at the interface with ferrite increases as does the thickness of that layer. Maximum carbon concentration c'_γ in the enriched layer at all times remains well below c_γ and minimum carbon concentration in ferrite c'_α remains well above c_α (c_γ and c_α are the equilibrium concentrations,

corresponding to the chemical free energy density function profile and unaffected by coherency strain effects, in austenite and ferrite, respectively (Fig. 3-1 and Fig. 3-2). At the end of the transformation austenite and ferrite acquire uniform concentration distributions with a high carbon concentration in austenite and a low carbon concentration in ferrite (Fig. 3-5 b); however, these concentrations are still significantly different from the corresponding equilibrium values c_γ and c_α .

Fig. 3-6 demonstrates the fraction of austenite as a function of time. It is clear that at both temperatures the transformation process has two stages. The fast stage in which most of the transformation is produced (from 0 to 50 time units for 260°C and from 0 to 25 time units for 500°C) and the slow stage in which the remaining transformation is produced (though at the end of the simulation a large amount of residual austenite is still found in the system). Such changes in kinetics suggest that at the first stage the transformation is fully controlled by the displacive mechanism and at the second stage the diffusional control of kinetics becomes more significant. Such a transition also corresponds to the changes in the carbon distribution demonstrated in Fig. 3-5. It can also be seen that after 10300 time units in the system with thermodynamic parameters corresponding to 260°C and 671 time units in the system with the parameters corresponding to 500°C, the transformation ceases and there are no changes in the volume fraction of austenite. Therefore, at the end of the simulation a state close to equilibrium is reached. However, the volume fraction of austenite is higher in both cases (0.61 at 260°C and 0.76 at 500°C) than the equilibrium fraction determined by \bar{c} , c_α and c_γ (0.5 at 260°C and 0.51 at 500°C).

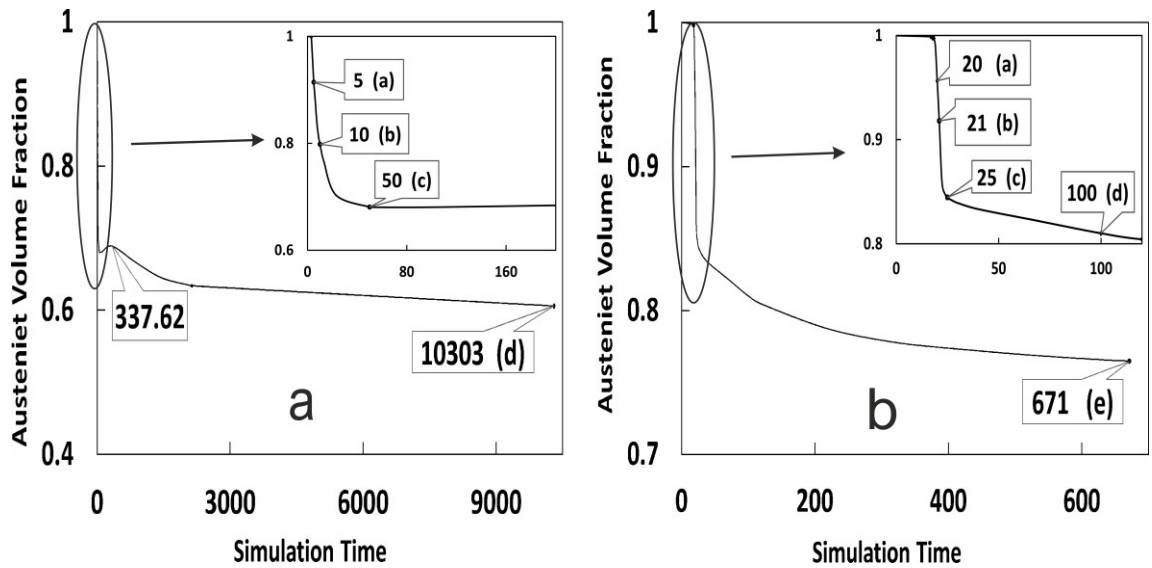


Figure 3-6. Dependencies of the austenite volume fraction on time obtained in the systems with (a) the thermodynamic parameters corresponding to 260°C, $\zeta=1157$ and $M = 0.1$. (b) the thermodynamic parameters corresponding to 500°C, $\zeta=1157$ and $M = 0.1$. The inserts show the initial high transformation rate stages with a higher temporal resolution.

3.3.2 Strain energy effect

Additional simulations were performed to investigate the effect of the characteristic energy ratio on the transformation and morphology of the product phase. The energy ratio was controlled by the changes in the initial concentration. The strain energy remained unchanged when the \bar{c} value was changed but the chemical driving force for direct displacive transformation rapidly increases. As a result, a small decrease in c resulted in a

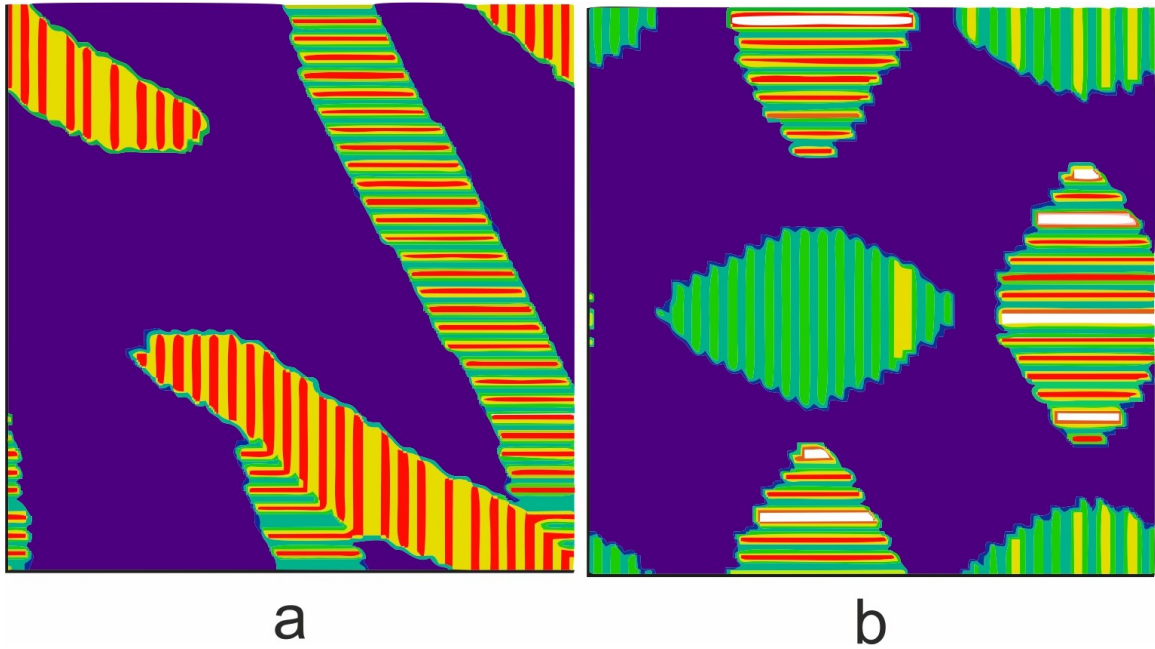


Figure 3-7. Different morphologies of final structures obtained with (a) the thermodynamic parameters corresponding to 260⁰C, $\zeta = 1157$ and $M = 0.1$. (b) the thermodynamic parameters corresponding to 260⁰C, $\zeta = 500$ and $M = 0.1$.

large change in the characteristic energy ratio. For the parameters corresponding to 260⁰C $\zeta=1157$ when $\bar{c}=1.3963$ and $\zeta=500$ when $\bar{c}=1.38$. Fig. 3-7 presents the cross-sections of the structures obtained with $\zeta=1157$ (Fig. 3-7 a) and $\zeta=500$ (Fig. 3-7 b). In both cases ferrite has the polytwinned structure and well defined habit planes which are almost exactly parallel to [011] axis and have the orientation between (210) and (320) or between (120) and (230) (the value of the third index may be nonzero, but it is much smaller than the values of the first two indices). Thus, the orientation of the habit plane is close to (15 10 3) which is predicted by the Bowles-Mackenzie and Wechsler-Lieberman-

Read theories and observed in some steels [59]. However, there are noticeable differences in the morphology of ferrite in these two systems. In the system with a high ζ value the ferrite grains have a plate-like shape, which is most favourable from the point of view of the reduction of the elastic energy. In the system with a reduced ζ value ferrite grains have a rod-like morphology, which is less effective for the reduction of the elastic energy, but more efficient for the growth limited by the diffusion.

3.3.3 Mobility effect

A strong effect of the characteristic energy ratio on the morphology of ferrite grains and obvious signs of a stronger diffusion control over the morphology when the elastic energy role is decreased motivated us to study the mobility effect on the transformation. Fig. 3-8 demonstrates the final structures and respective distributions of carbon concentrations in the systems where in thermodynamic parameters correspond to 260°C, $\zeta=1157$ and the diffusion mobility coefficient values 0.01, 0.1 and 1 (the structural mobility coefficient was equal to 10 in all simulations). The structures obtained with $M=0.01$ and $M=0.1$ were identical in the qualitative sense. In both cases plate-like shapes are produced with the same types of habit planes. These shapes indicated a complete control of the elastic energy over the morphology, even though in the system with $M=0.1$ the decomposition starts relatively early in the transformation process and produces enriched layers blocking the direct displacive transformation. In the case of the system with $M=1$, ferrite grains have a rod-like shape with almost equiaxed cross-sections. The

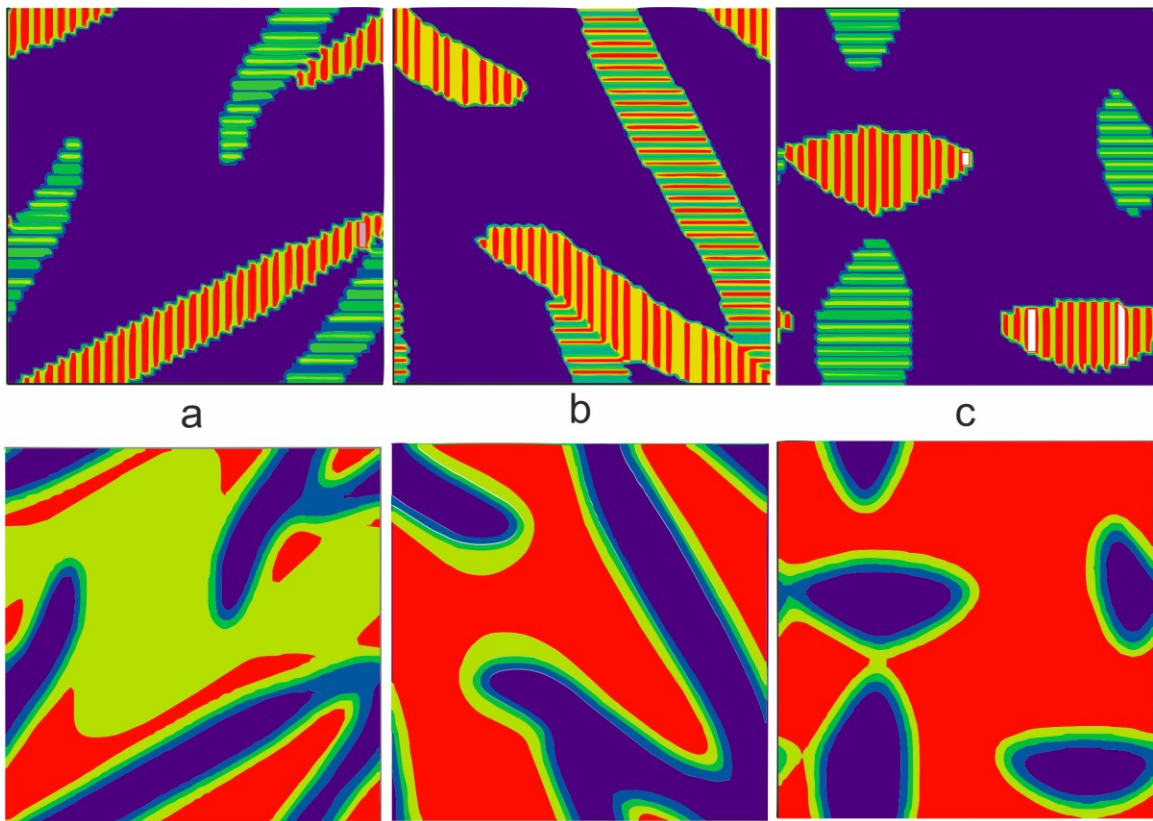


Figure 3-8 Morphologies of final structures (upper) and respective distributions of the carbon concentrations (lower) at 260⁰C with (a) the thermodynamic parameters corresponding to $\Delta G = 1157$ and $M = 0.01$. (b) the thermodynamic parameters corresponding to $\Delta G = 1157$ and $M = 0.1$. (c) the thermodynamic parameters corresponding to $\Delta G = 1157$ and $M = 1$.

habit planes are not well defined in this case as the surface of ferrite grains has a significant curvature and different grains have a noticeably different shape of the cross-sections. The structure obtained in this system demonstrates signs of more significant

effect of diffusion on ferrite morphology in comparison to the systems with $M=0.01$ and $M=0.1$.

3.4 Discussion

The simulation results demonstrated that if the transformation develops at the temperature below T_0 (corresponding to initial uniform composition \bar{c}), then the displacive mechanism may play a leading role and to a significant extent determine the morphology of the produced structure. Such a leading role of the displacive mechanism was suggested in [1-4] and experimentally demonstrated in [19, 44, 60]. However, our results also clearly show that the decomposition eventually produces sufficiently strong changes in the concentration distribution and forms carbon enriched layers at the austenite - ferrite interface. The formation of such layers changes the kinetics of the growth to that of a slow, diffusion-controlled process. At the end of the fast stage of the transformation, 0.16 to 0.3 of austenite was transformed. In the second, slow stage the nonzero rate of the transformation was produced leading to further reduction in austenite to the volume fraction of 0.61 to 0.76; the second stage can also result in large changes in the shape of ferrite grains (Fig. 3-3 b, c, d). However, the rate of the transformation at the second stage was lower than in the first by orders of magnitude. Such slowing down of the transformation up to a complete stasis was observed in some steels [39, 40] and attributed to the carbon partitioning effects [38, 39]. At the second stage of the transformation process, diffusion plays an important role controlling its kinetics, however, transformation strains and the elastic energy can still be important. They can

continue dictate the evolution of the morphology as can be seen from Fig. 3-3. The transition from the structure shown in Fig. 3-3 a to that in Fig. 3-3 b and finally to the structure shown in Fig. 3-3 d occurred after the formation of carbon enriched layers when the transformation rate is slow (Fig. 3-3 a). However, in this process the orientation of ferrite plate-like grains changes so that their habit planes become close to those corresponding to the minimum of the elastic energy. Thus, even though the transformation kinetics is controlled by diffusion, the shape of ferrite grains is dictated in this case by the strain energy minimization. The transformation strain may affect not only the morphology of the transformation product, but also the conditions of equilibrium between austenite and ferrite.

The difference between the minimum concentration obtained in ferrite c'_α and equilibrium concentration c_α as well as between the maximum concentration produced in austenite c'_γ and equilibrium concentration c_γ may be caused to some extent by kinetic factors, but such a difference can be also caused by the presence of the transformation induced strains (also known as coherency strains) [61] as a result of changes in Gibbs energy associated with the non-uniform distribution of elastic strains in the system. The distributions of the carbon concentration shown in Fig. 3-5 b demonstrate that: 1- at the end of the transformation process carbon distributions in both ferrite and austenite have become close to constant values and 2- that between $t = 100$ and $t = 671$ the maximum concentration of carbon in austenite decreased as the carbon from the enriched layer spread through the entire volume of residual austenite. A close to constant concentration of carbon in austenite, having a decreasing with time maximum value, indicates that the

deviation of the concentration from the nominal equilibrium value, predicted by the thermodynamic equilibrium in the absence of the coherency strain, is caused by thermodynamic reasons rather than kinetic effects. Similar deviations of the carbon concentration in ferrite and austenite from nominal equilibrium values corresponding to the equilibrium without misfit strain effects were observed experimentally and, therefore, the transformation strains and the associated with them strain energy might play a significant role in controlling the thermodynamic parameters that directly affect the diffusion process.

Now we can address the main question which motivated our study, which phenomenon (i.e., the displacive lattice transformation or the diffusion decomposition process) plays a more important role in the transformation of the bainitic type and controls the microstructure produced by it (or which of the displacive [1-4] and diffusion [5-9, 37] model may better describe this process)? Our results demonstrate that both the displacive transformation and decomposition may be playing important roles in the transformation of the bainitic type and that can be strong interactions between these processes. On the one hand, decomposition may take over the control of the transformation kinetics, while the strain energy may still control the shape selection, or even the shape control can also become dominated by the effects of the diffusion limited growth. On the other hand, coherency effects on the equilibrium between phases may change the compositions of the phases corresponding to the minimum energy of the system and, thus, change the phase fractions which can be produced by decomposition. Therefore, both the transformation strains and diffusion-controlled decomposition should be included into the transformation model. The effect of the diffusion mobility on the

strength of the diffusion control over the transformation may seem counterintuitive. When the diffusion mobility is very low, the transformation process and morphology of the product phase are dominated by the transformation strain effects, and below a definite value of the diffusional mobility the transformation outcome becomes insensitive to the reduction of mobility. However, such a trend should be expected when the transformation has thermodynamic parameters typical for the bainitic transformations, i.e., when the initial temperature is below T_0 . In this case, if diffusion stops completely, the transformation still may proceed because the free energy of austenite is higher than the free energy of ferrite with the same composition. In unconstrained system the transformation can produce a state with 100% of a single transformation variant, as is expected in a perfect martensitic transformation [48, 62]. The nontrivial microstructure and any residual austenite can be obtained in this case only if there are constraints imposed on the martensitic transformation by clamping [48], by the grain structure in a polycrystalline material [47, 62] or by other defects. A completely transformed state with the same composition as the parent phase will have a higher energy than a two phase mixture of the parent phase and the product phase with a corresponding equilibrium concentration. The increased diffusion mobility is necessary to produce more equilibrium states with a non-uniform composition, and a sufficiently high diffusion mobility is necessary to achieve conditions with the diffusion controlling not only the rate, but also the morphology of the product phase. However, it can be expected that in the limit of the infinite diffusion mobility the morphology will again be controlled by the strain energy minimization. A relative importance of the diffusion and strain energy control over the morphology of ferrite grains can also be affected by the characteristic energy ratio (the

ratio of the transformations strain energy to the driving force for the direct diffusionless displacive transformation). The decrease in the ratio corresponds to the decrease of the carbon concentration in austenite at given temperature or the decrease in the isothermal transformation temperature for an alloy with a given carbon concentration in austenite, and the ferrite morphology changes from a plate-like to a rod or lath like. Such a transition occurs in real steels when the transformation temperature decrease, the transformation has a significantly higher driving force, and the morphology control is less significantly dominated by the strain energy reduction and has a stronger contribution from the diffusion control producing the shapes that are more favourable for the diffusion limited growth.

3.5 Conclusions

In our study, we have used a phase field method to investigate the roles of two processes, i.e. the displacive transformation and the diffusion process, in the bainitic type transformation, and the interaction between these processes. The obtained results allow us to draw the following conclusions:

1. A transformation may develop as a two-stage process. At the first (fast) stage, the displacive mechanism plays a leading role by controlling the rate of the transformation and morphology of ferrite grains. At the second (slow) stage, the development of carbon enriched layers around the ferritic grains changes the kinetics control to the diffusion process.

2. The morphology of ferrite is either controlled by the strain minimization at both stages, resulting in a plate-like shape of ferrite grains, or, in cases of a lower strain energy and a sufficiently high diffusion mobility, the morphology control can be overtaken by the diffusion process, producing rod-like shapes of ferrite grains favored by the conditions of the high rate of the diffusion limited growth.
3. The coherency strains and the stresses caused by it affect the equilibrium conditions for carbon concentrations at the boundary between the ferrite grain and surrounding austenite, resulting in a higher concentration in ferrite and a lower concentration in austenite than the corresponding concentrations predicted by the stress-free thermodynamic model. Such a change in the concentration conditions at the interphase boundary may produce a significant effect on the diffusion limited growth.
4. Both the diffusion process and displacive transformation producing coherency strain effects should be included into the model of the transformation of the bainitic type

Chapter 4: The interaction between the carbon partitioning and carbide nucleation inside austenite during the bainitic type transformation.

Abstract

The interaction between the displacive transformation, carbon partitioning and carbide nucleation inside austenite during a bainitic type transformation was studied using a phase field model incorporating the displacive transformation and diffusion processes. The carbide nucleation was modeled as a formation of carbon sinks inside austenite with different nucleation sequences. The results obtained with different nucleation sequences demonstrate that carbide nucleation may play a secondary role controlling the transformation kinetics and microstructure evolution after the fast transformation stage completion; however, elastic interactions can control the ferrite morphology even at a later stage, thus leading to the change of the ferrite grain shape from a rod-like to plate-like. A rate of the carbide nucleation and the number of nucleated carbides controlled the extension of the stasis period separating the fast and slow transformation stages and the rate of the transformation after the stasis or during a temporary slowdown period. Results show that the transformation can proceed through several slowdown - acceleration periods.

4.1 Introduction

Among different austenite decomposition transformations, the bainitic transformation has the nature, which is probably the most complex to understand. The morphology and crystallography of bainite and the transformation kinetics have been intensively studied over a long time, but some unresolved problems still remain. In particular, the roles of diffusion process and the displacive mechanism in the control of the (i) kinetics of the transformation of austenite into bainite and (ii) morphology of bainitic ferrite as well as the interaction between the diffusion processes and carbide precipitation are still under debate. A number of theoretical and experimental studies have been carried out to investigate whether the diffusion process [9, 63] or the displacive transformation process with the shape of ferrite dictated by the minimization of elastic energy [3, 11, 20, 44, 64], control the bainitic transformation kinetics and bainite morphology, or whether both processes are equally important [65]. These two processes produce a carbide-free bainitic structure composed of bainitic ferrite and carbon-enriched retained austenite. However, the formation of carbides during the transformation cannot be ruled out as it is often observed during the partitioning step in low and high carbon steels [66-68] and even in steels with a high concentration of Si, which usually suppresses the carbide formation in austenite [19, 69-72] (though it is assumed that in this case, carbides are formed inside ferrite only). It has been suggested that generally carbide might precipitate (1) within carbon enriched austenite, (2) in the subunits of ferrite and (3) on the interphase boundaries between ferrite and austenite [20,

21, 25, 26, 73-77]. Also in some cases, the carbide formation can be found in both austenite and bainitic ferrite [73].

There are a few experimental studies of the carbide formation in austenite during the bainitic transformation [24, 25, 67, 78-82]. It was suggested in [78] that the decomposition of retained austenite into bainitic ferrite and carbide occurs by a diffusion process, which is similar to the mechanism of the pearlite formation, and due to a fast carbon partitioning between austenite and bainitic ferrite, the carbide particles obtained have long rod shapes. During the quenching and partitioning heat treatment of medium carbon steels described in [67], the fraction of the retained austenite curve demonstrates two peaks. The first one appears at the onset of the partitioning process when a rapid escape of carbon from martensite to untransformed austenite leads to a fast increase in the fraction of retained austenite. The second peak is produced at the intermediate partitioning times; it has been suggested that this peak may be associated with the resolution of carbides formed at lower transformation temperatures. The carbide formation during the bainitic transformation may also result in a multistage transformation with the stasis and acceleration periods [81]. The carbide formation inside austenite can result from the carbon partitioning between ferrite and austenite, and leads to the development of bainitic ferrite as a diffusion-controlled ledge-wise growth [25]. In this case, carbides may grow cooperatively with ferrite during the diffusion-controlled propagation of ledges on the ferrite-austenite interface [25, 82]. As a result of this process, some carbides, which are initially formed in austenite near the interface with ferrite, are eventually surrounded by ferrite, and it may be impossible to determine from the observations of the final microstructure in which phase carbides were formed. The results of metallographic

studies were used in [24] to propose that the formation of carbide in austenite might trigger further growth of bainitic ferrite, and carbide might play a subsequent role after the formation of bainitic ferrite by a displacive transformation. However, the investigations of the kinetics of the bainitic transformation, mentioned above, also indicate a need for further examination since some of the factors controlling the transformation kinetics could not be directly assessed experimentally. There are only a few studies focusing on the interaction of the carbide precipitation and the carbon partitioning process including the stasis phenomena which can be observed during the bainitic transformation [83]. The bainitic transformation can experience a stasis period during which the transformation slows down significantly or stops completely; however, after a period of time, the carbide nucleation can reaccelerate the transformation by reducing the concentration of carbon in the residual austenite; and then the transformation reaches completion [28, 39, 83]. It has been suggested that such a two-stage development (and, in some cases, even a multistage development [81]) of the transformation may result from the changes in the factors controlling the transformation rate, and a model including the carbide nucleation during the bainitic transformation may be necessary [76].

Several theoretical and computational models were proposed in the literature [79, 84-86] to describe the formation of carbides in austenite during the bainitic transformation. [79] used diffusion models of a plate shaped ferrite growth, developed in [87], to determine the overall kinetics of bainite, and reported a good agreement of the bainitic growth rate with the experimental data. The carbide precipitates in that model act as carbon sinks within austenite and such a sink was added near the austenite ferrite

interface behind the tip of the growing ferrite grain. A phase-field method coupled with a diffusion model was used in [85] for the simulation of the upper and lower bainitic transformation including the carbide formation. However, in that study, the elastic energy produced by the displacive transformation was not included into the model, and the transformation kinetics and the morphology of ferrite grains were controlled by the carbon diffusion and the precipitation of carbides. The formation of bainitic ferrite and carbide precipitation in TRIP steel were modeled in [86] using a nucleation-growth based model. This approach predicted the kinetics of the bainite formation for one alloy steel at different cooling conditions. However, the model did not consider the uphill diffusion during the bainitic transformation and neglected the effect of the strain energy. None of the models discussed above included the displacive transformation mechanism and thus omitted the elastic energy contribution into the control of the transformation. In the present work, the methodology used in [65] to study the displacive transformation accompanied by the partitioning of carbon between ferrite and austenite is modified to include the nucleation of carbides in austenite with the goal to investigate the influence of the carbide formation on the bainitic transformation kinetics and the morphology of bainite.

4.2 Phase field modelling

In this study, the phase field model is used to describe the bainitic transformation in the case wherein the displacive transformation, carbon partitioning from ferrite to austenite and carbide formation in austenite may occur simultaneously without any

imposed assumptions about the shape of phases and without imposing any artificial constraints on the sequence of the processes.

4.2.1 Transformation variants and order parameters

We use the same phase field approach as in [65] to describe the microstructure, formed by austenite and ferrite, using the distributions of three order parameters, $\eta_1(\mathbf{r})$, $\eta_2(\mathbf{r})$, $\eta_3(\mathbf{r})$ and the carbon concentration $c(\mathbf{r})$. The structural phase state at any location \mathbf{r} is determined by the η_1 , η_2 and η_3 values at this location. If all the order parameters at point \mathbf{r} have values close to zero, then that point has a crystal structure of austenite. If a value of one of the order parameters is close to one while the other two have values close to zero, then the crystal structure at such a location corresponds to ferrite with the lattice orientation determined by the non-zero order parameter. The transformation strain (stress free strain) producing a ferrite lattice from austenite by a displacive mechanism with a coherent interface is determined by the order parameter values as:

$$\varepsilon_{ij}^0 = \sum_{n=1}^3 \eta_n \cdot \varepsilon_{ij}^{00}(n) \quad (4-1)$$

where $\varepsilon_{ij}^{00}(n)$ is the transformation strain tensor describing the deformation that produces the transformation variant number n from the austenite lattice. For the austenite

to ferrite transformation, there are three strain tensors (describing three Bain strains) corresponding to three transformation variants:

$$\varepsilon_{ij}^{00}(1) = \begin{bmatrix} 0.137 & 0 & 0 \\ 0 & 0.137 & 0 \\ 0 & 0 & -0.196 \end{bmatrix} \quad \varepsilon_{ij}^{00}(2) = \begin{bmatrix} 0.137 & 0 & 0 \\ 0 & -0.196 & 0 \\ 0 & 0 & 0.137 \end{bmatrix} \quad \varepsilon_{ij}^{00}(3) = \begin{bmatrix} -0.196 & 0 & 0 \\ 0 & 0.137 & 0 \\ 0 & 0 & 0.137 \end{bmatrix} \quad (4-2)$$

The number of different orientation relationships, which can be produced by this transformation, can be substantially larger (up to 24) as a result of the combination of transformation strains and rotations [88]. However, in the phase field model based on the micromechanics model, only the transformation strains are used as input parameters, while the rotations are added by the model during the simulation to satisfy the requirement of the crystal lattice continuity.

4.2.2 Energy functional and strain energy

The free energy functional consisting of two parts (chemical energy E^{Chem} and elastic energy E^{Elast}) is used in the model to describe the system energy:

$$E = E^{Chem} + E^{Elast} \quad (4-3)$$

The E^{Chem} functional is determined as:

$$E^{Chem} = \int_V f[c(\mathbf{r}), \eta_p(\mathbf{r})] + \frac{1}{2} \beta_\eta \cdot [\nabla \eta_p(\mathbf{r})]^2 + \frac{1}{2} \beta_c \cdot [\nabla c(\mathbf{r})]^2 d^3r \quad (4-4)$$

where $f[c(\mathbf{r}), \eta_p(\mathbf{r})]$ is the density of the local chemical free energy which depends on the local values of the order parameters and the carbon concentration. The remaining terms describe a contribution of the energy of the interfaces determined by the gradients of the order parameters and the concentration in which gradient coefficients β_η and β_c are used with the order parameter and the concentration gradients, respectively. For the $f[c(\mathbf{r}), \eta_p(\mathbf{r})]$ function the fourth-order polynomial is used in the form introduced in [53] for the generic decomposition - displacive transformations (or decomposition - ordering transformations) as:

$$f(c, \eta) = \frac{1}{4} A_4 (c - c_d)^2 (c - c_i)^2 + \frac{1}{2} A_2 (c - c_d)^2 - \frac{1}{2} B_2 (c_{\tilde{\alpha}} - c) \cdot (\eta_1^2 + \eta_2^2 + \eta_3^2) - \frac{1}{3} B_3 (\eta_1^3 + \eta_2^3 + \eta_3^3) + \frac{1}{4} B_4 (\eta_1^2 + \eta_2^2 + \eta_3^2)^2 \quad (4-5)$$

where c_i is the carbon concentration close to that of the concentration in the austenite phase in equilibrium with ferrite; $c_{\tilde{\alpha}}$ is the carbon concentration close to the equilibrium concentration in ferrite; and c_d is the carbon concentration close to the critical concentration c_0 , at which austenite and ferrite have the same energy (so that the carbon concentration in austenite be below c_0 to allow a direct displacive transformation without the diffusion decomposition). The elastic energy of the system with a heterogeneous

misfit-generating microstructure characterized by the stress-free strain under an applied stress can be determined by:

$$E^{Elast} = \int_V \frac{1}{2} \cdot C_{ijkl} \cdot [\varepsilon_{ij}(\mathbf{r}) - \varepsilon_{ij}^0(\mathbf{r})] \cdot [\varepsilon_{kl}(\mathbf{r}) - \varepsilon_{kl}^0(\mathbf{r})] d^3r - \int_V \sigma_{ij}^{appl} \varepsilon_{ij}(\mathbf{r}) d^3r \quad (4-6)$$

where C_{ijkl} is the elastic modulus tensor; $\varepsilon_{ij}(\mathbf{r})$ is the total strain tensor, including the elastic part and stress free strain $\varepsilon_{ij}^0(\mathbf{r})$; and σ_{ij}^{appl} is the applied stress tensor. We have used the micromechanics theory providing a solution for elastic strains, satisfying the continuity condition and the stress equilibrium condition, and the stresses in the material with misfitting inclusions based on the Fourier transform method presented in [18] and used for the simulation of phase transformations in different systems (for example, in [18, 47, 54, 65, 89]).

4.2.3 Governing equations

The evolution of the microstructure and composition is described by the Ginzburg-Landau equation for the order parameter distributions and the Cahn-Hilliard equation for the concentration field:

$$\frac{\partial \eta_p(\mathbf{r}, t)}{\partial t} = -L \frac{\delta E}{\delta \eta_p(\mathbf{r}, t)} + \xi_{\eta_p}(\mathbf{r}, t) \quad (4-7)$$

$$\frac{\partial c(\mathbf{r}, t)}{\partial t} = M \nabla^2 \frac{\delta E}{\delta c(\mathbf{r}, t)} + \xi_c(\mathbf{r}, t) \quad (4-8)$$

where ∇ is the gradient operator; L and M are kinetic coefficients describing the rate of the displacive transformation and the isotropic mobility of carbon in the diffusion process, respectively; $\frac{\delta E}{\delta \eta_p(\mathbf{r}, t)}$ and $\frac{\delta E}{\delta c(\mathbf{r}, t)}$ are the variational derivatives of the free energy functional which determine the driving forces; and $\xi_{\eta_p}(\mathbf{r}, t)$ and $\xi_c(\mathbf{r}, t)$ are Langevin noise terms for the order parameters and carbon concentration, respectively. These noise terms introduce into the model a possibility of a spontaneous thermal nucleation not restricted by any *a priori* assumptions about the spatial and temporal distribution of nucleation events.

4.2.4 Modelling of carbide nucleation

In order to model the carbide nucleation, we introduced carbides as carbon sinks inside austenite. The nucleation of carbides was controlled by:

1. Minimum carbon concentration (C_{\min}) required to make the carbide nucleation possible.

2. Frequency (N_{attempts}) controlling the number of attempts to nucleate carbide sinks at every time step.
3. Minimum required probability function (P_{min}).
4. Maximum allowed number of sinks (C_{max}).

The nucleation was a stochastic process attempted in randomly chosen cells. If N_{attempts} was larger than one, then for each time step we randomly chose N_{attempts} cells. If N_{attempts} was fewer than one, then a single nucleation attempt was made in a randomly chosen cell per $1/N_{\text{attempts}}$ time steps. The success of the nucleation attempt in each cell was also based on random numbers and depended on the carbon concentration in cell $c(\mathbf{r})$. If $c(\mathbf{r})$ was below C_{min} then the nucleation could not occur. For cells with $c(\mathbf{r}) > C_{\text{min}}$, a minimum required probability function decreasing from 1 to 0 between the concentration values equal to C_{min} and 6.67 wt% (carbon concentration in carbide) was calculated. Then a random number with a uniform distribution between 0.0 and 1.0 was generated and the nucleation was allowed if the number was above the minimum required probability function value. If the number of the nucleated carbides reached C_{max} then no further nucleation attempts were made. When the carbides were nucleated, the cells containing those carbides were set to have a concentration determined by C_1 , which is a value of the carbon concentration in austenite in equilibrium with carbide; we estimated it using an extended ($\gamma+Fe_3C$) - γ boundary of the Fe-C phase diagram.

4.2.5 Model parameters

The coefficients in Eq. (4-5) for $f[c(\mathbf{r}), \eta_p(\mathbf{r})]$ were fitted to reproduce the thermodynamic characteristics of low alloy steels at 260 °C [65] which were based on Thermo-Calc software. The model parameters can be conveniently described using their dimensionless values. The dimensionless energy units are introduced by using the unit energy, Δf_0 , defined as $\Delta f_0 = f(c, 0) - f(c, (\eta_1=1, \eta_2=0, \eta_3=0))$, i.e., as the difference between the energy of austenite and ferrite with the same composition c , equal to the average carbon concentration in alloy \bar{c} , under the stress-free conditions. We can also introduce the characteristic energy ratio, which determines the relative strengths of elastic interactions and the chemical driving force, as:

$$\zeta = \frac{\varepsilon_0^2 G}{2\Delta f_0} \quad (4-9)$$

ε_0 is defined as:

$$\varepsilon_0 = \frac{a_t - c_t}{a_c} \quad (4-10)$$

where a_c is the lattice parameter of austenite, c_t and a_t are lattice parameters produced by the Bain strains with a cubic to tetragonal symmetry corresponding to the FCC to BCC displacive transformation. G in Eq. (4-9) is shear modulus.

The dimensionless form of the coefficients in the free energy density polynomial Eq. (4-5) is obtained by dividing the dimensional coefficients by Δf_0 . The Δf_0 value depends on the average carbon concentration in the alloy \bar{c} , which is used as a uniform concentration in the initial austenitic state of the system. As a result, the coefficients in the dimensionless polynomial representation of $f[c(\mathbf{r}), \eta_p(\mathbf{r})]$ as well as ζ value (and a relative contribution of elastic interactions into the overall energy balance) depend on \bar{c} . Even though the ferrite lattice parameters depend on carbon concentration [90], this effect is small compared to transformation strain.

The simulations were performed for the initial carbon concentration equal to 0.92 wt. %. A high value of \bar{c} was chosen so that the relative contribution of the elastic energy (ζ values) was high and the elastic energy could control the morphology of ferrite; however; the diffusional process included in the model also played an important role in the transformation process. The \bar{c} value used in the simulations corresponded to $\zeta=30$ and the dimensionless polynomial coefficient values: $A_4=0.244$; $A_2=0.536$; $B_2=4.091$; $B_3=34.091$; $B_4=34.091$; $c_d=1.40$; $c_i=1.5$; $c_{\tilde{\alpha}}=0.02$. We used kinetic coefficients $M=1$ and $L=10$. It is worth pointing out that the ratio of the values of mobility coefficients M and kinetic coefficients L , rather than the absolute values M and L , is important if we are interested in the sequence of microstructure changes during the transformation and do not attempt to capture the time scale of the microstructure evolution, as the absolute values of

these coefficients can be adjusted by changing the time scale. We assume that the length of the time step used in the simulations is equal to one dimensionless time unit. The dimensionless form of the gradient coefficients can be defined as $\beta^* = \beta / (l_0^2 \Delta f_0)$, where the length scale l_0 corresponds to the mesh cell size. As a result, the length scale of the model can be changed by choosing different β^* . $\beta_\eta^* = 1$ and $\beta_c^* = 80$ were used in the simulations. The $64 \times 64 \times 64$ computational mesh was used in all simulations.

To simulate the nucleation of carbides, we used $N_{\text{attempt}}=1000$; $C_1=0.6$ wt%; $C_{\text{max}}=1000$ and $C_{\text{min}}=0.97$ wt.%. Additional simulations with $N_{\text{attempt}} = 1$, $N_{\text{attempt}} = 0.5$ and $N_{\text{attempt}} = 0.3$ were performed. The formation of carbides acting as sinks for carbon resulted in a gradual decrease in the carbon concentration in the solid solution. The simulations were continued until the average carbon concentration in the solid solution reached 0.6 wt.%.

4.3 Results

Fig. 4-1 shows the effect of the number of carbide sinks formed in the retained austenite (solid lines) on the evolution of the ferrite volume fraction (dotted lines) and the average carbon concentration in the solid solution (dashed lines). Different carbide nucleation sequences were obtained using the nucleation models with different N_{attempt} described in section 2.4. These nucleation sequences produced four different transformations - carbide formation scenarios. In all the cases, at the beginning of the transformation the transition from a fast growth process controlled by the displacive mechanism and producing the transformation rate of 6.0 (determined using dimensionless

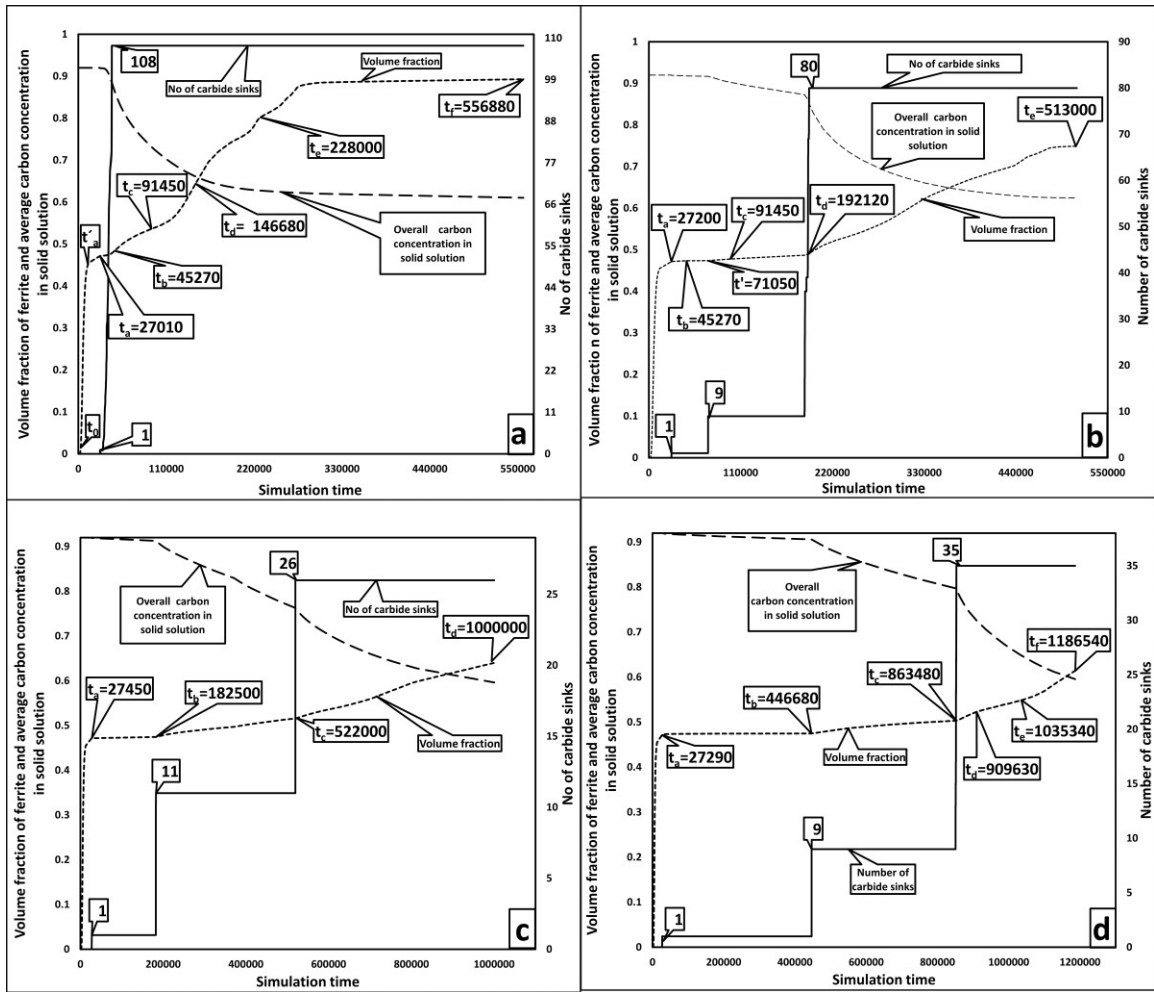


Figure 4-1 The effects of different sinks distributions of the nucleation events with time on the ferrite volume fraction rate and the overall average carbon concentration rate. The solid lines represent the number of carbide sinks introduced at different times; the dotted lines show the evolution of the ferrite volume fraction rate and the dashed lines show the average carbon concentration rate. The initial average carbon concentration in the system is 0.92 wt.% and the final average carbon concentration in the system is 0.6 wt.%, which is the carbon content of carbide in equilibrium with austenite.

time units) at t_0 to a slow growth process, limited by the diffusion, with the transformation rate decreasing to 0.623 at t_a' (as shown in Fig. 4-1 a), after which the kinetics of the transformation process was significantly different in the systems with different nucleation sequences.

In the first nucleation sequence (scenario 1, Fig. 4-1 a), the first carbide nucleation event (producing only one carbide sink) occurred at approximately t_a (a few time steps before t_a). This minor nucleation event did not produce any significant impact on the transformation rate which continued to slow down reaching the value of 0.138 at t_a . The first carbide nucleation event in this scenario was almost immediately followed by a massive carbide nucleation event (at approximately t_b) caused by the high value of N_{attempt} equal to 1000 and producing the number of carbides sinks equal to 108. After this nucleation event a rapid reduction in the average carbon concentration in the solid solution started, and the transformation from austenite to ferrite reaccelerated sharply, after which further transformation proceeded with several stages of slowing down and reaccelerating (although no further carbide nucleation events occurred for the rest of the transformation in this nucleation sequence). Such multiple changes in the transformation rate at intermediate transformation times before reaching completion were observed experimentally in [67, 81]. The transformation eventually approached termination with a zero-transformation rate at t_f when the overall average carbon concentration in solid solution reached 0.6 wt%. The final fraction of ferrite was nearly 90%, and the majority of the microstructure consisted of ferrite with some untransformed austenite as illustrated in Fig. 4-2.

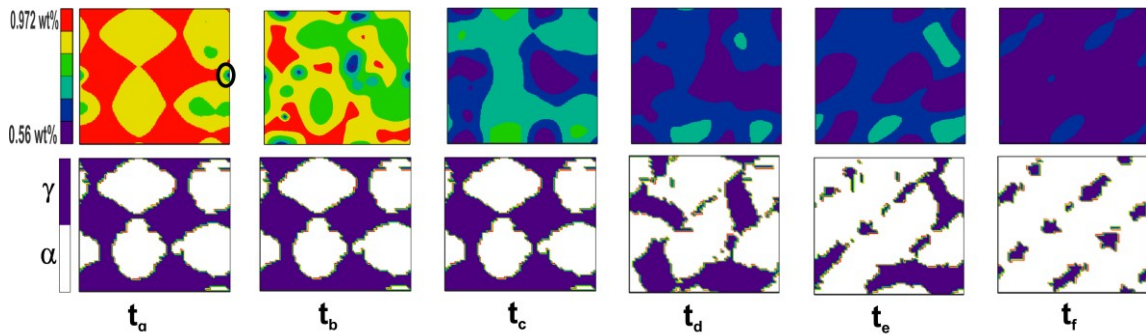


Figure 4-2 Distributions of the carbon concentrations sequences (upper) and respective structures (lower) at different moments of time outlined in Fig. 4-1 a. All transformation variants of ferrite are shown with the same colour.

Fig. 4-2 illustrates the distributions of the carbon concentration (upper) and respective microstructure sequences (lower) at different moments of time shown as t_a , t_b , t_c , t_d , t_e , and t_f on the transformation curve in Fig. 4-1 a, obtained when the carbide nucleation events followed scenario 1. The point marked by a circle on the carbon concentration map as corresponding to time t_a represents the location of the first carbide nucleated a few time steps before the time. This nucleation event occurred when the maximum concentration of carbon in the austenite grain close to the ferrite grain reached C_{\min} as shown in Fig. 4-3. We can see that the nucleation of the first carbide does not result in any observable growth of ferrite grains and the transformation rate still continues to decrease (from 0.623 at t_a' to 0.138 at t_a) as can be seen in Fig. 4-1 a. Fig. 4-2 demonstrates that between t_b and t_c a significant drop in the carbon concentration occurs, and the transformation rate as shown in Fig. 4-1 a accelerates to 0.164 at t_b . However, after that the transformation rate goes through several slowdown - acceleration transitions, for example, slowing down to 0.08 at t_c and then accelerating to 0.337 at t_d . A

significant increase in the volume fraction of ferrite can be observed in Fig. 4-1 a and Fig. 4-2 at the time moments from t_d to t_f ; the ferrite morphology also changes from a rod-like at t_c to a plate-like at t_f . It is interesting to note that ferrite grains and residual austenite form a regular pattern with two well defined orientations of the austenite - ferrite interfaces at $t=t_d$, when the system still has a significant fraction of retained austenite ($f_\gamma=0.355$). Such an arrangement of phases evidences a strong role played by the elastic interactions at this stage of the transformation.

Fig. 4-3 shows the effect of the first carbide nucleation event outlined in scenario 1 on the evolution of the carbon concentration (coloured solid lines) and the structural boundary (coloured dashed lines) along the vertical dashed line shown at the top right insert representing the carbon distribution map with a marked point which represents the first carbide sink outlined in Fig. 4-2. The black solid line in Fig. 4-3 represents the initial carbon content of the system and the coloured solid and dashed lines present the composition distributions and order parameter profiles at time moments outlined in Fig. 4-1 a and Fig. 4-2. The pink colour solid line shows the composition distribution corresponding to the ferrite grain configuration at several time steps before the nucleation of the first carbide when the ferrite boundaries are at the locations shown by pink dashed lines. The carbon concentration in this case still goes up in austenite and goes down in ferrite due to the uphill diffusion. A higher carbon concentration is reached in austenite at some distance from the structural boundary due to a more diffuse nature of the composition boundary as compared to the structural boundary because the composition gradient coefficient is larger than the structural gradient coefficient. After the first carbide

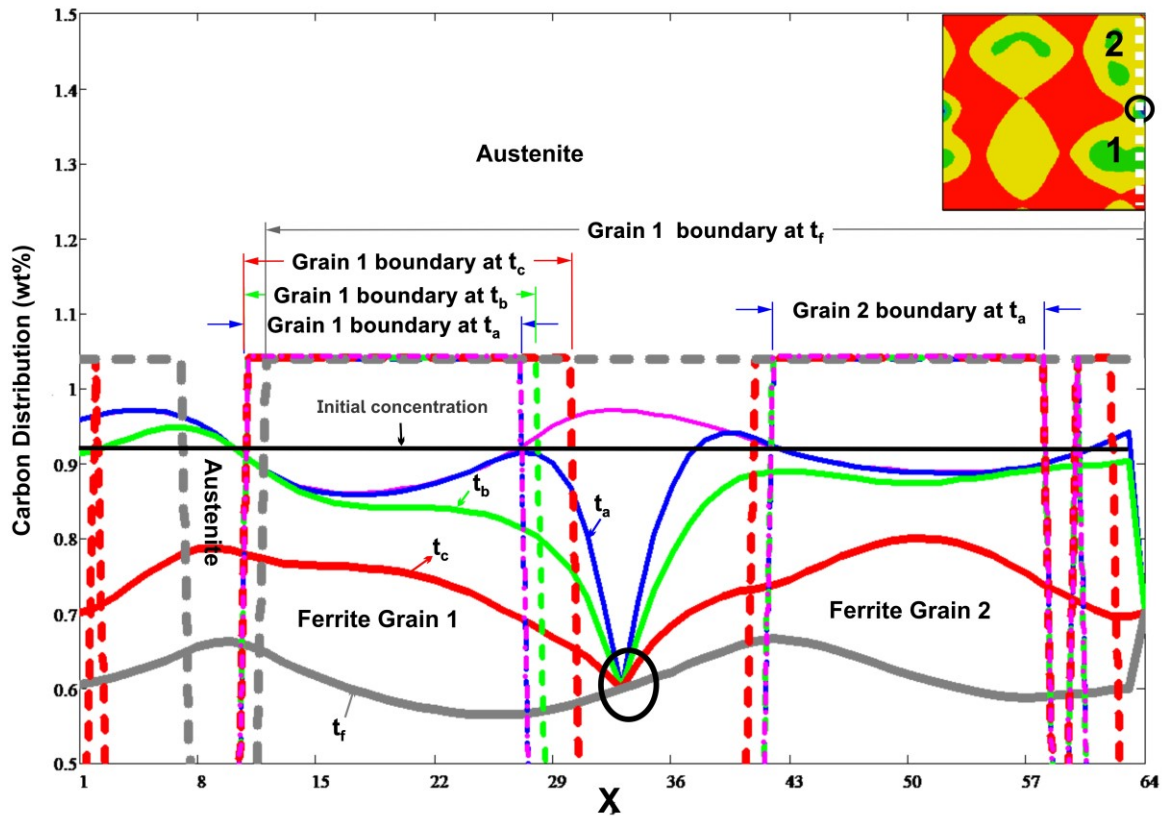


Figure 4-3. One dimensional distributions of the carbon concentration along the dotted white line (from bottom to top) shown in the insert with a two-dimensional concentration map at $t=t_a$ where the encircled point is the location of the first carbide sink. The graph shows carbon concentrations at different moments of time with the coloured solid lines, whereas the coloured dashed lines represent the different positions of the structural boundaries at different moments of time, and the encircled point indicates the location of the first carbide sink. All time markings indicated on these curves are consistent with time moments indicated by the same letters in Fig. 4-1 a.

nucleation event has occurred, a few time steps before t_a , at the location with the highest carbon concentration, any further growth in the direction aligned with the line, along which the concentration profiles are presented in Fig. 4-3, is associated with the carbide nucleation. Due to a slow depletion of carbon, the structural boundary location reflecting the extent of the structural transformation is still the same at time t_a as before the nucleation. Therefore, the effect of the first nucleated carbide on the carbon concentration does not affect the transformation development immediately, and it takes time to produce an impact on the transformation kinetics, as shown in Fig. 4-2 and 4-3.

As the diffusion of carbon towards the sink proceeds, the depletion region around the sink becomes wider and more pronounced as shown in Fig. 4-2 for time moment t_b . The growth of ferrite grain 1 restarting at the same time is illustrated in Fig. 4-3 showing the change of the ferrite-austenite interface position between t_a and t_b . However, on the other side of the austenite grain, the structural boundary of ferrite grain 2 remains unaffected. This can be explained by a shorter distance from the carbide location to the interface with grain 1 and a lower carbon concentration at this interface. As the transformation proceeds, the structural boundary of ferrite grain 2 (Fig. 4-3 at t_c) also begins to move as the carbon concentration at the interface between austenite and ferrite grain 2 gets well below the initial carbon concentration, and further growth of ferrite grain 1 is continued. The shape of ferrite grains then gradually begins to elongate in the direction favoured by the minimum of the elastic energy as shown in Fig. 4-2 at t_d and t_e . Eventually at t_f , in Fig. 4-3, the carbide sink becomes surrounded by ferrite, and the

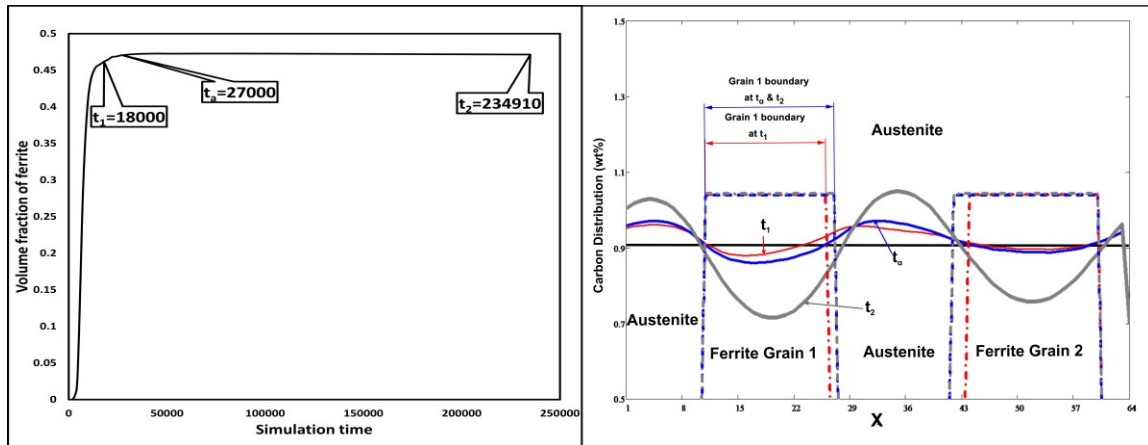


Figure 4-4 (a) Dependence of the ferrite volume fraction on time obtained in the systems without the formation of carbide. (b) Two-dimensional gradient of carbon concentrations through the coloured solid lines and the coloured dashed lines represents different positions of the boundary interface at three different moments of time along the same line as in Fig. 4-3.

carbon concentration gradient flattens out. The transformation reaches completion with rod-like shapes completely changed to plate-like shapes as shown in Fig. 4-2 at t_f .

Along the same line as in Fig. 4-3, Fig. 4-4 shows the evolution of the transformation (Fig. 4-4 a) and the concentration distributions at three different moments of time (Fig. 4-4 b) with no carbide nucleation allowed. After the transformation rate decreases at t_a to 0.138 some movement of ferrite-austenite interfaces and the growth of ferrite grains takes place as can be seen from the comparison of the interfaces shown by dashed lines in Fig. 4-4 b for t_a and t_2 . At t_2 a state of the full stasis is reached, and no movement of the interfaces is produced between t_2 and t_3 . However, during that period, the partitioning of carbon continues as can be seen from the concentration curves shown

in Fig. 4-4 b, and most of the carbon exchange between ferrite and austenite is produced after the structural transformation stopped.

Fig. 4-1 b shows the effect of three separate carbide nucleation events on the overall average concentration in the solid solution and the evolution of the volume fraction of ferrite at N_{attempt} equal to 1 (scenario 2). After the first carbide nucleation event occurred at time (t_a), the second carbide nucleation event (the number of sinks equal to 9) occurred at time (t') with a longer delay between the first and second nucleation events than in scenario 1. This minor carbide nucleation event contributed to a very slight increase in the transformation rate from 0.0023 at t' to 0.014 at t_c (the volume fraction of ferrite grew from 0.472 to 0.487 between t_a and t_c). The decrease in the average concentration in the solid solution was slow (from 0.918wt% at t_b to 0.905 wt% at t_c). As a result, the transformation curve developed a distinct stage of the transformation stasis. After a prolonged transformation stasis, the third carbide nucleation event (the number of carbide sinks equal to 80) at time t_d resumed the transformation producing the transformation rate of 0.104 at t_d and approached the termination of the transformation at time t_e , which was longer than a time t_f in scenario 1. It was observed that the amount of untransformed austenite in scenario 2 (0.250) (the microstructure shown in Fig. 4-5 (a)) is larger than that in scenario 1 (0.107) (the microstructure shown in Fig. 4-2 at t_f), although both scenarios reached a steady state with a zero transformation rate. This significant difference in retained austenite can be explained by the following: (1) the second carbide nucleation event in scenario 2 had only a slight effect on the slow growth mode; (2) all carbide nucleation events in scenario 2 provided a number of carbide sinks that was not sufficient to release all ferrite grains from the

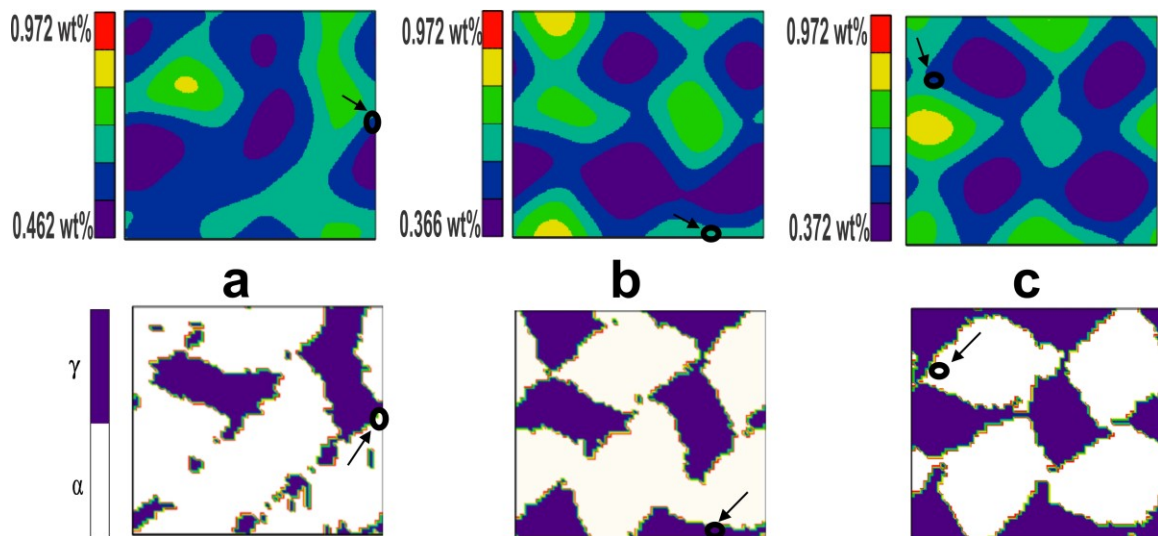


Figure 4-5 Morphologies of the final distributions of the carbon concentrations (upper) and respective structure (lower) at different moments of time outlined in (a) scenario 2, (b) scenario 3, and (c) scenario 4. The marked points that are pointed out by arrows show the first carbide sink formed at time t_a .

growth stasis before the overall average concentration in the solid solution reached 0.6 wt% and the simulation was terminated.

Fig. 4-6 shows the concentration distributions and the locations of the structural boundaries in the systems with the nucleation sequences corresponding to scenario 1 and scenario 2. Initially, at $t=t_a$ and $t=t_b$ there is no difference between the evolution of these systems. However, a significant difference appears at $t=t_c$. The system with the first nucleation sequence has a large number of carbides nucleated at that time, and the

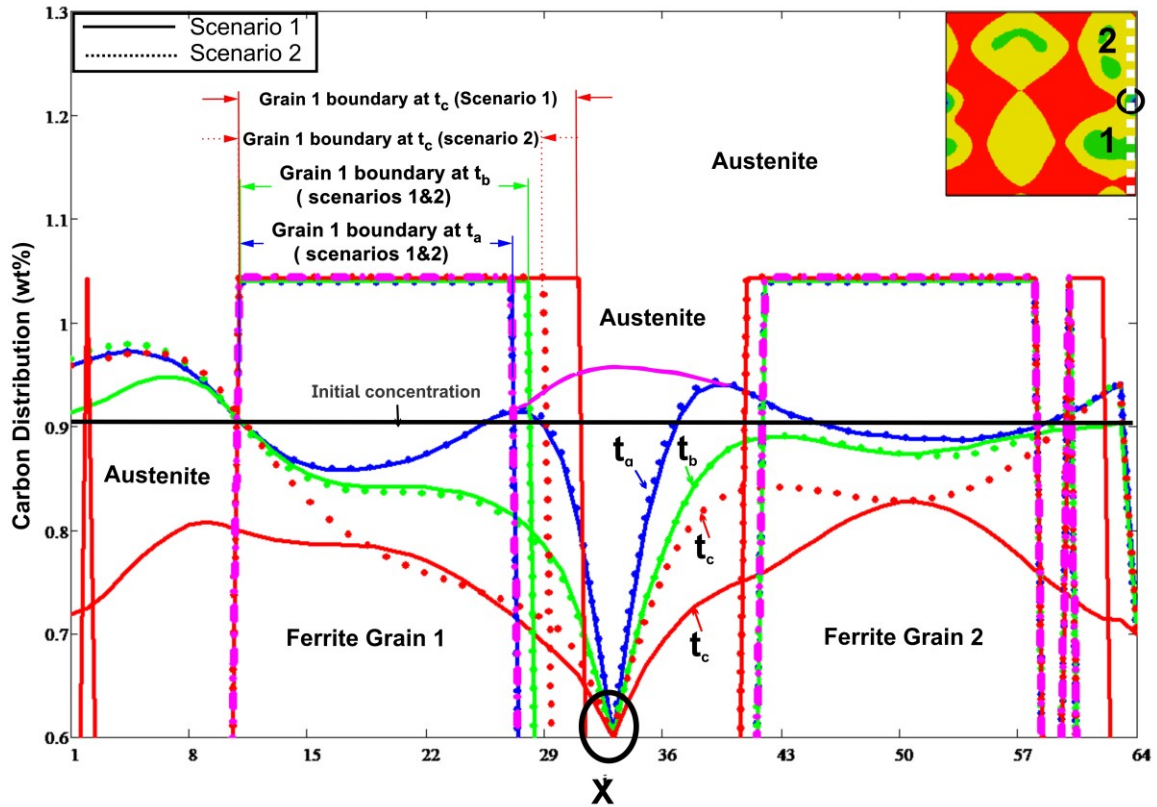


Figure 4-6. One dimensional distributions of the carbon concentration along the dotted white line (from bottom to top) shown in the insert with a two-dimensional concentration map at $t=t_a$, where the encircled point is the location of the first carbide sink. The graph shows the carbon concentrations and different positions of the structural boundaries with coloured solid lines at moments of time t_a , t_b and t_c outlined in Fig. 4-1a (scenario 1), while the coloured dotted lines represent the carbon concentrations and different positions of the structural boundaries at moments of time t_a , t_b and t_c outlined in Fig. 4-1b (scenario 2). All time markings indicated on these curves are consistent with time moments indicated by the same letters in Fig. 4-1 a and b, respectively.

evolution of the composition and grain configuration are controlled not only by the local sinks but also by the overall carbon depletion, which results in a significant acceleration of the ferrite growth. The system with a second nucleation sequence has only a few carbon sinks, and the local evolution is still controlled by the local carbides. As a result, such a system has a substantially higher carbon concentration and a lower transformation rate.

In Fig. 4-1 c and d, the transformation stasis can be observed in scenarios 3 and 4 at t_b . The N_{attempt} in scenario 3 equals 0.5, which makes the stasis period longer than in scenario 2 at t_b , while the longest stasis period occurs in scenario 4 at t_b with N_{attempt} equal 0.3 and the longest delay between the first and second nucleation events. In both scenarios (3 and 4), the restarted transformation rate is considerably slower at t_c (0.025 in scenario 3 and 0.037 in scenario 4) than in scenario 2 (0.104 at t_d) with a corresponding slow reduction in the average concentration of carbon in the solid solution (0.758 in scenario 3 and 0.777 in scenario 4). It can be observed that in Fig. 4-5. b the carbide sink in the final microstructure was not surrounded by ferrite; however, in the system the ferrite growth was still continuing at the end of the simulation. Almost 36% of the untransformed austenite remained in scenario 3 and 40% in scenario 4 in the final state reached at the end of the simulation. These high fractions of retained austenite are due to prolonged stasis periods, and in both cases the transformation had a non-zero rate when the overall average concentration of carbon in the solid solution reached 0.6 wt% and was terminated. The microstructure obtained using the nucleation scenario 3 (Fig. 4-5 b) had a regular pattern produced by the austenite and ferrite grains with the same morphology as the one observed in Fig. 4-2 at time t_d and obtained in the system with the

first nucleation scenario and characterized by a high transformation rate (0.337) at that point in time. It is necessary to note that the transformation kinetics after the end of all the nucleation events can exhibit several acceleration - slowdown transitions, especially clearly seen in the case of nucleation scenario 1, but also observed in nucleation scenarios 2 and 4.

4.4 Discussion

The simulation results demonstrate that a) the reacceleration of the bainitic transformation after the diffusion-controlled growth stage or full stasis is associated with the beginning of the carbide precipitation in austenite and b) the final stage of the transformation may play a role in determining the final morphology type of the produced microstructure. Such a role of the carbide precipitation in the development of the bainitic transformation was already suggested in [25, 67, 76, 79-81, 86] and experimentally demonstrated in [28, 39, 66, 69, 79, 83]. Our results clearly demonstrate that the overall bainitic transformation has three stages in all the nucleation scenarios shown in Fig. 4-1. The first stage takes place with a rapid kinetics controlled by the displacive transformation (as was shown in [65]), which leads to the start of the decomposition at the interface between austenite and ferrite and the build up of carbon in austenite (Fig. 4-4). However, the incubation period during which no transformation is detected was very short due to artificially high noise amplitude was used. At the beginning of the second stage, the transformation rate is slowed down and carbon concentration in the enriched layer approaches the equilibrium value, and the diffusion process takes over the control

of the transformation kinetics. The ferrite gains acquire a rod-like shape (Fig. 4-2) favored by the diffusion limited growth conditions. A full transformation stasis develops in all the systems with a small number of carbides when the fraction of ferrite is close to 0.472 (similar conditions were observed experimentally in [28, 39] in the range between 0.4 and 0.6). However, the fraction of product phase at the onset of stasis can be determined by role of carbon concentration where the driving force at given temperature and lower average concentration may lead to larger fraction of ferrite. In the system with massive nucleation occurring early in the transformation history only a reduction of the transformation rate is produced. In all cases during a slow transformation or during a complete stasis the carbon partitioning continues to lead to an increasing carbon concentration in austenite. When the concentration reaches the critical value C_{\min} , the formation of carbides becomes possible. In scenario 2, the long stasis stage leads to the increase in the fraction volume of ferrite from 0.472 to 0.487 after a minor nucleation event (>8 sinks). The effect of the enriched layer slows down the growth rate and the overall transformation rate remains unchanged. The transformation reaccelerates significantly by additional carbide sinks (> 25 sinks), thus eliminating the effect of the saturation layer. However, when the overall average concentration reaches 0.6 wt%, the final ferrite fraction is 0.749 which is smaller than 0.892 in scenario 1.

The third stage starts when a sufficient number of carbides is nucleated and the reduction of the carbon concentration in austenite makes a structural transformation possible again. Such a reacceleration of the transformation after the stasis period has been observed in [28, 39, 83]. The onset of the third stage, and the extent of the transformation reacceleration depends on the rate of the carbide nucleation. In scenario 1, a massive

nucleation of additional carbide sinks at t_b quickly reduces the carbon concentration in austenite around ferrite grains, and the transformation rate exhibits three peaks before completion. Similar changes in the transformation rate were observed experimentally in [67, 81]. The overall transformation rate during the third stage is controlled by the diffusion process; however, in this case, it is a diffusion from austenite to carbide carbon sinks. The carbides nucleated inside austenite close to interface with ferrite can eventually become surrounded by ferrite grains (Fig. 4-2); this mechanism is similar to the diffusion-controlled ledge-wise growth mechanism suggested in [25, 74, 82] .

While the volume fractions of phases remain unchanged during the stasis period, the carbon partitioning still takes place enhancing the carbon enriched layer around the ferrite grains and creating more favorable conditions for the carbide nucleation. It is possible that most of the carbon partitioning is produced after the termination of the ferrite grain growth, and the partitioning and carbide formation may be secondary processes following the structural transformation as suggested in [26, 76, 78-80]. However, the role of the carbide nucleation can still be important for the overall development of the transformation. The effect of a long stasis stage caused by a small number of carbide sinks nucleated in the system can also prevent the overall transformation reaching a stable state although the overall average concentration in the solid solution has reached 0.6 wt%. In scenarios 3 and 4, the stasis stage is longer than in scenario 2, and the effect of the diffusion-controlled growth is extended to prevent the overall transformation to a stable state. In addition, a larger fraction of untransformed austenite at the end of the simulation in scenarios 3 and 4 demonstrates that the effect of

the diffusion-control over the ferrite growth is stronger when the density of carbide sinks is low.

During the third stage, the carbide nucleation and carbon diffusion from austenite to carbides control the transformation kinetics and can also result in large changes in the final shapes of the ferrite grains; however, transformation strains and the elastic energy can still be important [65] in that they can continue to dictate the evolution of the morphology as can be seen in (Fig. 4-2). The transition from the shape shown in Fig. 4-2 at t_a to the shape shown Fig. 4-2 at t_f occurs after the carbide precipitation when the transformation curve has a steeper slope indicating a decrease in the degree of the diffusion control over the transformation. The shape of the ferrite grains changes over this period of time from a rod-like to plate-like because the plate-like shape corresponds to the minimum of the elastic energy. The microstructures obtained in different systems after a significant carbon depletion, but still having a significant fraction of austenite (Fig. 4-2 d, Fig. 4-5 b and c) demonstrate a well-organized pattern of the parent and product phases. In all the cases, austenite and ferrite are arranged into two-phase plates consisting of austenite and ferrite rods with the same orientation of the austenite-ferrite interfaces and plate habit planes in all the structures. Such a well reproducible morphology evidences the dominant role of elastic interactions in the morphology control at the corresponding stages of the transformation.

4.5 Conclusions

The bainitic type transformation was studied using the phase field method to investigate the effect of a carbide nucleation event on the overall kinetics of the transformation and the ferrite growth mechanism. The results and conclusions are summarized as follows:

1. The transition from a fast growth process to a slow growth with the diffusion control leads to the development of carbon enriched layers around the ferrite grains, which can result in a complete transformation stasis. During the stasis, the partitioning of carbon between ferrite and austenite continues, leading to the increase in the carbon concentration in austenite.
2. The increase in the carbon concentration in austenite in the locations with the highest carbon concentration leads to the nucleation of carbides close to ferrite grains.
3. Carbides, acting as sinks for carbon, reduce the carbon concentration in ferrite, thus creating a condition for the reacceleration of the austenite to ferrite transformation.
4. The length of the stasis period and the rate of the reaccelerated transformation are strongly sensitive to the density of carbides produced in austenite.

5. A significant reduction of the overall carbon concentration in the solid solution as a result of the carbide formation may shift control over the morphology of ferrite grains towards elastic interactions from the kinetic control of the diffusion process.

Chapter 5: The influence of carbide formation in ferrite on the bainitic type transformation.

Abstract

The effect of carbide formation on the development of the bainitic type transformation was studied using phase field modeling. The phase field model incorporated the displacive structural transformation producing a misfitting product phase, long range elastic interactions, carbon partitioning from austenite and ferrite and the formation of carbides in ferrite modelled as carbon sinks. The results of the simulations performed for the systems with different carbide nucleation sequences demonstrate that initially, due to a slow nucleation of carbides and fast carbon partitioning, carbon diffusion to austenite was the dominant process leading to the decrease in the transformation rate. However, after some period of time, the effect of carbon depletion in the solid solution by carbides became more significant, which led to the reduction of the average concentration of carbon in the whole system and the acceleration of the structural transformation. The rate of carbide nucleation and the number of nucleated carbides controlled both the transformation rate and the period of time before the transformation acceleration.

5.1 Introduction

For years, it has been discussed if the development of the bainitic transformation is controlled a) by diffusion [9, 63], b) by displacive mechanism [3, 11, 20, 44, 64], or c) equally by both processes [65]; however, the issue has not yet been resolved. For example, the role of carbide formation in ferrite during the bainitic transformation is not clear. Multiple experimental observations have revealed that carbides form and grow within supersaturated bainitic ferrite and may play an important role in the transformation kinetics [10, 20, 23, 24, 26, 27, 67, 72, 77, 81, 91-102]. It was suggested in [26] that carbide precipitation within supersaturated bainitic ferrite can be considered a diffusional process, which results in some reduction of the strain energy. The data relevant to the question of the role of carbide in the bainitic transformation can be found in the studies of the quenching and partitioning treatment in which steel is first quenched to martensite and then annealed at the bainitic transformation temperatures. It was demonstrated in [77] that during the quenching and partitioning treatment of the 0.3C-1.6Si- 3.5Mn (wt.%) steel, the formation of carbides at the initial stage of quenching, applied before the partitioning annealing, might play an important role in the kinetics of carbon partitioning. In particular, the combination of a slow process of the decomposition of unstable carbides, formed during the initial quenching and a fast carbon partitioning from ferrite to residual austenite, slowly reduces the carbon content in ferrite and requires a long time for the completion of carbon depletion in the ferrite grains [77]. Similar results were demonstrated in [67] wherein it was also suggested that the dissolution of

transitional releasing carbon in ferrite and the partitioning of released carbon into austenite may lead to the stabilisation of residual austenite and a temporary increase in its fraction during the partitioning treatment. A rather different role of carbides in the partitioning process was discussed in [72] on the basis of an experimental observation of the carbon concentration distribution during partitioning treatment of the 0.59%C–2%Si–2%Mn steel. In this case, the formation of carbides inside ferrite occurred simultaneously with the partitioning process and, thus, competed with it in carbon consumption. The presence of these carbides was shown to significantly affect the carbon concentration in austenite at the end of the partitioning treatment.

Mössbauer effect spectroscopy (MES) was used in [97] to quantify carbide formation in the 0.38C–1.54Mn–1.48Si wt.% steel after two different heat treatment processes; that is, quenching & partitioning (Q&P) with salt quenching to 225 °C and partitioning at 400 °C, and quenching & tempering (Q&T) with water quenching to room temperature and partitioning at 400 °C. The study illustrated the importance of the competition between carbide formation and carbon partitioning. The Q&P treatment produced a slightly smaller fraction of martensite after quenching compared to the Q&T treatment; martensite after the Q&P treatment contained a lower density of defects, which could provide the nucleation sites for carbides. As a result, the partitioning and tempering processes produced different microstructures even though the same annealing conditions were used. The Q&T process produced a higher volume fraction of carbides, which consumed more carbon, thus resulting in a zero fraction of residual austenite. The Q&P process produced approximately two-time less carbides which consumed less carbon, and, therefore, more carbon was partitioned to austenite, resulting in a non-zero fraction

of residual austenite at the end of treatment. Thus, the formation of carbides resulted in a faster formation of a more equilibrium structure.

In the case of the bainitic transformation, carbide formation within supersaturated ferrite can occur during the displacive transformation [23], and the effects of carbide formation on the bainite kinetic are different from the case wherein carbide forms in austenite [24]. It was proposed in [92] that due to the inhomogeneity of the carbon concentration within bainitic ferrite, carbides are formed in high carbon concentration regions. As a result, the combination of a slow rate of carbide nucleation and a fast rate of carbon partitioning at the interface between austenite and ferrite leads to the formation of depleted regions and carbide free zones in ferrite near the interfaces with austenite. Dislocations can attract carbon in ferrite and determine where carbides can be formed [27]; thus, dislocations can control the number of carbides that can be produced. Carbide formation can play an important role in the completion of the transformation after the stasis period [28, 39, 83]. Stasis is reached when the partitioning of carbon to austenite and the increase in the elastic energy make further transformation impossible. The formation of carbides reduces the carbon concentration in solid solutions and reaccelerates the transformation. However, stasis can be produced even during the time period when carbide formation in bainitic ferrite has already started [83].

There have been only a few modelling studies that focused on carbon partitioning from ferrite into austenite, accompanied by carbide precipitation in ferrite, and the impact of carbide precipitation on overall transformations kinetics and morphology [8, 72, 95, 103]. For example, in [8], a phase field model was used to study a possible role of carbide formation in the development of the bainitic transformation with carbon partitioning from

ferrite to austenite and the diffusion controlled kinetics. However, the effect of the strain or stress interaction was not considered. A thermodynamic model describing carbon partitioning between ferrite and austenite (a constrained carbon equilibrium model) was developed in [103] and later modified in [72] to include carbide formation in ferrite. The model was designed to predict the carbon concentration in austenite after the partitioning step. Because the model neglected the effect of the carbide formation kinetics, an accurate prediction of austenite carbon concentrations during the partitioning steps was not obtained. It is clear that that a model that accounts for the displacive transformation, carbide nucleation and carbon partitioning processes can provide a fundamental understanding of how the interactions between these processes affect the transformation kinetics and the morphology of the bainitic transformation. Thus, in this study we offer a model, which incorporates the displacive transformation accompanied by the carbide formation and carbon partitioning processes by using the methodology presented in [65] to investigate the effect of carbide nucleation in ferrite on the bainitic transformation kinetics and morphology of the produced microstructure.

5.2 Phase field modelling

A phase field model is used in this study to investigate the case of carbide formation in supersaturated ferrite during the bainitic transformation. The displacive transformation and carbon partitioning from ferrite to austenite are incorporated in the model to occur simultaneously with carbide formation without any explicit conditions imposed on the sequences of the processes.

5.2.1 Order parameters and transformation strains

The microstructure formed by austenite and ferrite is described using the distributions of three order parameters, $\eta_1(\mathbf{r})$, $\eta_2(\mathbf{r})$, $\eta_3(\mathbf{r})$, and, additionally, the distribution of the carbon concentration $c(\mathbf{r})$ describes the composition of the solid solutions. For example, the phase state is defined as austenite at any location r when all η_1 , η_2 , η_3 values are close to zero, while the phase state is defined as ferrite at points r when one of the η_1 , η_2 , η_3 has a value close to one and other values of the order parameters are close to zero. Also, the values of the order parameters determine the transformation induced stress-free strain field (ε_{ij}^0):

$$\varepsilon_{ij}^0 = \sum_{n=1}^3 \eta_n \cdot \varepsilon_{ij}^{00}(n) \quad (5-1)$$

where $\varepsilon_{ij}^{00}(n)$ describes the stress - free transformation strain corresponding to the displacive transformation of the parent phase into the orientation variant n of the ferrite phase. In the case of the austenite to ferrite transformation, there are three different transformation strains (Bain distortions having the cubic to tetragonal symmetry of the transformation strain) corresponding to three different transformation variants of ferrite:

$$\varepsilon_{ij}^{00}(1) = \begin{bmatrix} 0.137 & 0 & 0 \\ 0 & 0.137 & 0 \\ 0 & 0 & -0.196 \end{bmatrix} \quad \varepsilon_{ij}^{00}(2) = \begin{bmatrix} 0.137 & 0 & 0 \\ 0 & -0.196 & 0 \\ 0 & 0 & 0.137 \end{bmatrix} \quad \varepsilon_{ij}^{00}(3) = \begin{bmatrix} -0.196 & 0 & 0 \\ 0 & 0.137 & 0 \\ 0 & 0 & 0.137 \end{bmatrix} \quad (5-2)$$

Instead of using the combination of the transformation strains and rotations producing up to 24 orientation relations [88], we use the phase field model based on the micromechanics theory that requires only the transformation strains as the input parameters and accomplishes the lattice continuity by automatically adding the necessary rotations during the simulation [16, 18, 48].

5.2.2 Chemical free energy functional

The total chemical free energy of the microstructure E^{Chem} is defined as the functional:

$$E^{Chem} = \int_V f[c(\mathbf{r}), \eta_p(\mathbf{r})] + \frac{1}{2} \beta_\eta \cdot [\nabla \eta_p(\mathbf{r})]^2 + \frac{1}{2} \beta_c \cdot [\nabla c(\mathbf{r})]^2 d^3r \quad (5-3)$$

where $f[c(\mathbf{r}), \eta_p(\mathbf{r})]$ refers to the local chemical free energy density as a function of the composition, c , and the order parameters, η_p with $p=1,2,3$, while the remaining terms are the interfacial energy. β_η and β_c in the remaining terms are, respectively, the gradient coefficient of the order parameter and the gradient coefficient of the composition. We use

the Landau-type polynomial for a generic decomposition-displacive transformation presented in [53] to describe the local chemical free energy density as:

$$f(c, \eta) = \frac{1}{4} A_4 (c - c_d)^2 (c - c_i)^2 + \frac{1}{2} A_2 (c - c_d)^2 - \frac{1}{2} B_2 (c_{\tilde{\alpha}} - c) \cdot (\eta_1^2 + \eta_2^2 + \eta_3^2) - \frac{1}{3} B_3 (\eta_1^3 + \eta_2^3 + \eta_3^3) + \frac{1}{4} B_4 (\eta_1^2 + \eta_2^2 + \eta_3^2)^2 \quad (5-4)$$

where c_i corresponds to austenite composition close to the equilibrium state; $c_{\tilde{\alpha}}$ corresponds to ferrite composition close to the equilibrium state; and c_d is close to the critical composition c_0 , at which both the parent phase and the product phase have the same free energy in a stress free state.

5.2.3 Elastic strain energy

The energy of elastic interactions in the microstructure with coherent misfitting phases having stress-free strains produced by the transformation and described by Eq. (5-1) can be determined under the applied stress conditions as:

$$E^{Elast} = \int_V \frac{1}{2} \cdot C_{ijkl} \cdot [\varepsilon_{ij}(\mathbf{r}) - \varepsilon_{ij}^0(\mathbf{r})] \cdot [\varepsilon_{kl}(\mathbf{r}) - \varepsilon_{kl}^0(\mathbf{r})] d^3r - \int_V \sigma_{ij}^{appl} \varepsilon_{ij}(\mathbf{r}) d^3r \quad (5-5)$$

where C_{ijkl} is the elasticity tensor; $\varepsilon_{ij}(\mathbf{r})$ is the total strain, including the elastic part and stress free strain $\varepsilon_{ij}^0(\mathbf{r})$, and σ_{ij}^{appl} is the applied stress. In this study, we use the

formulation of the microelasticity theory based of the Fourier transform method as presented in [18], which provides the solution for the elastic strains, stresses and the elastic strain energy, and satisfies the continuity and stress equilibrium conditions. This approach was used in phase field models of different transformations (for example, in [18, 47, 54, 65, 89]).

5.2.4 Governing equations for microstructure evolution

The system evolution is determined by the time-dependent Ginzburg-Landau equation for $\eta_p(\mathbf{r},t)$ and the Cahn-Hilliard diffusion equation for $c(\mathbf{r},t)$:

$$\frac{\partial \eta_p(\mathbf{r},t)}{\partial t} = -L \frac{\delta E}{\delta \eta_p(\mathbf{r},t)} + \xi_{\eta_p}(\mathbf{r},t) \quad (5-6)$$

$$\frac{\partial c(\mathbf{r},t)}{\partial t} = M \nabla^2 \frac{\delta E}{\delta c(\mathbf{r},t)} + \xi_c(\mathbf{r},t) \quad (5-7)$$

where ∇ is the gradient operator; L and M are the coefficients describing the kinetics of the order parameter relaxation and the diffusion isotropic mobility of carbon, respectively; E is the total free energy $E = E^{Chem} + E^{Elast}$; $\frac{\delta E}{\delta \eta_p(\mathbf{r},t)}$ and $\frac{\delta E}{\delta c(\mathbf{r},t)}$ are the driving forces for the order parameter and the composition evolution, respectively; $\xi_{\eta_p}(\mathbf{r},t)$ and $\xi_c(\mathbf{r},t)$ are the noise terms for the order parameters and the composition, respectively.

5.2.5 Modelling of carbide nucleation

In order to model carbide nucleation during the bainitic transformation, carbide nucleation was described in the model as the formation of carbon sinks in ferrite. The following parameters were used to control the nucleation of carbides:

1. Minimum carbon concentration (C_{\min}) required to make carbide nucleation possible. This concentration is significantly higher than the equilibrium solubility limit of carbon in ferrite according to the data presented in [92].
2. Frequency (N_{attempts}) controlling the number of attempts to nucleate carbide sinks at every time step.
3. Required probability function (P_{req}).
4. Minimum required probability function (P_{\min}).
5. Maximum allowed number of sinks (C_{\max}). The parameter is determined by the density of the nucleation sites which can be controlled by the density of defects in ferrite [27].

The nucleation was a random process where attempts of nucleation were undertaken in randomly chosen cells in ferrite regions. If $N_{\text{attempts}} > 1$, then for each time step we randomly chose N_{attempts} cells. However, if $N_{\text{attempts}} < 1$, a single nucleation attempt was made in a randomly chosen cell per $1/N_{\text{attempts}}$ time steps. The nucleation attempts had continued until the total number of carbides reached the C_{\max} value. The probability of a successful nucleation attempt depended on the carbon concentration in the cell $c(\mathbf{r})$.

If $c(\mathbf{r}) > C_{\min}$, then the required probability function decreasing from 1 at C_{\min} to 0 at 6.67 wt. % of carbon was used to determine the P_{req} value. A random number with a uniform distribution between 0.0 and 1.0 was generated and the nucleation was allowed if the number was above the P_{req} value. When carbides were nucleated, the cells containing these carbides were set to have a concentration equal to C_1 , which was a value of the carbon concentration in ferrite in equilibrium with carbide. We estimated this value by using the extended ($\alpha+Fe_3C$) - α boundary of the Fe-C phase diagram.

5.2.6 Computational parameters

The thermodynamic data for a typical free energy for a low alloy high carbon steel at 260 °C was obtained using the Thermo-Calc software. The polynomial coefficients in Eq. (5-4) were fitted to reproduce these thermodynamic data as close as possible. We used dimensionless values to define the model parameters. The energy scale (Δf_0) is the difference between the energy of the γ phase and the α phase with the same carbon concentration \bar{c} corresponding to the initial uniform carbon concentration in the austenitic state: $\Delta f_0 = f(\bar{c}, 0) - f(\bar{c}, (\eta_1=1, \eta_2=0, \eta_3=0))$. By using this definition of Δf_0 , the characteristic energy ratio, which determines a relative strength of elastic interactions, can be introduced as:

$$\zeta = \frac{\varepsilon_0^2 G}{2\Delta f_0} \quad (5-8)$$

where G is the shear modulus and ε_0 is defined by:

$$\varepsilon_0 = \frac{a_t - c_t}{a_c} \quad (5-9)$$

where a_c is the lattice parameter of austenite, c_t and a_t are the lattice parameters produced by the cubic to tetragonal transformation Bain strain.

The chemical free energy can be presented in a dimensionless form using reduced coefficients in Eq. (5-5) defined as the dimensional coefficients divided by Δf_0 . The simulations were performed for the initial carbon concentration equal to 0.92 wt %. This \bar{c} value corresponded to $\zeta=30$ and to the dimensionless polynomial coefficient set $A_4=0.244$; $A_2=0.536$; $B_2=4.091$; $B_3=34.091$; $B_4=34.091$; $c_d=1.40$; $c_i=1.5$; $c_{\bar{\alpha}} = 0.02$; $M=1$ and $L=10$. It is worth pointing out that to initialize the process, a preliminary nucleation run with the lower $\zeta = 10$ was introduced for a short period of time (started at the evolution time = 0 and ended at the evolution time = 4000) because a high elastic energy suppressed the nucleation. Then the process switched to $\zeta=30$ and each simulation time shown in the results section equals the evolution time + 4000. We assumed that the length of the time step was equal to one dimensionless time unit. The relationship between the dimensionless time unit and the physical time is determined by the kinetics coefficient while relative rates of the displacive transformation and diffusion were determined by the L/M ratio.

To simulate the nucleation of carbides, we used $N_{\text{attempt}}=0.01$; $C_1=0.025$; $C_{\text{max}}=1000$; $P_{\text{min}}=0.1$ and $C_{\text{min}}=0.9$. Additional simulations with $N_{\text{attempt}} = 1$ were

performed. The dimensionless gradient coefficient β^* was scaled as $\beta^* = \beta / (l_0^2 \Delta f_0)$, where l_0 is the mesh cell size. Thus β^* value controlled the length scale of the model. We used the same values $\beta_\eta^* = 1$ and $\beta_c^* = 80$ as in [53, 65]. The $64 \times 64 \times 64$ computational mesh was used for all simulations.

5.3 Results

5.3.1 Transformation development without carbide nucleation.

Fig. 5-1 shows the evolution of the ferrite fraction at different moments of time. At the first stage up to t_a , the displacive transformation takes place with a high transformation rate (6.00 at t_0 in dimensionless time units). As a result, the volume fraction of ferrite increased rapidly from 0.076 at t_0 to 0.384 at t_a with the carbon content in austenite and ferrite remaining unaffected, as can be seen in Fig. 5-2. Fig. 5-2 shows concentration distributions (solid lines) and structural boundaries (dashed lines) at different moments of time along the dotted arrow line shown in the top left thumbnails representing the carbon distribution map (left thumbnail) and structure (right thumbnail). The coloured solid and dashed lines in Fig. 5-2 present composition distributions and order parameter profiles at the time moments marked in Fig. 5-1.

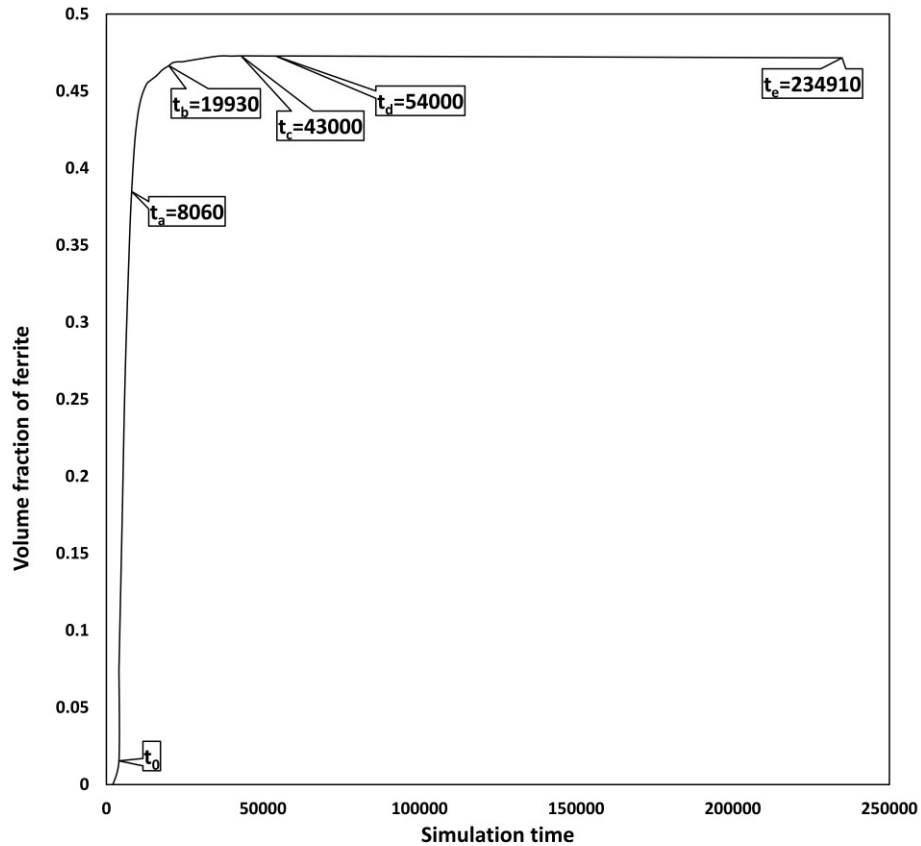


Figure 5-1 The dependence of the ferrite fraction on the time obtained in the system with the initial carbon concentration 0.92 wt.% and no carbide nucleation allowed.

At the beginning of the transformation, the ferrite grain 1 (Fig. 5-2) was formed by the displacive transformation followed by two types of the structural boundary movement occurring between t_a and t_b . One movement corresponded to the shifting of the whole ferrite grain 1 in the left direction, and the other corresponded to a slight increase in the

volume of the grain. Elastic interactions were the main cause of the grain shifting as this movement optimized the structure to reduce the elastic energy. The growth in size was caused by the transformation driving force determined by the chemical energy. The build-up of the elastic energy resulted in the decrease in the transformation rate and allowed the uphill diffusion to produce a noticeable partitioning effect, increasing the

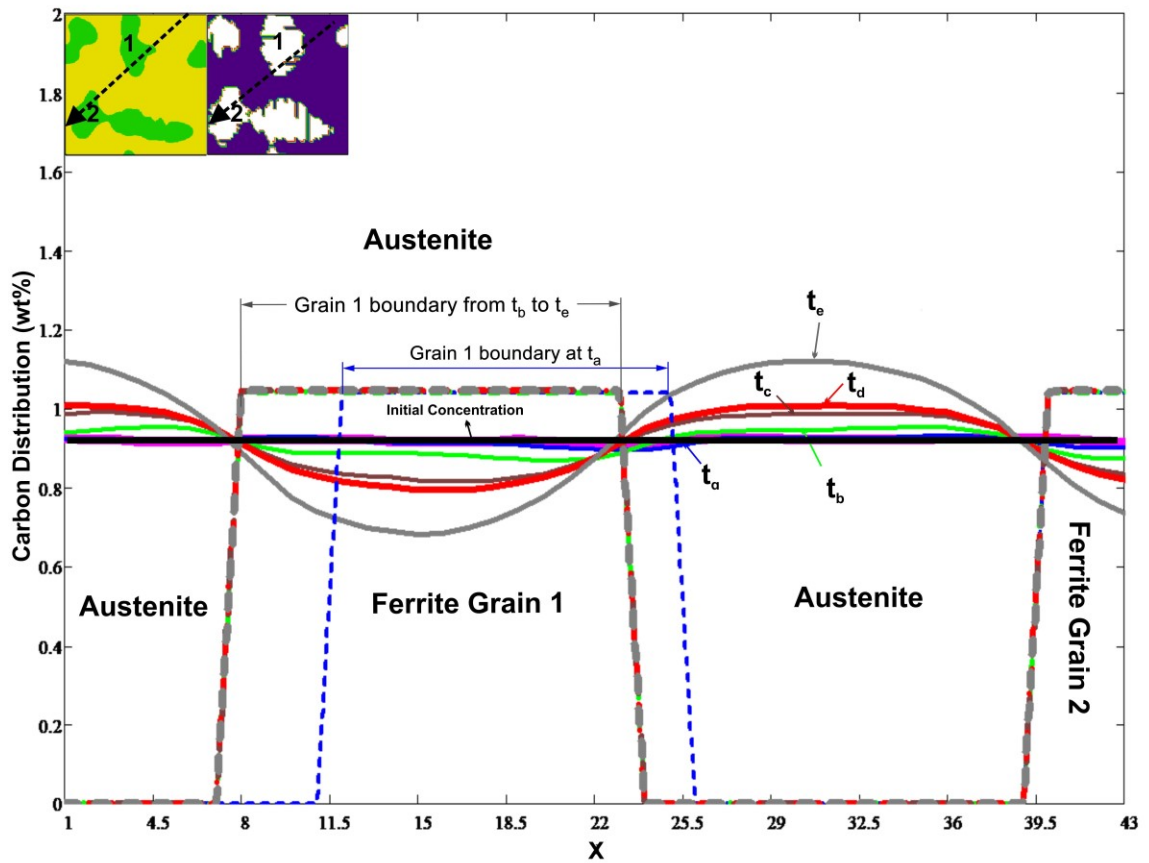


Figure 5-2. Coloured solid lines represent the distribution of carbon concentration; coloured dashed lines represent positions of the interfaces at different moments of time along the dotted arrow shown in the top left thumbnail, representing the carbon distribution map and respective structure at t_a .

carbon concentration in the austenite grain. At the second stage of the transformation, starting between t_a and t_b , the combined effects of the increased elastic energy and elevated carbon concentration in austenite caused a rapid decrease in the transformation rate from 5.742 at t_a to 0.131 at t_b . After t_b , the partitioning effect on carbon distribution became stronger (Fig. 5-2), which further reduced the rate of the structural transformation (Fig. 5-1). The average carbon content in austenite at t_b increased to 0.973 wt.% while the average carbon content in ferrite decreased to 0.859 wt.%. As the transformation proceeded, the volume fraction of ferrite slowly increased, changing from 0.466 at t_b to 0.472 at t_c with the average carbon content in austenite increasing to 0.996 wt.% at t_c . The ferrite grains at t_b had a rod-like shape (Fig. 5-3) which was favoured by the diffusion process.

Fig. 5-3 shows the distributions of the carbon concentration (a) and the corresponding microstructure sequences (b) at different moments of time shown as t_a , t_b , t_c , t_d and t_e , as marked in Fig. 5-1 and Fig. 5-2. During the time period from t_a to t_b , the nuclei of supersaturated ferrite formed by the displacive transformation and the carbon enriched layer begins to form in austenite at the boundary between ferrite and austenite.

The full stasis is reached at t_d when the transformation rate decreases from 0.027 at t_c to zero at t_d and no further growth of ferrite is produced as can be shown by structural boundaries from t_c to t_d in Fig. 5-2. However, the carbon partitioning between ferrite and austenite still occurs in the time period from t_d to t_e as demonstrated by the concentration curves in Fig. 5-2. The carbon concentration continues to increase in austenite during stasis and decrease in ferrite, with the average carbon content in austenite reaching 1.140 wt. % and the average carbon content in ferrite reaching 0.659 wt% at t_e .

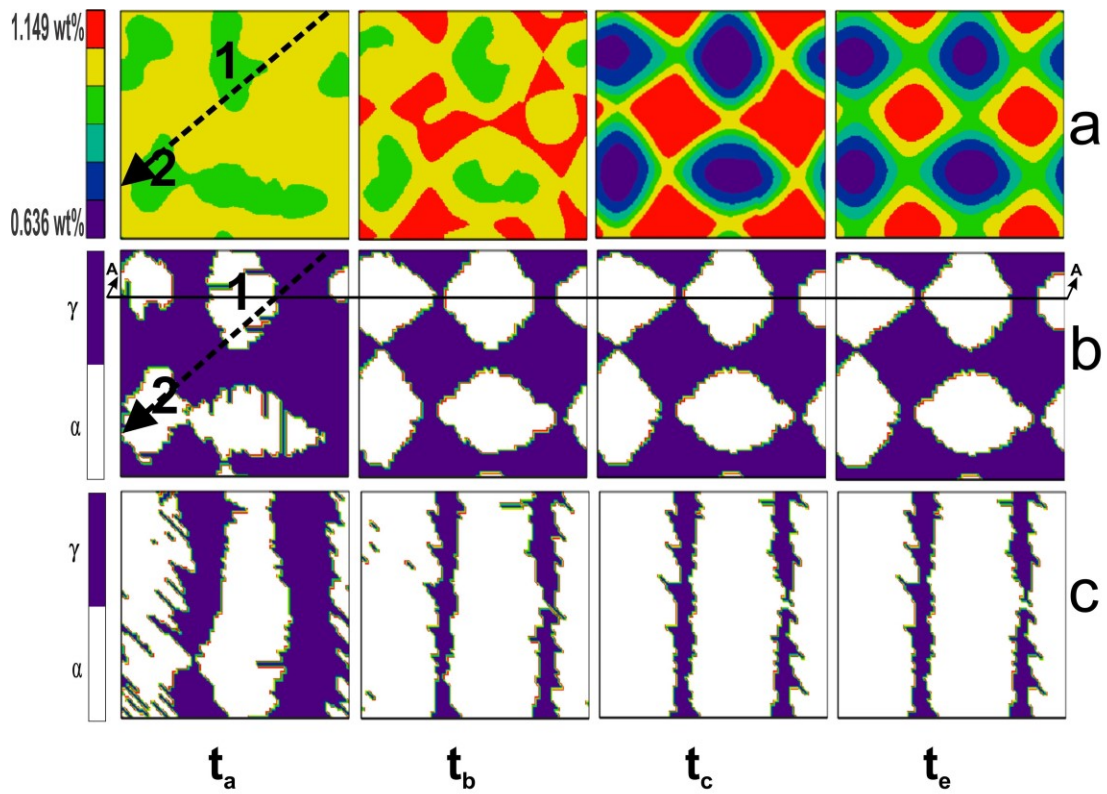


Figure 5-3 Distributions of the carbon concentrations (a) and the sequences of the corresponding structures (b) at different moments of time marked in Fig. 5-1 and Fig. 5-2. (c) shows a vertical cross section of the corresponding structure (b) along the line (A-A). All transformation variants of ferrite are shown in the same colour.

5.3.2 Transformation development with two different carbide nucleation sequences.

In this section, the results obtained by using two different carbide nucleation sequences with different N_{attempt} are presented. The formation of carbides started in both sequences soon after the beginning of the transformation and stopped when the carbon concentration in ferrite was below C_{min} . Fig. 5-4 shows the effect of carbide formation inside ferrite, which corresponded to the first nucleation sequence, on the evolution of the ferrite volume fraction (dotted lines) and the average carbon concentration in solid solutions (dashed lines). This carbide nucleation sequence obtained with N_{attempt} equal to 0.001 produced multiple carbide nucleation events, which started at t_a and reached the total number of carbide sinks equal to 21 at t_c . During the first stage (controlled by the displacive transformation), the first carbide nucleation event was produced at t_a . However, the nucleation of this carbide did not produce an immediate noticeable effect on the transformation process and the transformation rate continued to decrease rapidly from 5.742 at t_a to 0.126 at t_b . The volume fraction of ferrite increased from 0.384 at t_a to 0.466 at t_b and the average carbon concentration in the solid solution slowly decreased from 0.92 wt% at t_a to 0.916 wt% at t_b . When the total number of carbide sinks equal to 6 was produced at t_c , the transformation rate continued to decrease from 0.045 at t_c to

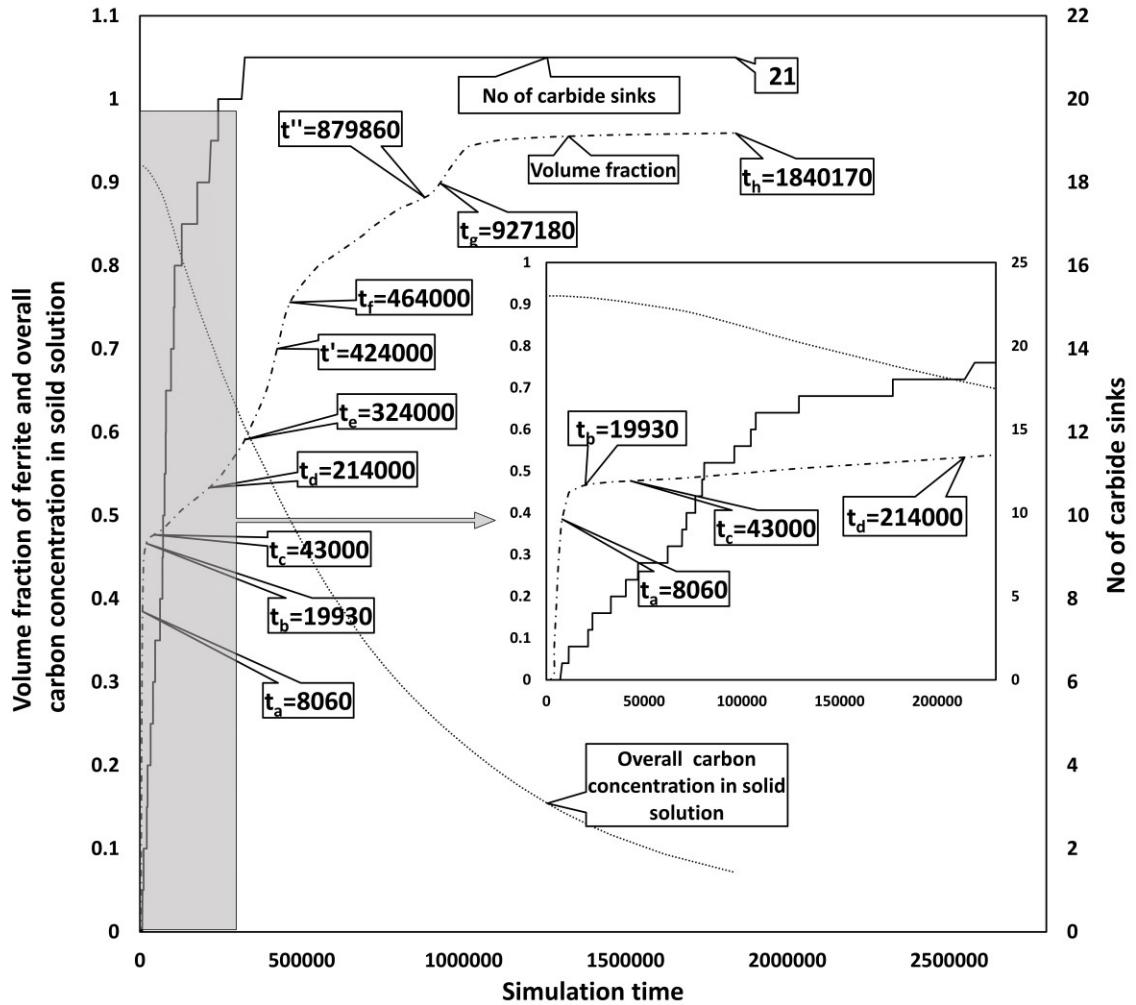


Figure 5-4. The solid line represents the number of carbide sinks introduced at different times; the dashed line shows the evolution of the ferrite volume fraction rat; the dotted line shows the average carbon concentration rate. The initial average carbon concentration in the system is 0.92 wt%; the final average carbon concentration in the system is 0.025 wt% (the carbon content of carbide in equilibrium with ferrite).

0.0322 at t_d with the transformation producing the increase in the volume fraction of ferrite from 0.476 at t_c to 0.533 at t_d . The nucleation of these carbide sinks resulted in a noticeable reduction in the average carbon concentration in the solid solution from 0.903 wt% at t_c to 0.713 wt% at t_d . However, the average carbon content in austenite continued to increase to 1.013 wt% at t_c and reached a high value of 1.165 wt% at t_d . In comparison with Fig. 5-1, the average carbon content in austenite was still below 1.013 wt% at same moment of time ($t=t_c$).

After the total number of carbide sinks increased to 18 at t_d , the average carbon content in austenite decreased to 1.163 wt.% at t_e , and the overall average carbon concentration in solid solution was reduced to 0.605 wt.%. The formation of these carbides contributed to the increase in the volume fraction of ferrite to 0.591 at t_e and resulted in the reacceleration of the transformation rate to 0.0753 at t_e . In contrast, the transformation in the system without carbides (Fig. 5-1) reached a zero rate at t_d with the average carbon content in austenite is 1.153 wt%. Once a total number of carbon sinks reached 21 at t_e , the transformation rate in the system with carbides continued to increase to 0.149 at t' , then slowed down to 0.139 at t_f , and further decreased to 0.0175 at t'' . This slowing down was caused by a small fraction of austenite still remaining in the system (equal to 0.244 at t_f ; see the microstructure presented in Fig. 5-6). However, the transformation rate reaccelerated again to 0.0473 at t_g . The untransformed austenite fraction was equal to 0.100 at t_g when the second reacceleration of the transformation occurred. The transformation eventually proceeded to completion at a very slow rate reaching a zero rate at t_h , with the average carbon concentration at that time equal 0.025 wt.%.

Fig. 5-5 demonstrates the effect of the first carbide sink, formed at t_a (marked in Fig. 5-4), on the evolution of the carbon concentration (coloured solid lines) and the structural boundary locations (coloured dashed lines) along the same dotted arrow as the one in Fig. 5-2 but with carbide nucleation allowed. The pink line represents the carbon concentration at a few time steps before t_a and the coloured solid and dashed lines present the composition distributions and the order parameter profiles at the time moments marked in Fig. 5-4. The first carbide sink produced just before t_a , at t_a resulted in a narrow well in the concentration distribution thus producing a small depletion region inside ferrite grain 1. The structural boundaries at that time were still moving without any observable carbon partitioning between austenite and ferrite. The structural boundary movements of ferrite grain 1 at t_a were similar to the structural boundary movements of ferrite grain 1, which had occurred at the same time in the system without carbides (Fig. 5-2). The ferrite grain 1 evolution (the whole grain shifting and the growth in size) was also the same.

As the transformation proceeded, the carbon exchange at the interfaces between austenite and ferrite began to occur at t_b and resulted in increasing the carbon content in austenite in a way similar to the carbon partitioning at the same moment of time in Fig. 5-2 (in the system without carbides). However, the depletion region inside ferrite grain 1 grew wider and resulted in the decrease in the carbon concentration to 0.821 wt% at the interface between austenite and ferrite grain 1. In contrast, the carbon concentration at

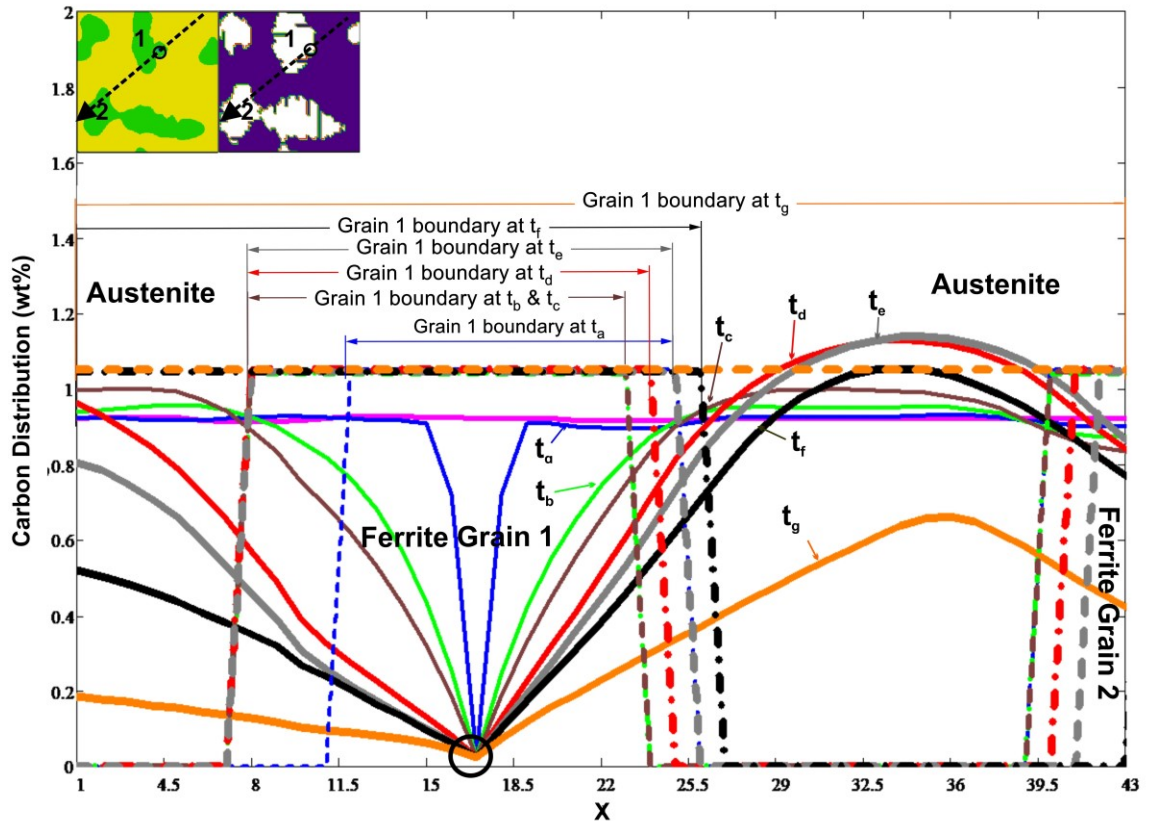


Figure 5-5. One dimensional distributions of the carbon concentration along the dotted white arrow shown in the insert with a two-dimensional concentration map and microstructure at $t=t_a$. The encircled point is the location of the first carbide sink. The coloured solid lines present carbon concentrations at different moments of time; the coloured dashed lines represent different positions of the structural boundaries at different moments of time. All time moments indicated on the curves correspond to time moments indicated by the same letters in Fig. 5-4.

the interface between austenite and ferrite grain 1 in Fig. 5-2 at t_b remained nearly at the initial carbon content (0.92 wt.%). The carbon concentration in austenite in Fig. 5-5 at t_c increased to a similar level of the carbon concentration in austenite at the same moment

of time in the system without carbides (Fig. 5-2). However, the carbon concentration at the interface between austenite and ferrite grain 1 in Fig. 5-2 at t_c still remained at the initial carbon content while the expanded depleted region around carbide in Fig. 5-5 at the same moment of time continued to reduce the carbon concentration at the interface between austenite and ferrite grain 1 to 0.772 wt%. Fig. 5-5 demonstrates that the development of the local stasis (no movement of the structural boundaries from t_b), which occurred from t_b to t_c , is similar to the local stasis development in Fig. 5-2 during the same time period, although the observable reduction of the carbon concentration occurred in Fig. 5-5 during that time period at the interface between austenite and ferrite grain 1.

A significant difference between Fig. 5-2 and Fig. 5-5 can be observed at t_d and at the later time moments. The structural boundaries presented in Fig. 5-5 at t_d resumed the movement resulting from a significant decrease of the carbon concentration (down to 0.65 wt% at the interface between ferrite and austenite) caused by the expansion of the depleted region inside ferrite grain 1 while the carbon content in austenite at that time reached the value of 1.140 wt%. The deep and wide carbon depletion zone inside ferrite grain 1 at t_d provided an extra driving force to allow the transformation to take place as presented by the movement of the structural boundaries in Fig. 5-5 at t_d . In contrast, the carbon partitioning between austenite and ferrite grain 1 in the system without carbides at t_d (Fig. 5-2) produced an enriched layer around the ferrite grains with a slight increase in the carbon content at the interface between austenite and ferrite grain 1 and prevented any movement of the structural boundaries. The ferrite grains in Fig. 5-5 at t_d have rod-like shapes (the microstructure shown in Fig. 5-6 at same moment of time ($t=t_d$)) similar

to the ferrite grain shapes in Fig. 5-3 at time $t = t_d$. In Fig. 5-5, at t_e , the maximum concentration in the austenite grain reached the value of 1.150 wt% and after that the maximum concentration of carbon in austenite decreased as the effect of the carbon sink in the ferrite grain spread to the whole volume of the austenite grain, and the partitioning ceased to play a dominant role in the evolution of the carbon concentration in austenite. The structural boundaries then continued to move until the completion of the transformation, at which time the concentration distribution flattened at approximately 0.025 wt.% in the whole system.

Fig. 5-6 a illustrates the distributions of the carbon concentration (upper) and the respective microstructure sequences (lower) at different moments of time shown as t_a , t_c , t_d , t_e , t_f , t' and t_g on the transformation curve in Fig. 5-4 obtained when the carbide formation with the first nucleation sequence was introduced. The point marked by a circle on the carbon concentration map represents the location of the first carbide nucleated at t_a in supersaturated ferrite. Fig. 5-6 indicates that the carbon distribution remained mostly unaffected by the transformation at t_a and the carbon enriched layer began to form in austenite at the boundary between austenite and the ferrite grain at t_b . The rod-like morphology of the ferrite grains obtained at t_b is more efficient for the diffusion-controlled growth process wherein carbon partitions to austenite. The microstructure obtained at t_d in the systems with carbides (Fig. 5-6) is similar to the final microstructure in the system without carbides (Fig. 5-3) with only a slightly larger size of ferrite grains and a stronger carbon partitioning in the former system as illustrated in Fig 5-5. At $t = t_e$,

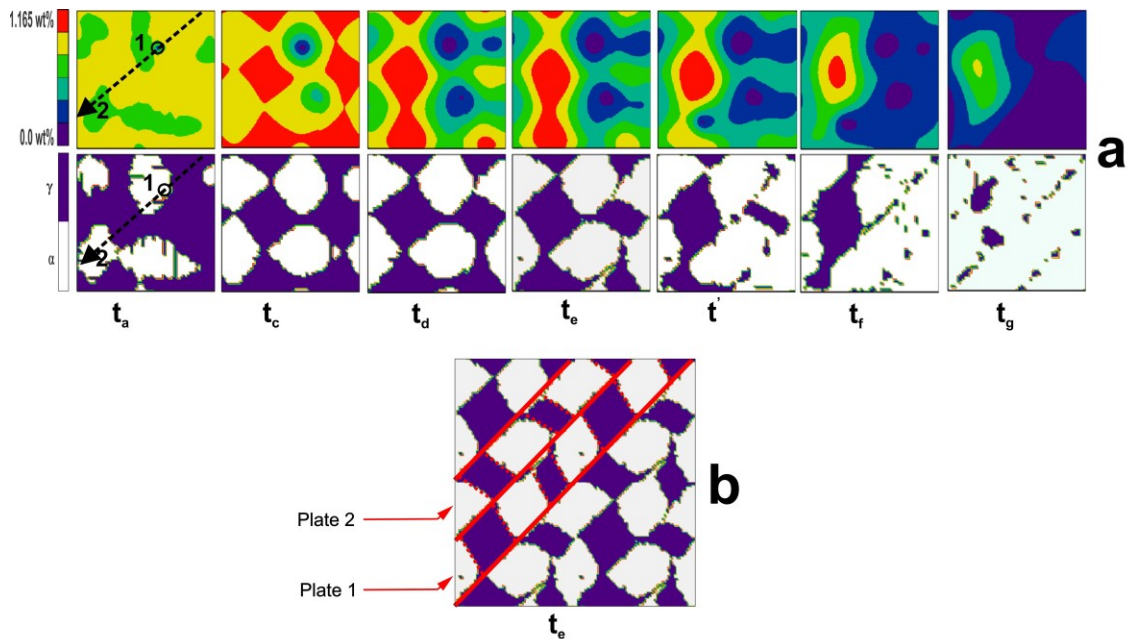


Figure 5-6 (a) Distributions of the carbon concentrations sequences (upper) and respective structure (lower) at different moments of time marked in Fig. 5-4. (b) Periodic repetition of the structure shown in Fig. 5-6 a at the moment of time $t = t_e$. Solid red lines outline the boundaries of composite austenite-ferrite plates; dotted red lines outline the austenite-ferrite interfaces in the plates. All transformation variants of ferrite are shown in the same colour.

once total of 21 carbon sinks have been produced in the system, the morphology of ferrite grains changed to a more regular pattern with a well-defined arrangement of austenite and the ferrite grains. The microstructure at t_e (shown in Fig. 5-6 b) consists of composite plates with parallel boundaries outlined by red lines. Each of the composite plates consists of the rods of austenite and ferrite with the boundaries between the rods within each plate parallel to each other. There are only two possible orientations of the austenite

- ferrite boundaries in all plates (such as in plate 1 and in plate 2). This morphology has been maintained until the completion of the transformation.

Fig. 5-7 illustrates the effect of carbide nucleation with the second sequence (producing 190 carbide sinks starting at t_a and ending at t_b) on the evolution of the ferrite volume fraction (dotted lines) and the average carbon concentration in the solid solutions (dashed lines). This nucleation sequence was obtained using N_{attempt} equal to 1. During this process, at t_b , the transformation rate decreased to 0.517 which is higher than the transformation rate at the same moment of time in Fig. 5-4, and the average carbon concentration in the solid solution rapidly decreased from 0.92 wt% at t_a to 0.609 wt% at t_b . The ferrite volume fraction at t_b was 0.557 which is higher than the 0.465 volume fraction of ferrite at the same moment of time in Fig. 5-4. This nucleation sequence also resulted in the increase in the average carbon content in austenite to 1.074 wt% at t_b which is higher than 0.973 wt% of the average carbon content in austenite obtained in the system with the first nucleation sequence at the same moment of time (Fig. 5-4). When there were no further carbide sinks introduced after t_b , we can see that the transformation rate continued to decrease to 0.283 at t_c with the average carbon concentration in the solid solution reduced further to 0.394 wt%. However, the overall carbon content in austenite at t_c increased to 1.103 wt.% at that time. The transformation rate then reaccelerated to 0.298 at t_d when the average carbon content in austenite decreased to 1.036 wt.% and remaining fraction of austenite reached 0.311. It was observed that when the transformation accelerated in the system with 190 carbides at time t_d , the microstructure (Fig. 5-8) had the morphology similar to the arrangement of the ferrite

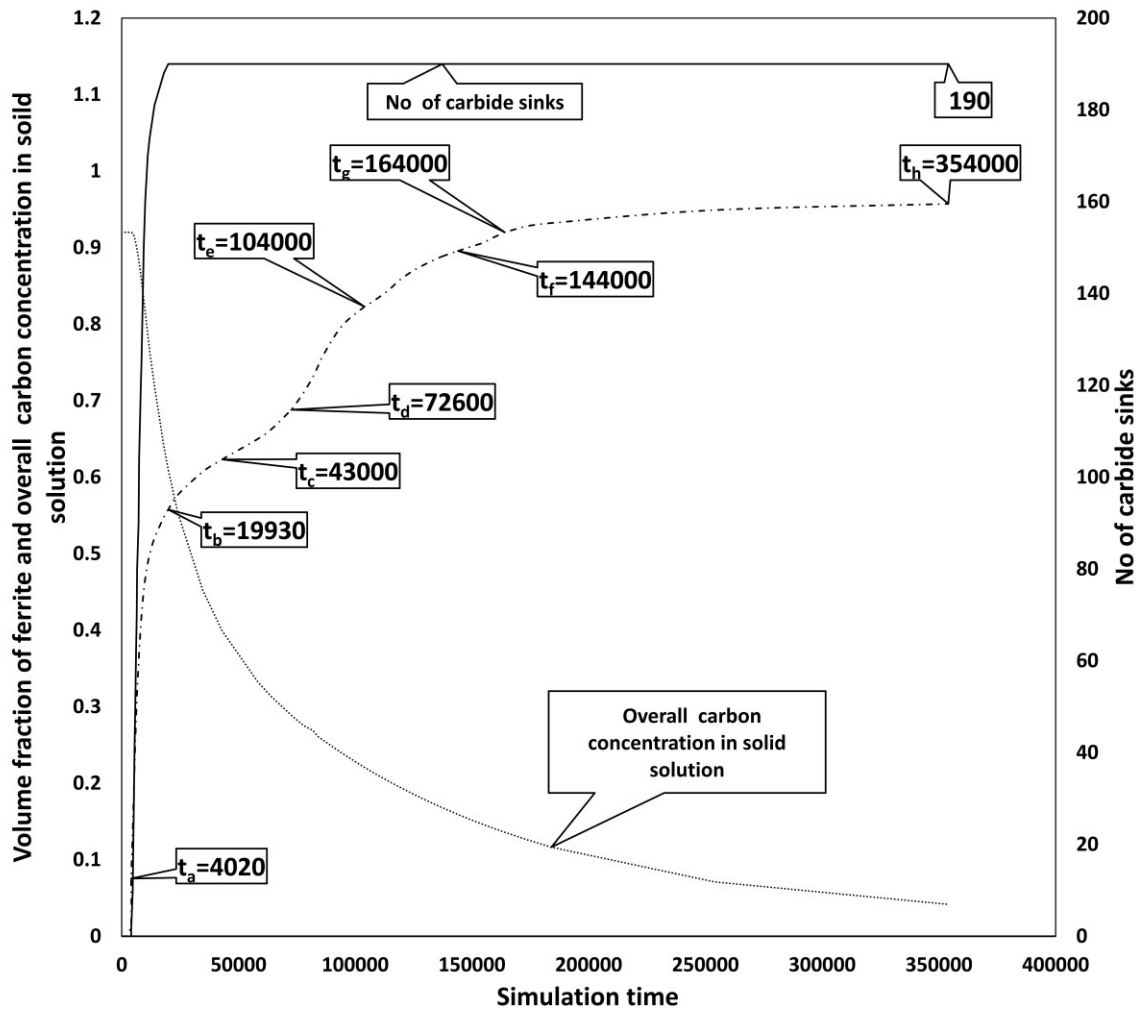


Figure 5-7 Solid line represents the number of carbide sinks introduced at different time; dashed line shows the evolution of the ferrite volume fraction rate; dotted line shows the average carbon concentration rate. The initial average carbon concentration in the system is 0.92 wt%; the final average carbon concentration in the system is 0.025 wt%.

grains and residual austenite in the system with 21 carbides (Fig. 5-6) at the time when the transformation reaccelerated in that system at t_e .

The transformation rate decreased in the system with 190 carbides to 0.262 at t_e and further slowed down to 0.114 at t_f . This decrease in the transformation rate can be attributed to the decrease in the volume fraction of residual austenite available for the

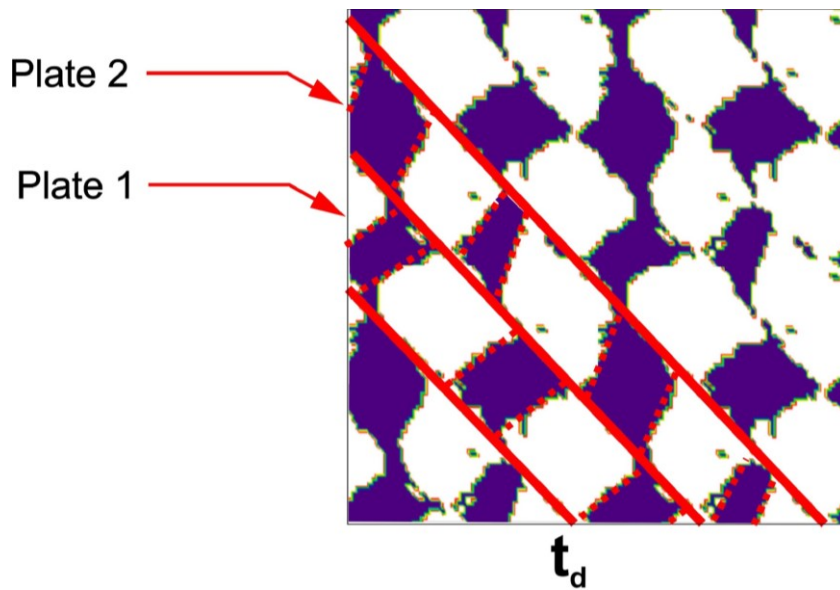


Figure 5-8. Periodic repetition of the structure at time $t = t_d$ marked in Fig. 5-7. All transformation variants of ferrite are shown in the same colour.

transformation (the volume fraction of austenite dropped to 0.177 at t_e). The overall transformation rate briefly reaccelerated again to 0.219 at t_g . The untransformed austenite fraction was equal to 0.079 at t_g when the second reacceleration of the transformation occurred. A similar second reacceleration of the transformation in the system with 21 carbides (Fig. 5-4) occurred when the volume fraction of untransformed austenite was equal to 0.100. The transformation reached the termination state in the system with 190

carbides with the same average carbon concentration in the solid solution equal to 0.025 wt% as in the system with 21 carbides.

5.4 Discussion

The simulation results have demonstrated that if the transformation develops without carbide formation, then it has two stages. The first stage takes place with rapid kinetics controlled by the displacive transformation (as it was shown in [65]) and supersaturated ferrite grows without any noticeable partitioning effects with the same carbon concentration as in austenite. The beginning of the second stage occurs when the transformation slows down as a result of the build up of the elastic energy and the onset of the partitioning effect at the interface between austenite and ferrite leading to the build up of the carbon concentration in austenite (Fig. 5-1b). At the end of the second stage, a full stasis is reached when the fraction of residual austenite is approximately equal to 0.5. When the state of the full stasis is reached, the partitioning of carbon from ferrite to austenite continues, and the main part of the carbon transfer to austenite occurs during the stasis. If carbides are produced during the transformation, the transformation develops in three stages. The first and second stages are similar to those in the system without carbides, however, at the end of the second stage the reacceleration occurs instead of a full stasis and the transformation proceeds to completion. Such a development of the third stage of the bainitic transformation caused by the formation of carbides in ferrite was observed experimentally in [28, 39, 83].

In both models, with a different number of carbides nucleated in supersaturated ferrite, carbides appear before any significant partitioning of carbon occurs. Such a formation of carbides in supersaturated ferrite during the displacive transformation was reported experimentally in [10, 20, 23, 24, 26, 27, 67, 72, 77, 81, 91-102]. The partitioning starts after carbides have nucleated and, for a while, it plays a dominant role in the evolution of the carbon concentration in austenite. The effect of carbides acting as carbon sinks inside ferrite is initially localised inside ferrite and does not have a strong impact on *i*) the transformation rate, which continues to decrease, and *ii*) the carbon concentration inside austenite. Such a coexistence of carbon sinks acting in ferrite and carbon partitioning from ferrite to austenite was observed experimentally in [67, 72]. The diffusion-controlled growth is dominant at this stage as long as carbon is still partitioned from ferrite to austenite. Also, due to carbon partitioning, the carbon content on the ferrite side of the austenite-ferrite interface decreases below C_{\min} , which results in the suppression of further carbide formation in the regions along the interface. This mechanism is similar to the mechanism of the formation of a carbide-free zone suggested in [92] on the basis of the experimental results presented there.

Although the diffusion-controlled growth in the second stage is dominant, two other hidden effects are involved: carbon depletion and elastic interactions. The carbon depletion by carbides initially produces a weak effect on the transformation only slightly increasing the transformation rate even in the system with a large number of carbides. However, the depleted regions grow with time and reach the interface with austenite. Starting from this moment, the concentration of carbon in austenite at the interface with ferrite starts to decrease providing an additional driving force for the transformation. The

effect of carbon sinks on the carbon concentration is still limited by a very thin interface region, and in the depth of austenite, the evolution of the concentration is still dominated by the partitioning effects. During this part of the transformation process, the competition between carbon depletion by carbides and the partitioning into austenite continues as it was suggested in [67, 72].

Eventually, the effect of carbon sinks spreads over the whole volume of the material, and the carbon concentration starts to decrease in austenite far from the interface with ferrite. Starting from that moment, the diffusion of carbon to carbides determines the kinetics of the transformation, and the transformation rate significantly increases. A weaker role of diffusion between austenite and ferrite results in a stronger control of the microstructure morphology by elastic interactions. The microstructure acquires a regular pattern consisting of parallel composite austenite-ferrite plates having approximately the same thickness. Austenite and ferrite inside the plates form a structure with parallel habit planes. Such a regular microstructure pattern provides an evidence of an important role played by elastic interactions in the evolution of the microstructure.

The comparison of the transformation paths in the systems with different numbers of carbides demonstrates that, even though there are expected quantitative differences, these paths have the same basic type of the transformation development with three transformation stages. A larger number of carbides results, as can be expected, in a slightly higher transformation rate at the second stage; however, the transformation rate still decreases with time and is much lower than at the first stage. In both cases the effect of carbides on the transformation rate is initially small and increases only after some period of time when the effect of carbon sinks on the carbon concentration spreads well

into austenite. A significant reduction of the carbon content in the whole volume then results in the re-acceleration of the transformation. A similar slowing down and reacceleration of the transformation rate during the bainitic transformation were observed experimentally in [81].

5.5 Conclusions

1. Over a period of time, the formation of carbides in ferrite leads to a higher rate of the transformation and produces a three-stage transformation path with a re-accelerated third stage and a full transformation completion.
2. In the absence of carbides, the transformation is terminated at approximately 0.5 volume fraction of the material remaining in the austenitic state. However, even when a full stasis of the structural transformation is reached, the partitioning of carbon from ferrite to austenite still continues, and most of the partitioning effect may be produced during the stasis.
3. After the nucleation of carbides, the effect produced by carbon sinks inside ferrite coexists with the effect produced by carbon partitioning from ferrite to austenite. The latter results in the formation of a carbon depleted zone in ferrite near the interface with austenite wherein any further nucleation of carbides is impossible.

4. The expansion of the depleted regions around carbides eventually leads to the carbon concentration reduction at the ferrite - austenite interface and, later, to the decrease in the carbon concentration in the whole volume, thus causing the re-acceleration of the transformation and leading to its completion.

5. A strong depletion of carbon results in the increase in the role of elastic interactions in the microstructure evolution and the formation of regular phase patterns with well-defined habit planes.

Chapter 6: Conclusions

A phase field method was used to investigate the roles of the displacive transformation, the diffusion process and carbide formation in the bainitic type transformation, and the interaction between these processes. The bainitic type transformation exhibited a complex behavior due to a simultaneous occurrence of these processes. This behavior cannot be fully described using conventional nucleation and growth models, such as the Johnson-Mehl-Avrami-Kolmogorov model; therefore, a phase field method was used to simulate the evolution of the microstructure. The use of the phase field method allowed for an investigation of the effect of coherency elastic interactions and its role in controlling the ferrite morphology. The conclusions of the thesis are presented as follows:

The formation of carbide-free bainite and the interaction between a displacive transformation and diffusion process.

The bainitic type transformation excluding carbide formation develops in two stages: the first, fast stage, wherein bainitic ferrite grows without any change in the carbon concentration, with the displacive mechanism being dominant at this stage. At the second stage, the diffusion process takes place, leading to the formation of a saturation layer around ferrite grains, thereby resulting in the retardation of the transformation rate.

The ferrite morphology can be controlled by either a diffusion-controlled growth process or the elastic energy, depending on the thermodynamic conditions and diffusion mobility. Thus, the model of the bainitic transformation should include the displacive mechanism and diffusion process because both of them produce coherency strain effects.

Interaction between three processes (displacive transformation, diffusion process and carbide formation) in the bainitic type transformation.

The bainitic type transformation including carbide formation was modeled using carbon sinks acting as carbides either in austenite or in supersaturated bainitic ferrite. This approach, combining the effect of the displacive transformation, diffusion process and carbide formation, allowed for the investigation of the role of carbides and its effect on kinetics of the bainitic transformation. Carbide formation in both cases (carbides forming either in austenite or in supersaturated bainitic ferrite) produces a three-stage transformation path with a re-accelerated third stage with the length of the stasis period and the rate of the reaccelerated transformation being strongly sensitive to the density of carbides.

Carbide formation in retained austenite plays a secondary role by *i*) reducing the carbon concentration in ferrite and creating the condition for the reacceleration of the austenite to ferrite transformation, and *ii*) shifting the kinetic control of the morphology of ferrite grains from the diffusion process to elastic interaction.

While carbide formation in supersaturated bainitic ferrite coexists with the effect produced by carbon partitioning from ferrite to austenite resulting in the formation of a

carbide free zone on the ferrite side of the austenite-ferrite interface. A strong depletion of carbon in supersaturated bainitic ferrite results in the increase in the role of elastic interactions in the microstructure evolution and the formation of regular phase patterns with well defined habit planes.

Appendix A

The aim of this appendix is to determine the number of different transformation variants by the orientation relationships between the product and parent phase. There are two types of orientation relationships usually applied to bainitic and martensitic transformations, i.e., the Kurdjumov-Sachs (K-S) [104, 105] and Nishiyama- Wasserman (N-W) [32, 60, 106]. There are 24 different orientation relationships according to the K-S model and 12 according to the N-W model; however, larger numbers of orientation relationships in the K-S and N-W models, as compared to just three product phase variants used in the phase field model, are due to the combinations of the transformation strains and rotations in the K-S and N-W orientation relationships. Let's consider, for example, one of the N-W orientation relationships with the $(111)_\gamma$ plane of the FCC parent phase parallel to the $(011)_\alpha$ plane of the BCC product phase, the $[\bar{1}10]_\gamma$ direction in the $(111)_\gamma$ plane parallel to the $[\bar{1}00]_\alpha$ direction in the $(011)_\alpha$ plane and the $[11\bar{2}]_\gamma$ direction in the $(111)_\gamma$ plane parallel to the $[01\bar{1}]_\alpha$ direction in the $(011)_\alpha$ plane. The orientation relationship determines the transformation tensor describing the displacement of atoms during the transformation from the FCC to BCC lattice. That tensor can be found from the stretches produced in the directions aligned with each other in the orientation relationship between the FCC and BCC lattice. Thus, for and the FCC to BCC transformation with the lattice parameters $\gamma=0.357nm$ and $\alpha=0.287nm$ and with orientation relationship presented above, the transformation stretches are determined by:

$$\mathbf{u}_1 = \frac{\begin{bmatrix} -1 \\ 1 \\ 0 \end{bmatrix}}{\sqrt{(-1)^2 + (1)^2 + (0)^2}} \Rightarrow \mathbf{u}_1 = \begin{bmatrix} -0.707 \\ 0.707 \\ 0 \end{bmatrix} \quad a_1 = \frac{0.287\sqrt{2}}{0.357} = 1.1369167854 \quad (\text{A.1})$$

$$\mathbf{u}_2 = \frac{\begin{bmatrix} 1 \\ 1 \\ -2 \end{bmatrix}}{\sqrt{(1)^2 + (1)^2 + (-2)^2}} \Rightarrow \mathbf{u}_2 = \begin{bmatrix} 0.408 \\ 0.408 \\ -0.816 \end{bmatrix} \quad a_2 = \frac{0.287 \cdot 2\sqrt{2}}{0.357 \cdot \sqrt{6}} = 0.9282886681 \quad (\text{A.2})$$

$$\mathbf{u}_3 = \frac{\begin{bmatrix} 1 \\ 1 \\ 2 \end{bmatrix}}{\sqrt{(1)^2 + (1)^2 + (2)^2}} \Rightarrow \mathbf{u}_3 = \begin{bmatrix} 0.408 \\ 0.408 \\ 0.816 \end{bmatrix} \quad a_3 = \frac{0.287 \cdot 2\sqrt{2}}{0.357 \cdot \sqrt{6}} = 0.9282886681 \quad (\text{A.3})$$

$$\mathbf{u}_4 = \frac{\begin{bmatrix} 1 \\ 1 \\ 1 \end{bmatrix}}{\sqrt{(1)^2 + (1)^2 + (1)^2}} \Rightarrow \mathbf{u}_4 = \begin{bmatrix} 0.577 \\ 0.577 \\ 0.577 \end{bmatrix} \quad a_4 = \frac{0.287\sqrt{2}}{0.357 \cdot \sqrt{6}} = 0.9282886681 \quad (\text{A.4})$$

where $\mathbf{u}_1, \mathbf{u}_2, \mathbf{u}_3, \mathbf{u}_4$ are unit vectors corresponding to different stretch directions and a_1, a_2, a_3, a_4 are stretch values in the corresponding directions. Transformation tensor \mathbf{T} can be found [18, 32] by solving:

$$\mathbf{T} \cdot \mathbf{u}_1 = a_1 \cdot \mathbf{u}_1 \quad (\text{A.5})$$

$$\mathbf{T} \cdot \mathbf{u}_2 = a_2 \cdot \mathbf{u}_2 \quad (\text{A.6})$$

$$\mathbf{T} \cdot \mathbf{u}_3 = a_3 \cdot \mathbf{u}_4 \quad (\text{A.7})$$

The lattice transformation involves lattice deformation \mathbf{F} and lattice rotation \mathbf{R} , so that $\mathbf{T}=\mathbf{R}\cdot\mathbf{F}$. The deformation tensor can be separated from the rotation tensor by using:

$$\mathbf{T}^2 = \mathbf{T}^T \cdot \mathbf{T} = \mathbf{F}^T \cdot \mathbf{R}^T \cdot \mathbf{R} \cdot \mathbf{F} = \mathbf{F}^T \cdot \mathbf{F} \quad (\text{A.8})$$

Then the transformation strain tensor \mathbf{E} can be obtained by using:

$$\mathbf{E} = \mathbf{e} \cdot |\mathbf{F}| \cdot \mathbf{e}^{-1} - \mathbf{I} \quad (\text{A.9})$$

where \mathbf{I} is the identity matrix, \mathbf{e} is the tensor in which the e_{ij} component is equal to the j -th component of the i -th eigenvector of \mathbf{T}^2 and $|\mathbf{F}|$ is diagonal matrix with the square roots of the eigenvalues of \mathbf{T}^2 . Using Eq. (A.5-A.9), the transformation tensor \mathbf{E} corresponding to relationships (A.1- A.4) can be obtained as:

$$\mathbf{E} = \begin{bmatrix} 0.137 & 0 & 0 \\ 0 & 0.137 & 0 \\ 0 & 0 & -0.196 \end{bmatrix} \quad (\text{A.10})$$

Using all the 12 NW orientation relationships, only three different transformation strain tensors can be obtained:

$$\varepsilon_{ij}^{00}(\mathbf{1}) = \begin{bmatrix} 0.137 & 0 & 0 \\ 0 & 0.137 & 0 \\ 0 & 0 & -0.196 \end{bmatrix} \quad (\text{A.11})$$

$$\varepsilon_{ij}^{00}(2) = \begin{bmatrix} 0.137 & 0 & 0 \\ 0 & -0.196 & 0 \\ 0 & 0 & 0.137 \end{bmatrix} \quad (\text{A.12})$$

$$\varepsilon_{ij}^{00}(3) = \begin{bmatrix} -0.196 & 0 & 0 \\ 0 & 0.137 & 0 \\ 0 & 0 & 0.137 \end{bmatrix} \quad (\text{A.13})$$

and each of these strain tensors corresponds to four different orientation relationships having different rotations [105]. It should be noted that the form of the strain tensor is sensitive to the accuracy of calculations. The calculations with a lower accuracy can produce transformation strains with non-zero off-diagonal terms and can also generate more than three different strain tensors. For example, if a four-digit accuracy is used, then a strain tensor will become

$$\varepsilon_{ij}^{00}(1) = \begin{bmatrix} 0.137 & -0.0006 & 0.0002 \\ -0.0006 & 0.137 & 0.0002 \\ 0.0002 & 0.0002 & -0.196 \end{bmatrix} \quad (\text{A.14})$$

instead of $\varepsilon_{ij}^{00}(1)$ shown in Eq. (A,11), and 12 different looking strain tensors will be produced.

References

- [1] G. Rees, H. Bhadeshia, Bainite transformation kinetics part 1 modified model, *Materials Science and Technology* 8 (11) (1992) 985–993.
- [2] N. Chester, H. Bhadeshia, Mathematical modelling of bainite transformation kinetics, *Le Journal de Physique IV* 7 (C5) (1997) C5–41 – C5–46.
- [3] H. Matsuda, H. Bhadeshia, Kinetics of the bainite transformation, *Proceedings of the Royal Society of London Series A: Mathematical, Physical and Engineering Sciences*. 460 (2046) (2004) 1707–1722.
- [4] H. Bhadeshia, Bainite: Overall transformation kinetics, *Le Journal de Physique Colloques* 43 (C4) (1982) C4–443 – C4–448 .
- [5] S. Samanta, P. Biswas, S. Giri, S. B. Singh, S. Kundu, Formation of bainite below the ms temperature: Kinetics and crystallography, *Acta Materialia* 105 (2016) 390–403.
- [6] M. Hillert, Diffusion in growth of bainite, *Metallurgical and Materials Transactions A* 25 (9) (1994) 1957–1966.
- [7] Z. Yang, W. Xu, Z. Yang, C. Zhang, S. van der Zwaag, A 2d analysis of the competition between the equiaxed ferritic and the bainitic morphology based on a gibbs energy balance approach, *Acta Materialia* 105 (2016) 317–327.
- [8] M. Düsing, R. Mahnken, Simulation of lower bainitic transformation with the phase-field method considering carbide formation, *Computational Materials Science*. 111 (2016) 91-100.

- [9] Morteza Toloui, Matthias Militzer, Phase field modeling of the simultaneous formation of bainite and ferrite in TRIP steel, *Acta Mater.* 144 (2018) 786–800.
- [10] F. G. Caballero, M. K. Miller, C. Garcia-Mateo, J. Cornide, M.J. Santofimia, Temperature dependence of carbon supersaturation of ferrite in bainitic steels, *Scripta Materialia.* 67(10) (2012) 846-849.
- [11] F. G. Caballero, C. Garcia-Mateo, M. Santofimia, M. K. Miller, C. G. De Andres, New experimental evidence on the incomplete transformation phenomenon in steel, *Acta Mater.* 57 (1) (2009) 8–17.
- [12] M. Griebel, S. Knapek, G. Zumbusch, Numerical Simulation in Molecular Dynamics: Numerics, Algorithms, Parallelization, Applications, 1st Edition, Springer Publishing Company, Incorporated, 2007.
- [13] Y. Chen, C. A. Schuh, A coupled kinetic monte carlo-finite element mesoscale model for thermoelastic martensitic phase transformations in shape memory alloys, *Acta Materialia* 83 (2015) 431-447.
- [14] M. Zhu, S. Lee, C. Hong, Modified cellular automaton model for the prediction of dendritic growth with melt convection, *Physical Review E* 69 (6) (2004) 061610.
- [15] Y. Le Bouar, A. Khachaturyan, Mechanism and modeling of saw-tooth structure formation in the L12–L10 two-phase system, *Acta materialia* 48 (8) (2000) 1705–1717.
- [16] Y. Wang, A. Khachaturyan, Three-dimensional field model and computer modeling of martensitic transformations, *Acta Mater.* 45 (2) (1997) 759–773.

- [17] L.-Q. Chen, Phase-field models for microstructure evolution, *Annual review of materials research* 32 (1) (2002) 113–140.
- [18] A. G. Khachaturyan, *Theory of structural transformations in solids*, Wiley, New York, 1983.
- [19] F. G. Caballero, M. K. Miller, S. S. Babu, C. Garcia-Mateo, Atomic scale observations of bainite transformation in a high carbon high silicon steel, *Acta Materialia* 55 (1) (2007) 381–390.
- [20] H. K. D. H. Bhadeshia, *Bainite in steels: transformations, microstructure and properties*, Inst. of Materials, London, 1992.
- [21] R.F. Hehemann, K.R. Kinsman, H.I. Aaronson, A debate on the bainite reaction, *Metallurgical Transactions*. 3 (5) (1972) 1077-1094.
- [22] H.K.D.H. Bhadeshia, A.R. Waugh, Bainite: An atom-probe study of the incomplete reaction phenomenon, *Acta Metallurgica*. 30(4) (1982) 775-784.
- [23] L. C Chang, Microstructures and reaction kinetics of bainite transformation in Si-rich steels, *Materials Science and Engineering A*. 368 (1-2) (2004) 175-182.
- [24] Annika Borgenstam, Mats Hillert, and John Ågren, Metallographic evidence of carbon diffusion in the growth of bainite, *Acta Materialia*. 57 (11) (2009) 3242-3252.
- [25] H.-S. Fang, J.-B. Yang, Z.-G. Yang, B.-Z. Bai, The mechanism of bainite transformation in steels, *Scripta Materialia*. 47 (3) (2002) 157-162.
- [26] H. K. D. H. Bhadeshia, The lower bainite transformation and the significance of carbide precipitation, *Acta metallurgica*. 28 (8) (1980) 1103-1114.

- [27] F. G. Caballero, M. K. Miller, C. Garcia-Mateo, Influence of transformation temperature on carbide precipitation sequence during lower bainite formation, *Materials Chemistry and Physics*. 146(1-2) (2014) 50-57.
- [28] Hao Chen, Kangying Zhu, Lie Zhao, Sybrand van der Zwaag, Analysis of transformation stasis during the isothermal bainitic ferrite formation in Fe–C–Mn and Fe–C–Mn–Si alloys, *Acta Materialia*. 61(14) (2013) 5458-5468.
- [29] G. Kurdjumov and G. Sachs, *Z. Phys.*, Vol.34, 1930, pp.325.
- [30] C. Mesplont, B. C. De Cooman, Effect of austenite deformation on crystallographic texture during transformations in microalloyed bainitic steel, *Materials science and technology*. 19 (7) (2003) 875-86.
- [31] Z. Nishiyama, *Sci. Rep. Tohoku Imp. Univ.*, 19341, Vol.23, 1935, pp.638.
- [32] Z. Guo, C. Lee, J. Morris Jr, On coherent transformations in steel, *Acta materialia* 52 (19) (2004) 5511–5518.
- [33] B. Muddle, J. Nie, Formation of bainite as a diffusional displacive phase transformation, *Scripta Materialia* 47 (3) (2002) 187-192.
- [34] Y. Ohmori, T. Maki, Bainitic transformation in view of displacive mechanism, *Materials Transactions, JIM* 32 (8) (1991) 631–641.
- [35] A. B. Greninger, A. R. Troiano, Crystallography of austenite decomposition, *Trans. AIME* 140 (1940) 307-331.
- [36] M. Peet, S. Babu, M. Miller, H. Bhadeshia, Three-dimensional atom probe analysis of carbon distribution in low-temperature bainite, *Scripta Materialia* 50 (10) (2004) 1277–1281.

- [37] M. Hillert, Diffusion and interface control of reactions in alloys, *Metallurgical Transactions A* 6 (1) (1975) 5–19.
- [38] J. G. Speer, D. V. Edmonds, F. C. Rizzo, D. K. Matlock, Partitioning of carbon from supersaturated plates of ferrite, with application to steel processing and fundamentals of the bainite transformation, *Current Opinion in Solid State and Materials Science* 8 (3-4) (2004) 219–237.
- [39] W. Reynolds, F. Li, C. Shui, H. Aaronson, The incomplete transformation phenomenon in Fe-C-Mo alloys, *Metallurgical Transactions A* 21 (6) (1990) 1433–1463.
- [40] H. Aaronson, G. Spanos, W. Reynolds Jr, A progress report on the definitions of bainite, *Scripta Materialia* 47 (3) (2002) 139–144.
- [41] C. Magee, The nucleation of martensite, *Phase Transformations* 115 (1970) 115–156.
- [42] H. Bhadeshia, The bainite transformation: unresolved issues, *Materials Science and Engineering: A* 273 (1999) 58–66.
- [43] L. C. Chang, H. K. D. H. Bhadeshia, Austenite films in bainitic microstructures, *Materials Science and Technology* 11 (9) (1995) 874–882.
- [44] F. G. Caballero, M. K. Miller, C. Garcia-Mateo, Carbon supersaturation of ferrite in a nanocrystalline bainitic steel, *Acta Mater.* 58 (7) (2010) 2338–2343.
- [45] G. Olson, H. Bhadeshia, M. Cohen, Coupled diffusional/displacive transformations, *Acta Metallurgica* 37 (2) (1989) 381–390.

- [46] S. Mujahid, H. Bhadeshia, Coupled diffusional/displacive transformations: effect of carbon concentration, *Acta metallurgica et materialia* 41 (3) (1993) 967–973.
- [47] Y. Jin, A. Artemev, A. Khachaturyan, Three-dimensional phase field model of low-symmetry martensitic transformation in polycrystal: simulation of ξ' 2 martensite in auctd alloys, *Acta materialia* 49 (12) (2001) 2309–2320.
- [48] A. Artemev, Y. Jin, A. Khachaturyan, Three-dimensional phase field model of proper martensitic transformation, *Acta materialia* 49 (7) (2001) 1165–1177.
- [49] P. Song, Y. Ji, L. Chen, W. Liu, C. Zhang, L.-Q. Chen, Z. Yang, Phase-field simulation of austenite growth behavior: Insights into the austenite memory phenomenon, *Computational Materials Science* 117 (2016) 139–150.
- [50] Y. Le Bouar, A. Loiseau, A. Khachaturyan, Origin of chessboard-like structures in decomposing alloys. theoretical model and computer simulation, *Acta materialia* 46 (8) (1998) 2777–2788.
- [51] Y. Wang, D. Banerjee, C. Su, A. Khachaturyan, Field kinetic model and computer simulation of precipitation of L12 ordered intermetallics from fcc solid solution, *Acta materialia* 46 (9) (1998) 2983–3001.
- [52] Y. Wen, Y. Wang, L. Bendersky, L.-Q. Chen, Microstructural evolution during the $\alpha_2 \rightarrow \alpha_2 + O$ transformation in Ti–Al–Nb alloys: phase-field simulation and experimental validation, *Acta materialia* 48 (16) (2000) 4125–4135.
- [53] Y. Ni, Y. Jin, A. Khachaturyan, The transformation sequences in the cubic \rightarrow tetragonal decomposition, *Acta Mater.* 55 (14) (2007) 4903–4914.

- [54] A.G. Khachaturyan, G. Shatalov, Theory of macroscopic periodicity for a phase transition in the solid state, *Soviet Phys. JETP* 29 (3) (1969) 557–561.
- [55] S. Chupatanakul, Kinetics of Bainite Transformation in Carburized 4317 M2. PhD thesis, Illinois Institute of Technology (2006).
- [56] Wang, Y.U., Y.M. Jin, and A.G. Khachaturyan, Phase field microelasticity theory and modeling of elastically and structurally inhomogeneous solid. *Journal of Applied Physics*, 2002. 92(3): p. 1351-1360.
- [57] Y. Zhang, Microstructure and modeling of bainite transformation in deformed austenite. PhD thesis, Queen's University (2005).
- [58] W. Zhang, Y. Jin, A. Khachaturyan, Phase field microelasticity modeling of heterogeneous nucleation and growth in martensitic alloys, *Acta Materialia* 55 (2) (2007) 565–574.
- [59] Z. Nishiyama, *Martensitic transformation*, Elsevier, 2012.
- [60] W. Gong, Y. Tomota, Y. Adachi, A. Paradowska, J. Kelleher, S. Zhang, Effects of ausforming temperature on bainite transformation, microstructure and variant selection in nanobainite steel, *Acta Materialia* 61 (11) (2013) 4142–4154.
- [61] W. Johnson, P. Voorhees, Coherent phase diagrams, *Bulletin of Alloy Phase Diagrams* 9 (3) (1988) 208–215.
- [62] A. Artemev, Y. Jin, A. Khachaturyan, Three-dimensional phase field model and simulation of cubic \rightarrow tetragonal martensitic transformation in polycrystals, *Philosophical Magazine A* 82 (6) (2002) 1249–1270.

- [63] Zenan Yang, Wei Xu, Zhigang Yang, Chi Zhang, Sybrand van der Zwaag, A 2d analysis of the competition between the equiaxed ferritic and the bainitic morphology based on a gibbs energy balance approach, *Acta Mater.* 105 (2016) 317–327.
- [64] H. Bhadeshia, Bainite: Overall transformation kinetics, *Le Journal de Physique Colloques.* 43 (C4) (1982) C4–443 – C4–448.
- [65] F. Elhigazi, A. Artemev, The interaction between the displacive transformation and the diffusion process in the bainitic type transformation, *Computational Materials Science.* 169 (2019) 109079.
- [66] M. J. Santofimia, L. Zhao, J. Sietsma, Microstructural evolution of a low-carbon steel during application of quenching and partitioning heat treatments after partial austenitization, *Metallurgical and Materials Transactions A.* 40 (1) (2009) 46-57.
- [67] D. V. Edmonds, K. He, F.C. Rizzo, B. C. De Cooman, D. K. Matlock, J. G. Speer, Quenching and partitioning martensite—A novel steel heat treatment, *Materials Science and Engineering : A.* 438-440 (2006) 25-34.
- [68] Toji Yuki, Hiroshi Matsuda, Michael Herbig, Pyuck-Pa Choi, Dierk Raabe, Atomic-scale analysis of carbon partitioning between martensite and austenite by atom probe tomography and correlative transmission electron microscopy, *Acta Materialia.* 65 (2014) 215-228.
- [69] H.K.D.H. Bhadeshia, D.V. Edmonds, The bainite transformation in a silicon steel, *Metallurgical Transactions A.* 10 (7) (1979) 895-907.

- [70] C. Garcia-Mateo, J.A. Jimenez, H.W Yen, M.K. Miller, L. Morales-Rivas, M. Kuntz, S.P. Ringer, J.R. Yang, F.G. Caballero, Low temperature bainitic ferrite: Evidence of carbon super-saturation and tetragonality, *Acta Materialia*. 91 (2015) 162-173.
- [71] Kangying Zhu, Coralie Mager, Mingxin Huang, Effect of substitution of Si by Al on the microstructure and mechanical properties of bainitic transformation-induced plasticity steels, *Journal of Materials Science & Technology*. 33 (12) (2017) 1475-1486.
- [72] Yuki Toji, Goro Miyamoto, Dierk Raabe, Carbon partitioning during quenching and partitioning heat treatment accompanied by carbide precipitation, *Acta Mater*. 86 (2015) 137–147.
- [73] J. Zhonghua, P. Wang, D. Li, and Y. Li, Influence of the decomposition behavior of retained austenite during tempering on the mechanical properties of 2.25 Cr-1Mo-0.25 V steel, *Materials Science & Engineering A*. 742 (2019) 540-552.
- [74] R. Hadian, G.R. Purdy, On the nucleation of cementite on bainitic ferrite–austenite interphase boundaries, *Philosophical Magazine*. 94 (22) (2014) 2551-2561.
- [75] Yasuya Ohmori, Crystallographic aspects of bainite transformation in steels, *Scripta materialia*. 47 (3) (2002) 201-206.
- [76] D. Quidort, Y. Bréchet, The role of carbon on the kinetics of bainite transformation in steels, *Scripta Materialia*. 47 (3) (2002) 151-156.

- [77] Farideh Hajyakbary, Jilt Sietsma, Goro Miyamoto, Tadashi Furuwara, maria Jesus Santofimia, Interaction of carbon partitioning, carbide precipitation and bainite formation during the Q&P process in a low C steel, *Acta Mater.* 104 (2016) 72–83.
- [78] Guanghua Yan, Lizhan Han, Chuanwei Li, Xiaomeng Luo, Jianfeng Gu, Characteristic of retained austenite decomposition during tempering and its effect on impact toughness in SA508 Gr.3 steel, *Journal of Nuclear Materials.* 483 (2017) 167-175.
- [79] D. Quidort, Y.J.M. Brechet, Isothermal growth kinetics of bainite in 0.5% C steels, *Acta Materialia.* 49 (20) (2001) 4161-4170.
- [80] B.P.J. Sandvik, The bainite reaction in Fe-Si-C alloys: the secondary stage, *Metallurgical Transactions A.* 13 (5) (1982) 789-800.
- [81] Y. Ohmori, Y. -C. Jung, K. Nakai, H. Shioiri, Bainite transformation and the diffusional migration of bainite/austenite broad interfaces in Fe-9% Ni-C alloys, *Acta materialia.* 49 (16) (2001) 3149-3162.
- [82] Hong-Sheng Fang, Jia-Jun Wang, Yan-Kang Zheng, Formation mechanism of bainitic ferrite and carbide, *Metallurgical and Materials Transactions A.* 25 (9) (1994) 2001-2007.
- [83] H. -D. Wu, G. Miyamoto, Z. -G. Yang, C. Zhang, H. Chen, T. Furuwara, Incomplete bainite transformation in Fe-Si-C alloys, *Acta Materialia.* 133 (2017) 1-9.
- [84] Zener, Clarence, Kinetics of the decomposition of austenite, *Trans. Aime* 167 (1946) 550-595.

- [85] Martin Düsing, Rolf Mahnken, A coupled phase field/diffusion model for upper and lower bainitic transformation, *International Journal of Solids and Structures*. 135 (2018) 172-183.
- [86] Fazeli Fateh, Matthias Militzer, Modelling simultaneous formation of bainitic ferrite and carbide in TRIP steels, *ISIJ international*. 52 (4) (2012) 650-658.
- [87] R. Trivedi, The role of interfacial free energy and interface kinetics during the growth of precipitate plates and needles, *Metallurgical Transactions*. 1(4) (1970) 921.
- [88] S. Morito, H. Tanaka, R. Konishi, T. Furuhashi, T. Maki, The morphology and crystallography of lath martensite in Fe-C alloys, *Acta materialia*. 51 (6) (2003) 1789-1799.
- [89] Y.U. Wang, Y.M. Jin, A.G. Khachaturyan, Phase field microelasticity theory and modeling of elastically and structurally inhomogeneous solid, *J. Appl. Phys.* 92 (3) (2002) 1351–1360.
- [90] Xiao. Liu, Fan. Zhong, Jinxiu. Zhang, Mingxing. Zhang, Mokuang. Kang, Zhenqi. Guo, Lattice-parameter variation with carbon content of martensite. I. X-ray-diffraction experimental study, *Physical Review B*. 52 (14) (1995) 9970--9978.
- [91] Farideh HajyAkbari, Jilt Sietsma, Goro Miyamoto, Naoya Kamikawa, Roumen H. Petrov, Tadashi Furuhashi, Maria J. Santofimia, Analysis of the mechanical behavior of a 0.3C-1.6Si-3.5Mn(wt%) quenching and partitioning steel, *Materials Science and Engineering A*. 677 (2016) 505-514.

- [92] Thomas Klein, Christina Hofer, Marina Lukas, Tomasz Wojcik, Ronald Schnitzer, Matthew Galler, Gerald Ressel, Formation of "carbide-free zones" resulting from the interplay of C redistribution and carbide precipitation during bainitic transformation, *Materialia*. 7 (2019) 100380.
- [93] Rosalia Rementeria, Jose A. Jimenez, Sébastien Y. P. Allain, Guillaume Geandier, Jonathan D. Poplawsky, Wei Guo, Esteban Urones-Garrote, Carlos Garcia-Mateo, Francisca G. Caballero, Quantitative assessment of carbon allocation anomalies in low temperature bainite. *Acta Materialia*. 133 (2017) 333-345.
- [94] W. Song, J. von Appen, P. Choi, R. Dronskowski, D. Raabe, W. Bleck, Atomic-scale investigation of ϵ and θ precipitates in bainite in 100Cr6 bearing steel by atom probe tomography and ab initio calculations, *Acta Materialia*. 61(20) (2013) 7582-7590.
- [95] M. Takahashi, H. K. D. H. Bhadeshia, Model for transition from upper to lower bainite, *Materials Science and Technology*. 6 (7) (1990) 592-603.
- [96] G. Miyamoto, J. C. Oh, K. Hono, T. Furuhashi, T. Maki, Effect of partitioning of Mn and Si on the growth kinetics of cementite in tempered Fe-0.6 mass% C martensite, *Acta materialia*. 55(15) (2007) 5027-5038.
- [97] D. T. Pierce, D. R. Coughlin, D. L. Williamson, K. D. Clarke, A. J. Clarke, J. G. Speer, E. De Moor, Characterization of transition carbides in quench and partitioned steel microstructures by Mössbauer spectroscopy and complementary techniques, *Acta Materialia*. 90 (2015) 417-430.

- [98] A. Varshney, S. Sangal, Gouthama, A. K. Pramanick, K. Mondal, Microstructural evidence of nano-carbides in medium carbon high silicon multiphase steels, *Materials Science and Engineering A*. 708 (2017) 237-247.
- [99] D. T. Pierce, D. R. Coughlin, D. L. Williamson, J. Kähkönen, A.J. Clarke, K. D. Clarke, J. G. Speer, E. De Moor, Quantitative investigation into the influence of temperature on carbide and austenite evolution during partitioning of a quenched and partitioned steel, *Scripta Materialia*. 121 (2016) 5-9.
- [100] Y. X. Wu, W. W. Sun, M. J. Styles, A. Arlazarov, C. R. Hutchinson, Cementite coarsening during the tempering of Fe-C-Mn martensite, *Acta Materialia*. 159 (2018) 209-224.
- [101] Fang, Hong-Sheng, Jia-Jun Wang, and Yan-Kang Zheng. Formation mechanism of bainitic ferrite and carbide, *Metallurgical and Materials Transactions A*. 25 (1994) 2001-2007.
- [102] C. Philippot, K. Hoummada, M. Dumont, J. Drillet, V. Hebert, P. Maugis, Influence of a 2-D defect on the partitioning during the formation of a cementite particle in steels, *Computational Materials Science*. 106 (2015) 64-68.
- [103] J. Speer, D. K. Matlock, B. C. De Cooman, J. G. Schroth, Carbon partitioning into austenite after martensite transformation, *Acta materialia*. 51 (9) (2003) 2611-2622.
- [104] G. Kurdjumov, G. Sachs, Over the mechanisms of steel hardening, *Z. Phys* 64 (1930) 325–343.

- [105] N. Takayama, G. Miyamoto, T. Furuhashi, Effects of transformation temperature on variant pairing of bainitic ferrite in low carbon steel, *Acta Materialia* 60 (5) (2012) 2387–2396.
- [106] Z. Nishiyama, X-ray investigation of the mechanism of the transformation from face centered cubic lattice to body centered cubic, *Sci. Rep. Tohoku Univ.* 23 (1934) 637–664.